

UNIVERSITY OF CALIFORNIA

Los Angeles

Investigations of Stimulated Raman Scattering  
from High Density Underdense Plasmas  
Irradiated by a 0.35 Micron Laser

A dissertation submitted in partial satisfaction of the  
requirements for the degree Doctor of Philosophy  
in Physics

by

Humberto Glodulfo T. Figueroa Lopez

1986

UNIVERSITY OF CALIFORNIA

Los Angeles

Investigations of Stimulated Raman Scattering  
from High Density Underdense Plasmas  
Irradiated by a 0.35 Micron Laser

A dissertation submitted in partial satisfaction of the  
requirements for the degree Doctor of Philosophy  
in Physics

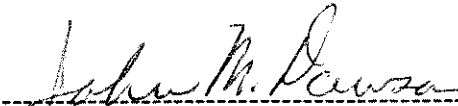
by

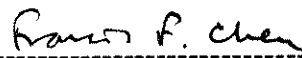
Humberto Glodulfo T. Figueroa Lopez

1986

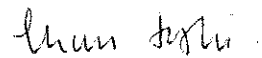
---

The dissertation of Humberto Glodulfo T. Figueroa Lopez is approved.

  
-----  
John M. Dawson

  
-----  
Francis F. Chen

  
-----  
A.T. Forrester, Committee Co-Chair

  
-----  
Chan Joshi, Committee Co-Chair

University of California, Los Angeles

1986

To my wife Dilia,

hoping that now I can help her to fulfill her dreams.

## TABLE OF CONTENTS

List of figures.....	vi
Acknowledgements.....	viii
Vita and publications.....	x
Abstract.....	xiii
Chapter I. INTRODUCTION.....	1
Chapter II. RAMAN THEORY.....	8
2.1. Equation for the scattered e.m. wave.....	11
2.2. Equation for the plasma wave.....	13
2.3. Dispersion relation for SRS-B.....	14
2.4. Growth rate for SRS-B.....	16
2.5. Thresholds for SRS-B.....	16
2.5.a. Collisional threshold.....	17
2.5.b. Convective threshold.....	18
2.6. Stimulated Raman forward scatter.....	24
Chapter III. PROPAGATION OF WAVES IN A RIPPLED PLASMA...	26
3.1. Theory.....	28
Chapter IV. EXPERIMENTS WITH FOIL TARGETS.....	46
4.1. Experimental conditions.....	46
4.2. Plasma diagnostics.....	48
4.3. Results and discussion.....	53
4.3.a. Scattered light measurements.....	53
4.3.b. Hot electron generation from foil targets.....	63
Chapter V. EXPERIMENTS WITH FOAM TARGETS.....	69

Chapter V. EXPERIMENTS WITH FOAM TARGETS.....	69
5.1. Experimental conditions.....	72
5.2. Results and discussion.....	74
Chapter VI. HALF HARMONIC SPLITTING.....	93
6.1. Splitting due to self generated magnetic fields.....	93
6.2. Splitting due to $2\omega_p$ decay.....	96
6.3. Splitting due to a density ripple from SBS.....	99
6.4 Experimental data.....	109
Chapter VII. SUMMARY.....	115
Appendix A. GLASS DEVELOPMENT LASER SYSTEM.....	119
References.....	121

## LIST OF FIGURES

Figure .....	page
2.1 SRS k-matching .....	10
2.2 Collisional threshold for SRS-B .....	19
2.3 Local k-matching for SRS-B .....	20
2.4 Convective threshold for SRS-B .....	23
3.1 Dispersion relations for the e.m. and the plasma waves .....	36
3.2 Wave dispersion relation in a rippled plasma with $\beta^2 = 1$ .....	37
3.3 Wave dispersion relation in a rippled plasma with $\beta^2 = 2$ .....	39
3.4 Wave dispersion relation in a rippled plasma with $\beta^2 = 10$ .....	40
3.5 Width of first forbidden band .....	41
3.6 Real and imaginary parts of dispersion relation .....	42
3.7 Imaginary part of wave number .....	43
3.8 Minimum value of $\alpha^2$ vs. $\beta^2$ .....	45
4.1 Experimental set-up for foil experiments .....	47
4.2 Experimental set-up for sidescatter detection .....	50
4.3 Spatial resolution of sidescatter .....	51
4.4 Temporal behavior of SRS-B .....	52
4.5 Time integrated SRS-B spectra .....	55
4.6 SRS-B polarization dependence .....	56
4.7 Enhanced Thomson scattering spectra .....	62

4.8	Electron emission from foil targets .....	65
5.1	SRS-B spectrum from an Al target .....	71
5.2	Experimental set-up for foam experiments .....	73
5.3	SRS-B spectrum from a $0.22n_c$ target .....	76
5.4	Temporal behavior of Raman gap .....	77
5.5	Raman reflectivity from foam targets .....	79
5.6	SRS reflectivity vs. target density .....	82
5.7	Forward Raman spectrum .....	83
5.8	SRS-F excitation from SRS-B .....	86
5.9	Dispersion relation of plasma wave .....	89
5.10	Behavior of a small wave vector mode $q_2$ .....	90
6.1	k- matching for $2\omega_p$ decay .....	98
6.2	Region for occurrence of SRS-B .....	101
6.3	Possible values of $h^2$ .....	102
6.4	$\omega$ - and k-matching for SRS-B .....	105
6.5	$\omega$ vs. k diagram of the plasma wave in a rippled plasma .....	107
6.6	$\omega_o/2$ splitting .....	110
6.7	Predicted $\omega_o/2$ splitting from SRS-B in a rippled plasma .....	114
A.1	Layout of GDL system .....	120



## ACKNOWLEDGEMENTS

The author is deeply indebted to a great many people who contributed to the execution of this work.

I wish to thank the LLE personnel, Dr. T. Bristow, Dr. W. Seka, Dr. K. Tanaka, Dr. J. Soures, Professor L. Goldman, Professor A. Simon, Professor R. McCrory, Mr. J. Boles, Mr. B. Flaherty, Mr. R. Boni, and Mr. R. Bahr for their hospitality and collaboration during my frequent visits to the National Laser Users Facility at the University of Rochester where the experimental work described in this dissertation was carried out. Also, I want to thank Professor A. Simon for letting me include his data in this work.

I am very grateful to my family in Venezuela, Conicit, Fundacion Gran Mariscal de Ayacucho, Compania Anonima La Electricidad de Caracas, and Professor Chan Joshi for financial support

My thanks to Miss Maria Gonzales for keeping all the parts of the administrative machinery running smoothly, and for deciphering the Pyramid manual.

I also wish to thank Dr. K. Estabrook for providing the fluid simulations of the foil and foam targets.

Special thanks to Drs. Hiroshi Azechi and N. Ebrahim who took the electron data and played an active role in the analysis of the foil results.

I am also very thankful to Dr. Chris Clayton, who was always ready to lend a hand in the every day work. I also thank him and Mr. Ken Marsh for useful discussions and for taking active part in the data collection of the foil and foam targets.

The author wants to acknowledge useful discussions with Don Umstadter, Dr. Chris Clayton, Warren Mori, Dr. Tom Katsouleas, and Professor J. Dawson on the propagation of waves in a rippled plasma.

I want to thank Professor T. Forrester for being my sponsor in the Physics Department.

I am very grateful to Professor Francis Chen for innumerable discussions throughout the development of this dissertation, but especially for insisting on pointing at the "road to Nirvana" every Friday afternoon.

The author is also deeply indebted to Professor Chan Joshi, whose personal dedication, perseverance, and day-to-day guidance made possible the existence of the present work and the birth of a new physicist.

Above all, I wish there were words to express indebtedness to my wife Dilia, who year after year gave all she had and more for the completion of this work. To her, my eternal gratitude.

This work was supported by the DOE Inertial Confinement Fusion program.

## VITA

- June 10, 1952    Born, Venezuela.
- 1977            Licentiate in Physics, Universidad Central de Venezuela.
- 1980            M.S.,    University    of    California,    Los    Angeles.  
Teaching Assistant, Department of Physics, University of California, Los Angeles.
- 1982-1986      Post-graduate Research Engineer, Department of Electrical Engineering, University of California, Los Angeles.
- 1985            Teaching Fellow, Department of Physics, University of California, Los Angeles.  
Referee for the journal *The Physics of Fluids*.

## PUBLICATIONS AND PRESENTATIONS

- H. Azechi, N.A. Ebrahim, H. Figueroa and C. Joshi, "Hot Electron Generation in UV-Laser-Irradiated Underdense Plasmas," in *Plasma Physics and Controlled Nuclear Fusion Research*, Vol. 1, p.115 (1982).
- H. Azechi, N.A. Ebrahim, K. Estabrook, C.E. Clayton, H. Figueroa, and C. Joshi, "Studies of High Frequency Instabilities in 0.35 Micron Laser-Produced Hot Long Scalelength Underdense Plasmas," American Physical Society--Division of Plasma Physics Meeting, New Orleans (1982).
- H. Azechi, N.A. Ebrahim, K. Estabrook, C. Clayton, H. Figueroa, and C. Joshi, "Two Plasmon Decay and Stimulated Raman Scattering Instabilities in 0.35 Micron Laser Produced Underdense Plasmas," American Physical Society--

- Division of Plasma Physics Meeting, New Orleans (1982).
- H. Figueroa, C. Joshi, N.A. Ebrahim and H. Azechi, "Studies of Raman Back and Forward Scattering at 0.35 Microns," IEEE International Conference on Plasma Science, San Diego (1983).
- H. Azechi, N.A. Ebrahim, H. Figueroa, and C. Joshi, "Raman Back and Forward Scattering Studies at 0.35 Microns," American Physical Society--Division of Plasma Physics Meeting, Los Angeles (1983).
- H. Figueroa, C. Joshi, C.E. Clayton, H. Azechi, N.A. Ebrahim, and K. Estabrook, "High Frequency instabilities in Underdense Plasmas produced by a 0.35 Micron Laser," in *Laser Interaction and Related Plasma Phenomena*, edited by H. Hora and G. Miley, p.527, Plenum Press, New York (1984).
- H. Figueroa, C. Joshi, H. Azechi, N.A. Ebrahim, and K. Estabrook, "Stimulated Raman Scattering, Two Plasmon Decay and Hot Electron Generation from Underdense Plasmas at 0.35 Microns," *The Physics of Fluids* 27, 1887 (1984).
- C. Joshi, H. Figueroa, and C.E. Clayton, "Observations of Forward Scattering and Filamentation at 0.35 Microns," American Physical Society--Division of Plasma Physics Meeting, Boston (1984).
- H. Figueroa, C. Joshi, and C.E. Clayton, "Studies of Stimulated Raman Backscattering from Long, Underdense Plasmas at 0.35 Microns," American Physical Society--Division of Plasma Physics Meeting, Boston (1984).
- H. Figueroa and C. Joshi, "Propagation of Electron Plasma Waves in a Rippled

Density Profile and its Effects on Stimulated Raman Scattering," American Physical Society--Division of Plasma Physics Meeting, San Diego (1985).

R.B. Palmer, N. Bagget, J. Claus, R. Fernow, I. Stumer, H. Figueroa, N. Kroll, W. Funk, G. Lee-Whiting, M. Pickop, P. Goldstone, K. Lee, P. Corkum, and T. Himel, "Report of Near Field Group," in *Proc. 2nd. Workshop on Laser Acceleration of Particles*, p. 234, American Institute of Physics, New York (1985).

H. Figueroa and C. Joshi, "Half Harmonic Splitting from Raman Scatter in a Rippled Plasma," Anomalous Absorption Conference, New York (1986).

H. Figueroa and C. Joshi, "Experimental Studies on Raman Scattering from Foam Targets at 0.35 Microns," accepted for Publication in *The Physics of Fluids*, July (1986).

H. Figueroa and C. Joshi, "Wave Propagation in a Rippled Plasma," to be published in *Laser Interaction and Related Plasma Phenomena*, edited by H. Hora and G. Miley, Plenum Press, New York (1986).

H. Figueroa and C. Joshi, "Half Harmonic Splitting Due to Raman Scatter in a Rippled Plasma," submitted for publication to *The Physics of Fluids*.

ABSTRACT OF THE DISSERTATION

Investigations of Stimulated Raman scattering  
from High Density Underdense Plasmas  
Irradiated by a 0.35 Micron Laser

by

Humberto Glodulfo T. Figueroa Lopez

Doctor of Philosophy in Physics

University of California, Los Angeles, 1986

Professor A.T. Forrester, Co-Chair

Professor Chan Joshi, Co-Chair

Studies of stimulated Raman back and forward scattering and the generation of high energy electrons at 0.35 microns are presented. To isolate the various phenomena occurring at different densities, we attempted to control the plasma density by varying the thickness of the foil targets and also by using foam targets of variable average density. The frequency of the scattered light is used as a diagnostic to measure the plasma density. Time resolved and time integrated spectra for various plasma densities are discussed. Also, the measured energy and angular distribution of the high energy electrons from foil targets are presented. Two-plasmon decay is suggested as the probable mechanism generating the hot electrons.

The backscattered light presents a broadband spectrum in the sub-half-harmonic region. This spectrum is limited by a sharp cut-off near 400 nm and by a spectral gap near the half-harmonic region. The half-harmonic spectrum is shown to be split into a red and a blue shifted peak. Effects of the self-generated magnetic fields and plasma temperature on Raman scattering and two-plasmon decay, respectively, are examined as possible mechanisms responsible for the splitting of the half-harmonic spectrum. Finally, a discussion of the effects of the coupling of Raman and Brillouin scattering on the Raman spectrum is presented with emphasis on the quarter critical region. This last mechanism is suggested to contribute to the splitting of the half-harmonic light.

## CHAPTER I

### INTRODUCTION

High frequency parametric instabilities excited when an intense electromagnetic pulse  $(\omega_0, \mathbf{k}_0)$  propagates through an underdense plasma are currently under active investigation<sup>1-59</sup>. Energy and momentum conservation give

$$\omega_0 = \omega_1 + \omega_2, \quad \mathbf{k}_0 = \mathbf{k}_1 + \mathbf{k}_2 \quad (1.1)$$

where at least one of the decay waves is an electron plasma wave (epw) with the dispersion relation

$$\omega_{\text{epw}}^2 = \omega_p^2 + 3k_p^2 v_e^2 ; \quad (1.2)$$

$\omega_p = (4\pi n_e^2/m_e)^{1/2}$  is the plasma frequency,  $v_e = (kT_e/m_e)^{1/2}$  is the electron thermal velocity, and  $\mathbf{k}_p$  is the electron plasma wave wave vector. In the underdense corona of a laser fusion pellet there are two such instabilities of great significance: the stimulated Raman scattering (SRS) instability and the two-plasmon decay ( $2\omega_p$ ) instability. This is because the plasma waves associated with these instabilities can have phase velocities on the order of the speed of light and therefore produce very energetic electrons when they damp<sup>60-70</sup>. Since such electrons can preheat the fuel in a laser fusion pellet before significant compression, the  $2\omega_p$  and the SRS instabilities are of particular concern. In the



$2\omega_p$  decay instability, the two decay waves are both plasma waves, so that the frequency matching can occur only if  $\omega_o \approx 2\omega_p$ . This instability can therefore be expected to occur only near the quarter-critical ( $n_c/4$ ) layer of an inhomogeneous plasma. The SRS instability, on the other hand, results from the resonant decay of an incident photon into a scattered photon plus a plasmon. Since the minimum frequency of an electromagnetic (e.m) wave in a plasma is  $\omega_p$ , this process can occur in the plasma region with densities  $n \leq n_c/4$ . If the scattering of the laser light from SRS is strong enough, the laser light could be prevented from reaching the critical density where the laser absorption is the strongest. On the other hand, the energy of the laser beam could be anomalously absorbed by the underdense plasma through the excitation of the plasma waves by SRS. The relative importance of the reflective and absorptive nature of the SRS instability, is dictated by the conservation law for wave action, or Manley-Rowe relation<sup>71</sup> which gives

$$\frac{W_o}{\omega_o} = \frac{W_1}{\omega_1} = \frac{W_2}{\omega_2} \quad (1.3)$$

where  $W_j = N_j \hbar \omega_j$  and  $N_j$  is the change in the number of quanta in the  $j$ th wave. Thus, except at  $n_c/4$ , the energy given to the scattered e.m. wave is always greater than that for the plasma wave.

Experimental observations of the SRS instability have been reported by several authors. Bobin et al.<sup>2</sup> observed a scattered spectrum at  $\omega_o/2$  and a width twice that of the laser when a  $1 \times 10^9$  W Nd-glass laser was focused on a solid hydrogen target. Later, Watt et al.<sup>10</sup> studied the threshold and growth rate of

SRS. In their experiments, a  $3 \times 10^9 \text{ W/cm}^2$   $\text{CO}_2$  laser was focused on a 20 cm long hydrogen plasma which was created and confined by a 16.5 kG  $\theta$ -pinch. Once the laser exceeded an intensity of  $3 \times 10^8 \text{ W/cm}^2$ , an exponential growth was observed in the backscattered light. This scattered radiation showed a shift in frequency which was in agreement with the expected frequency shift due to scattering from the excited plasma waves at the measured density of  $2 \times 10^{16} \text{ cm}^{-3}$ . Raman scatter from a  $\theta$  pinch has also been observed by Amini<sup>10</sup>.

Phillion et al.<sup>19</sup> reported the first SRS measurements from solid targets when a high intensity 1.064  $\mu\text{m}$  laser (Shiva) and a 0.532  $\mu\text{m}$  laser (Argus) were focused on solid disc targets of both low- and high- Z materials. The scattered spectrum, spectrally and temporally resolved, showed a broadband of frequencies with a maximum intensity below  $\omega_0/2$ . The half harmonic spectrum showed a blue and a red shifted peak. The scattered spectrum was observed at laser intensities as low as  $5 \times 10^{14} \text{ W/cm}^2$ . These experiments were among the first using a solid target where SRS apparently occurred "below threshold".

Spectrally and temporally resolved measurements of SRS reported by Turner and co-workers<sup>25</sup>, showed that when flat solid targets were irradiated with a high power, nanosecond, 0.523  $\mu\text{m}$  laser beam, the observed scattered light came principally from densities below  $n_c/4$ . The scattered light occurred nearly simultaneously over a wide range of frequencies and it was seen to occur in bursts of duration  $< 50$  psec.

The first measurements of the SRS spectrum with a 0.35  $\mu\text{m}$  laser as a pump, were made by Tanaka et al.<sup>22</sup> Tanaka made time integrated measurements of the backscattered light when a parylene slab target was irradiated with a 0.35  $\mu\text{m}$  laser with intensities between  $10^{13} \text{ W/cm}^2$  and  $10^{15} \text{ W/cm}^2$ . A broad

continuum spectrum was observed, similar to the one reported by Phillion et al.<sup>19</sup> A distinct gap in the spectrum between the  $\omega_0/2$  and the broadband spectrum was conjectured to be due to profile steepening. The half-harmonic radiation intensity showed two distinct increases at the threshold intensities of  $4 \times 10^{13}$  and  $4 \times 10^{14}$  W/cm<sup>2</sup>. The first increase was attributed to the excitation of the  $2\omega_p$  decay instability and the second, to the excitation of SRS at the  $n_c/4$  layer.

The most direct way to observe the Raman instability in experiments is to measure the frequency shift of the scattered light from the frequency  $\omega_0$  of the incident laser. This shift should agree with the frequency of the electron plasma waves for plasmas with densities below  $n_c/4$ . It is important to recognize, however, that the scattered light with frequency  $\omega_0/2$  could ambiguously come from the mode conversion of the plasma waves from the  $2\omega_p$  instability into e.m. waves. This mode conversion, which is a process inverse of resonance absorption, is possible since the plasma waves are being excited very close to their cut-off density.

The first measurements of parametrically excited plasma waves at  $n_c/4$  were made by Schuss et al.<sup>11</sup> In their experiments, a 40J, 130 nsec FWHM CO<sub>2</sub> laser was focused into a hydrogen gas jet. The plasma waves thus excited, were detected through Thomson scattering of a ruby laser from these waves. The scattered ruby light showed a sharp increase in intensities at a frequency shift of  $\Delta\omega = \omega_0/2$ , indicating that the scattering process was due to the presence of plasma waves at  $n_c/4$ . These measurements agreed with interferometric measurements of the plasma density.

Ruby Thomson scattered measurements also allowed Baldis et al.<sup>12</sup> to observe the decay plasma waves generated by  $2\omega_p$  decay when a  $5 \times 10^{12}$  W/cm<sup>2</sup>,

4 nsec FWHM CO<sub>2</sub> laser pulse was focused on a solid carbon disc. Optical interferometry, performed simultaneously with Thomson scattering, showed steepening of the profile at densities  $n_c/4$  and below. Time resolved Thomson scattered measurements<sup>16-17</sup> showed the saturation of the  $2\omega_p$  decay instability which was attributed to the ion motion driven by the ponderomotive force associated with the large amplitude electrostatic waves.

Thomson scattering has been used to probe for Raman driven plasma waves by several groups. Darrow et al.<sup>90</sup> used the frequency shifted signal, by the plasma frequency  $\omega_p$ , of the Thomson scattered light as a sensitive diagnostic of plasma density in an optical mixing experiment. Walsh et al.<sup>32</sup> used Thomson scattering to simultaneously time resolve the Raman driven plasma wave and the Brillouin driven ion wave. Recently, Mayer and co-workers<sup>109</sup> have investigated the evolution of plasma waves from a plasma with a density gradient, by  $k$  and time resolving the Thomson scattered light. Finally, D. Umstadter<sup>114</sup> at UCLA has recently simultaneously measured the frequency shift of the backscattered light and the frequency of the plasma wave (by Thomson scattering) and conclusively demonstrated that the backscatter instability was Raman by the  $\omega$ - and  $k$ -matching condition.

High energy electrons generated by the SRS and  $2\omega_p$  decay instabilities have been observed directly by Ebrahim et al.<sup>60-62</sup>, Joshi et al.<sup>63</sup>, Burger et al.<sup>68</sup>, and Villeneuve et al.<sup>69</sup>; and indirectly via the high energy x-ray bremsstrahlung they produce by Phillion et al.<sup>66</sup>, by Nugent et al.<sup>67</sup>, and by Keck et al.<sup>70</sup>. Ebrahim and Joshi<sup>61</sup> made detailed measurements of heated electron distributions created by the interaction of a  $10^{12}$  -  $10^{14}$  W/cm<sup>2</sup> CO<sub>2</sub> laser with plasmas created from solid targets. The angular measurements of the energetic

electrons indicated that the electrons were ejected preferentially in the backward direction with maximum energies of up to 600 KeV. Since the plasmas created from the solid targets were highly inhomogeneous with peak plasma densities larger than the critical density, the authors were unable to discriminate the process responsible for the accelerated electrons.

Villeneuve et al.<sup>69</sup> measured the hot electron emission from a uv laser produced plasma from a solid target. The majority of the hot electrons with energies between 100 - 400 keV were thought to be produced by the  $2\omega_p$  decay since the hot electron threshold correlated very well with the onset of the  $\omega_0/2$  radiation.

In the experimental part of this dissertation, we present direct observations of the SRS instability induced by a 0.35  $\mu\text{m}$  laser in totally underdense plasmas. At this short wavelength, collisional or inverse bremsstrahlung absorption is the dominant coupling mechanism. Also, the inhomogeneous threshold for SRS is much higher for a given scalelength at shorter wavelengths. However, the next generation of laser-fusion targets will produce plasmas that are thousands of wavelengths long. In such plasmas, the extent to which this instability will play a role will be dependent upon the complex interplay between lowering of the threshold with increasing scalelength and whole-beam or small-scale self-focusing because of thermal or ponderomotive effects, on the one hand, and stabilization by significant collisional absorption below  $n_c/4$  on the other. To isolate the phenomena occurring at and below  $n_c/4$ , we attempted to control the maximum density of the plasma by two different methods. In the first method, we used a 1  $\mu\text{m}$  prepulse on a limited thickness target. An intense 0.35  $\mu\text{m}$  mainpulse is then used to excite the instabilities in such a preformed plasma. In

the second method, foam disc targets of various densities were irradiated by the 0.35  $\mu\text{m}$  main pulse. These targets allowed us to vary the average plasma density in the neighborhood of  $n_c/4$  and at the same time permitted us to create plasmas, with only a laser of modest energy of about 50 J, whose lengths approached that of plasmas expected to be generated from a future laser fusion pellet.

This dissertation is structured as follows. Chapter II contains a review of the SRS theory that is directly applicable to our experiments. The theory of plasma waves and electromagnetic waves propagating in a rippled plasma is presented in Chapter III. The experimental results from foils and foam targets, together with a detailed discussion of the results, are presented in Chapters IV and V. Chapter VI discusses the splitting of the half-harmonic light, and Chapter VII contains the summary and conclusions. The appendix contains a short review of the laser system used in these experiments.

## CHAPTER II

### RAMAN THEORY

The theory of Raman scattering in homogeneous and inhomogeneous plasmas has been worked out by several authors. For completeness, we give a simplified review of this theory following very closely the works of Drake et al.<sup>4</sup> and Estabrook and Kruer<sup>24</sup>.

Stimulated Raman scattering is the process by which an incident e.m. wave of high enough intensity decays into a plasma wave and a scattered e.m. wave of different frequency. This process satisfies the frequency and wave vector matching conditions:

$$\omega_o = \omega_s + \omega_{epw} \quad (2.1)$$

and

$$\mathbf{k}_o = \mathbf{k}_s + \mathbf{k}_p \quad (2.2)$$

Here,  $(\omega_o, \mathbf{k}_o)$  is the frequency and wave vector of the incident e.m. wave;  $(\omega_s, \mathbf{k}_s)$  and  $(\omega_{epw}, \mathbf{k}_p)$  are the frequency and wave vector of the e.m. scattered wave and plasma wave respectively.

From these two equations one can easily see that SRS will occur in the region of densities  $n \leq n_c/4$ . Thus, the scattered frequency will fall in the range  $\omega_o/2 \leq \omega_s \leq \omega_o$ .  $\omega_s = \omega_o/2$  corresponds to scattering from  $n_c/4$ , whereas  $\omega_s = \omega_o$  corresponds to the limiting case of scattering from zero density. This two bounds

for the scattered frequency are correct in the cold plasma approximation; however, corrections due to the finite plasma temperature will modify these two limits.

In what follows, we will consider a 1-D plasma; thus, we will be concerned only with two types of Raman scattering: (1) stimulated Raman backscattering (SRS-B) and (2) stimulated Raman forward scattering (SRS-F). The labels back and forward correspond to the direction of the scattered wave. In back scatter, the direction of the scattered wave opposes that of the incident e.m. wave. In forward scatter, the scattered wave travels in the same direction of the incident wave. The k-matching diagram for these two processes are shown in Figs. 2.1(a) and 2.1(b).

Let us consider a plane polarized e.m. wave  $\mathbf{E}(\mathbf{x},t)$  propagating in an infinite, homogeneous plasma

$$\begin{aligned}\mathbf{E}(\mathbf{x},t) &= E_0 \mathbf{e}_0 \cos(\mathbf{k}_0 \cdot \mathbf{x} - \omega_0 t) \\ &= \frac{1}{2} E_0 \mathbf{e}_0 e^{i(\mathbf{k}_0 \cdot \mathbf{x} - \omega_0 t)} + \text{c.c}\end{aligned}\tag{2.3}$$

The equilibrium will consist of electrons oscillating in the electric field of the incident e.m. wave. The ions are assumed to be fixed. Let us now perturb the electron density with a small disturbance

$$n_1(\mathbf{x},t) = n_1 e^{i(\mathbf{k} \cdot \mathbf{x} - \omega_{\text{epw}} t)} + \text{c.c}\tag{2.4}$$

This perturbation will scatter radiation with frequency and wave vector

$$\omega_s \equiv \omega_{\pm} = \omega_{\text{epw}} \pm \omega_0\tag{2.5a}$$



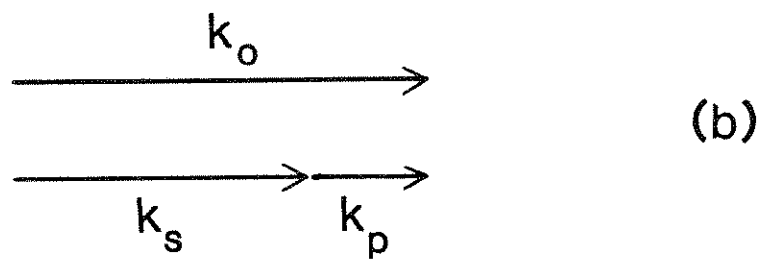
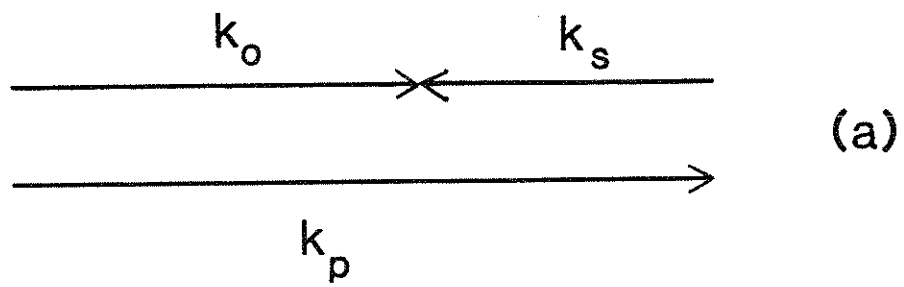


FIG. 2.1.  $k$  matching for (a) SRS-B, and (b) SRS-F, assuming all frequencies positive.

and

$$\mathbf{k}_s \equiv \mathbf{k}_\pm = \mathbf{k}_p \pm \mathbf{k}_o \quad (2.5b)$$

The scattered sidebands will beat with the incident e.m. wave at the frequency and wave vector  $(\omega_p, \mathbf{k}_p)$ . This beat wave will enhance the density perturbation through the ponderomotive force, which in turn, will scatter more radiation. Thus, we have a feedback loop whose final result is the excitation of the daughter waves  $(\omega_s, \mathbf{k}_s)$  and  $(\omega_{epw}, \mathbf{k}_p)$  at the expense of the energy contained in the pump  $(\omega_o, \mathbf{k}_o)$ . Notice that Fig. 2.1 does not correspond to Eq. (2.5b) since now  $\omega_s$  can be negative.

## 2.1 EQUATION FOR THE SCATTERED E.M. WAVE.

Let us assume that the scattered e.m. wave are plane waves of the form

$$\mathbf{E}_\pm(\mathbf{x}, t) = \mathbf{E}_\pm \mathbf{e}_\pm e^{i(\mathbf{k}_\pm \cdot \mathbf{x} - \omega_\pm t)} + \text{c.c} \quad (2.6)$$

From Maxwell's eqns. one gets the vector wave eqn. for  $\mathbf{E}_\pm(\mathbf{x}, t)$ :

$$\nabla(\nabla \cdot \mathbf{E}_\pm) - \nabla^2 \mathbf{E}_\pm + \frac{1}{c^2} \frac{\partial^2 \mathbf{E}_\pm}{\partial t^2} = \frac{4\pi}{c^2} \frac{\partial \mathbf{J}_\pm}{\partial t} \quad (2.7)$$

Since we are looking for scattering at the frequencies  $\omega_\pm$ , we have to consider the components of the current density  $\mathbf{J}$  that oscillate at those frequencies. Thus, the only possible combinations of density and velocity in  $\mathbf{J}$  will be

$$\mathbf{J}_+ = -en_0\mathbf{v}_+ - en_1\mathbf{v}_o \quad (2.8a)$$

and

$$\mathbf{J}_- = -en_0\mathbf{v}_- - en_1\mathbf{v}_o^* \quad (2.8b)$$

Here,  $\mathbf{v}_\pm$  and  $\mathbf{v}_o$  are the quiver velocities of the electrons in the fields of the scattered waves and the incident wave respectively:

$$\mathbf{v}_\pm = \frac{-ie}{m\omega_\pm} \mathbf{E}_\pm \quad (2.9a)$$

$$\mathbf{v}_o = \frac{-ie}{m\omega_o} \mathbf{E}_o \quad (2.9b)$$

$\mathbf{v}_o^*$  is the complex conjugate of  $\mathbf{v}_o$ . The relations (2.9) are valid only if the electron velocity is much less than  $c$ . This is true for most of today's lasers.

Substituting eqns. (2.9), (2.8), and (2.6) into eqn. (2.7) one gets, in the 1-D case:

$$(\omega_+^2 - \omega_p^2 - c^2k_+^2)\mathbf{v}_+ = \omega_p^2 \frac{n_1}{n_0} \mathbf{v}_o \quad (2.10a)$$

and

$$(\omega_-^2 - \omega_p^2 - c^2k_-^2)\mathbf{v}_- = \omega_p^2 \frac{n_1}{n_0} \mathbf{v}_o^* \quad (2.10b)$$

These equations give the scattered electric field produced by the interaction of the pump with the density perturbation.

## 2.2 EQUATION FOR THE PLASMA WAVE

The plasma wave will be excited by the ponderomotive force that results from the beating of the sideband modes with the incident e.m. wave.

The equations needed to get an expression for the behavior of the density fluctuations in terms of the coupling between  $\mathbf{E}_0$  and  $\mathbf{E}_\pm$  are the following:

a) Poisson's eqn.:

$$\nabla \cdot \mathbf{E} = -4\pi en_1 \quad (2.11)$$

b) Continuity eqn.:

$$\frac{\partial n}{\partial t} + \nabla \cdot (n\mathbf{v}) = 0 \quad (2.12)$$

c) Equation of motion:

$$\frac{\partial \mathbf{v}}{\partial t} = -\frac{e}{m} \mathbf{E} - 3v_e^2 \frac{\nabla n_1}{n_0} - \frac{1}{2} \nabla (\mathbf{v} \cdot \mathbf{v}) \quad (2.13)$$

The first term on the RHS of the eqn. of motion is the acceleration due to the longitudinal electric field, the second term is the acceleration due to pressure, and the last term is the ponderomotive acceleration. This last term will contain the beating between  $\mathbf{E}_0$  and  $\mathbf{E}_\pm$ .

Since we are looking for perturbations with phase  $\mathbf{k}_p \cdot \mathbf{x} - \omega_{epw} t$ , we need to take the components of the eqns. (2.11), (2.12), and (2.13) with that phase. Fourier analyzing in space and time, we get

$$ik_p E = -4\pi en_1 \quad (2.14)$$

$$-\omega_{epw} n_1 + n_o k_p v = 0 \quad (2.15)$$

$$-i\omega_{epw} v = -\frac{e}{m} E - 3iv_e^2 \frac{n_1}{n_o} k_p - ik_p (v_- v_o + v_+ v_o^*) \quad (2.16)$$

Solving for  $n_1$  one gets:

$$\frac{n_1}{n_o} = k_p^2 \frac{v_- v_o + v_+ v_o^*}{\omega_{epw}^2 - \omega_p^2 - 3k_p^2 v_e^2} \quad (2.17)$$

Now, multiply eqn. (2.16a) by  $v_o^*$  and eqn. (2.16b) by  $v_o$  and substitute into eqn. (2.17). We get

$$\omega_{epw}^2 - \omega_p^2 - 3k_p^2 v_e^2 = -k_p^2 \omega_p^2 \frac{|v_o|^2}{4} \left[ \frac{1}{D_+} + \frac{1}{D_-} \right] \quad (2.18)$$

where

$$D_+ = c^2 k_+^2 - \omega_+^2 + \omega_p^2 \quad (2.19a)$$

and

$$D_- = c^2 k_-^2 - \omega_-^2 + \omega_p^2 \quad (2.19b)$$

### 2.3 DISPERSION RELATION FOR SRS-B

From eqns. (2.19) and (2.5), one can obtain the relation between  $D_+$  and  $D_-$ :

$$D_+ = 4\omega_o \left[ \frac{c^2 \mathbf{k}_p \cdot \mathbf{k}_o}{\omega_o} - \omega_{epw} \right] + D_- \quad (2.20)$$

If  $D_+ \approx D_- \approx 0$  both side bands will be resonantly excited, otherwise only the  $(\omega_-, \mathbf{k}_-)$  will be unstable and the  $D_+$  term can be neglected in eqn. (2.18). This latter case will be true only if

$$\frac{c^2 \mathbf{k}_p \cdot \mathbf{k}_o}{\omega_o} > \omega_{epw} \quad (2.21)$$

In the case of SRS-B, the range of values for the wave number of the plasma wave will fall in the interval  $k_o \leq k_p \leq 2k_o$ , with  $k_p$  on the order of  $k_o$  only at  $\frac{n_c}{4}$ . Thus,

$$\omega_o < \frac{c^2 k_p k_o}{\omega_o} < 2\omega_o$$

and both  $D_+$  and  $D_-$  cannot be simultaneously excited. Therefore, in the case of excitation of the SRS-B instability, the  $D_+$  term can be neglected in the dispersion relation, eqn. (2.18), resulting:

$$(\omega_{epw}^2 - \omega_p^2 - 3k_p^2 v_e^2)(\omega_-^2 - \omega_p^2 - c^2 k_-^2) = -\frac{k_p^2 \omega_p^2 |v_o|^2}{4} \quad (2.22)$$

Notice that on the left hand side we have the dispersion relations of the plasma wave and the scattered e.m. wave which are now coupled through the pump  $v_o$ . For  $v_o = 0$ , we regain the uncoupled modes.

## 2.4 GROWTH RATE FOR SRS-B

One can estimate the growth rate for SRS-B by letting  $\omega_{\text{epw}} \rightarrow \omega_{\text{epw}} + i\delta$  and substituting in eqn. (2.22). Neglecting the temperature term, one obtains:

$$\delta = \frac{k_p v_o}{4} \left[ \frac{\omega_p}{\omega_o - \omega_p} \right]^{1/2} \quad (2.23)$$

The value of  $k_p$  can be obtained from the  $\omega$ - and  $k$ -matching conditions eqns. (2.1) and (2.2) to give:

$$k = \frac{\omega_o}{c} \left[ 1 - \frac{n}{n_c} \right]^{1/2} + \left[ 1 - 2 \left[ \frac{n}{n_c} \right]^{1/2} \right]^{1/2} \quad (2.24)$$

## 2.5 THRESHOLDS FOR SRS-B

So far, we have neglected all the energy dissipation terms in our calculations. This means that SRS-B could be excited by any e.m. wave of arbitrary intensity. However, if the daughter waves dissipate energy into the bulk of the plasma, the instability will grow only if the intensity of the pump is higher than a given threshold. This threshold can be estimated by introducing a phenomenological dissipation process into the eqn. (2.22). Let  $\gamma_p$  and  $\gamma_-$  represent the energy dissipation terms associated with the plasma wave and the scattered e.m. wave respectively. Thus, assuming weak damping, eqn.(2.22) can be written as

$$(\omega_{epw}^2 + i\gamma_p\omega_{epw} - \omega_p^2)(\omega_-^2 + i\gamma_-\omega_- - c^2k_-^2 - \omega_p^2) = -\frac{k_p^2\omega_p^2|v_o|^2}{4} \quad (2.25)$$

Here, the temperature term has been neglected. Letting  $\omega_{epw} \rightarrow \omega_p + i\delta$  we get at threshold ( $\delta=0$ ):

$$|v_o|^2 = 16\frac{\gamma_p\gamma_-}{k_p^2}\frac{\omega_-}{\omega_p} \quad (2.26)$$

The physical meaning of this relation can be made clear if we write it in terms of the growth rate. Substituting eqn.(2.23) into eqn.(2.26) we get

$$\delta^2 = \gamma_p\gamma_- \quad (2.27)$$

This says that the threshold will occur when the rate at which the energy is being deposited into the daughter waves equals the rate at which the daughter waves dissipate energy.

### 2.5.a COLLISIONAL THRESHOLD

If the dominant mechanism that dissipates energy into the plasma is electron-ion collisions, then the  $\gamma_p$  and  $\gamma_-$  terms are given by

$$\gamma_p = \frac{V_{ei}}{2} \quad (2.28a)$$

and



$$\gamma_- = \frac{\omega_p^2}{\omega_-^2} \frac{\nu_{ei}}{2} \quad (2.28b)$$

Here,  $\nu_{ei}$  is the electron-ion collision frequency. Substituting the eqns. (2.28) into eqn. (2.26) one gets the threshold due to collisions. Fig. 2.2 shows the values of collisional threshold vs. the plasma density. We have used the typical parameters that apply to our experiments:  $T_e = 1\text{keV}$  and  $\lambda_0 = 0.35\mu\text{m}$ . The maximum threshold is on the order of  $10^{13} \text{ W/cm}^2$  and occurs at  $n_c/4$ . This threshold is 2 orders of magnitude lower than the average laser intensity used in our experiments. Therefore, collisions would not prevent us from exciting the SRS-B instability. However, collisions is not the only mechanism that can dissipate energy. Plasmas created from solid targets are highly inhomogeneous, and convection of the daughter waves can effectively dissipate energy out of the interaction region. This introduces a new type of threshold that the pump has to overcome in order to excite the SRS instability.

### 2.5.b CONVECTIVE THRESHOLD

Let us assume a plasma created from a solid target with a density profile as shown in Fig. 2.3. The daughter waves resonantly excited at  $x_0$  will move away from the resonant region and will be absorbed by the plasma in regions where the phase mismatch exceeds  $1/2^{24}$ .

The threshold due to this convective process can be estimated by substituting the dissipative terms  $\gamma_p$  and  $\gamma_-$  in eqn. (2.26) for

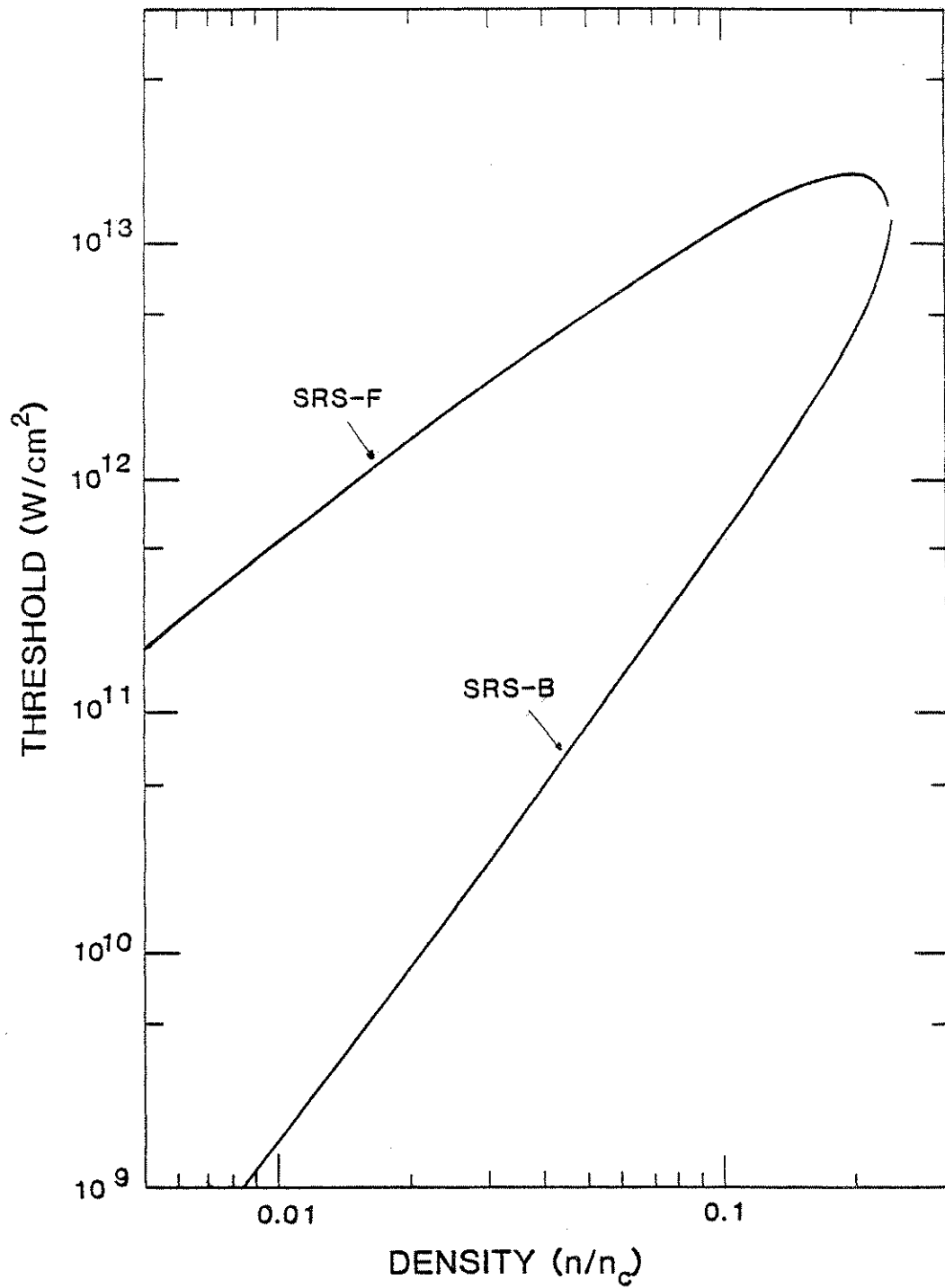


FIG. 2.2. Collisional threshold for SRS-B and SRS-F vs. plasma density for a 0.35  $\mu\text{m}$  laser and a plasma temperature of 1 keV.

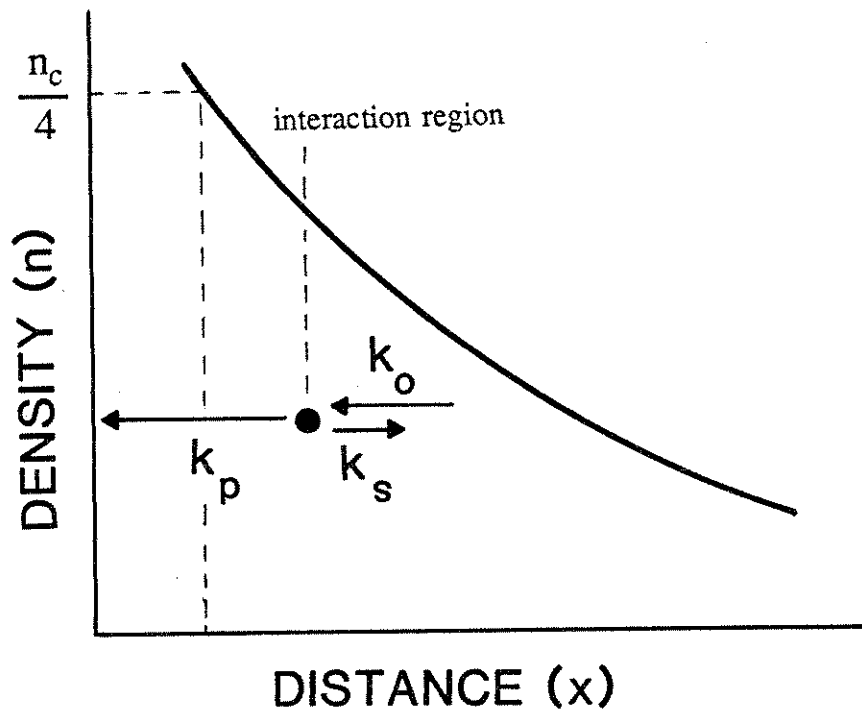


FIG. 2.3. Local SRS-B k-matching in an inhomogeneous plasma.

$$\gamma_p = \frac{v_{gp}}{\zeta} \quad (2.29a)$$

and

$$\gamma_- = \frac{v_{g-}}{\zeta} \quad (2.29b)$$

Here,  $v_{gp,-}$  is the group velocity of the plasma wave and the scattered e.m. wave, and  $\zeta$  is the length of the interaction region. The length of the interaction region is defined as the distance between the turning points of the WKB problem:

$$\int_0^{\zeta} \Delta k(x) dx \approx 1/2 \quad (2.30)$$

where  $\Delta k = k_0 - k_p - k_-$ . In the case of a linear density profile,  $\Delta k \approx x[dk_p(0)/dx]$ , which gives  $\zeta^2 \approx (dk_p/dx)^{-1}$ . Substituting this expression for  $\zeta$  together with equations (2.29) into eqn. (2.26) we get the inhomogeneous threshold for a linear density profile:

$$\left[ \frac{v_0}{c} \right]^2 = \frac{2}{k_p L} \quad (2.31)$$

which is weakly dependent on the plasma density. Here,  $L$  is the density scalelength defined as

$$L^{-1} = \frac{1}{n} \frac{dn}{dx} \quad (2.32)$$

Eqn. (2.31) can be expressed in a more useful form in terms of the pump intensity and pump wavelength in vacuum:

$$I\left(\frac{\text{W}}{\text{cm}^2}\right) \approx \frac{4 \times 10^{17}}{L(\mu\text{m})\lambda_0(\mu\text{m})} \quad (2.33)$$

Figure 2.4 shows the inhomogeneous threshold for SRS-B in a plasma with a linear profile vs. the plasma scalelength. We see that for pump intensities on the order of  $10^{15}$  W/cm<sup>2</sup>, millimeter plasma scalelengths are necessary in order to exceed the threshold.

There are some situations in which the density profile is best approximated by a parabola as is the case of plasmas created from exploding thin foils. Therefore, it is useful to find an expression for the convective threshold of SRS-B in a plasma with a parabolic density profile.

If we assume a density profile of the form

$$n = n_0 \left[ 1 - \frac{x^2}{L^2} \right]$$

the mismatch coefficient will be

$$\Delta k \approx \frac{x^2}{2} \frac{d^2 k_p}{dx^2}$$

for instabilities occurring at the peak of the plasma density. Thus, the threshold

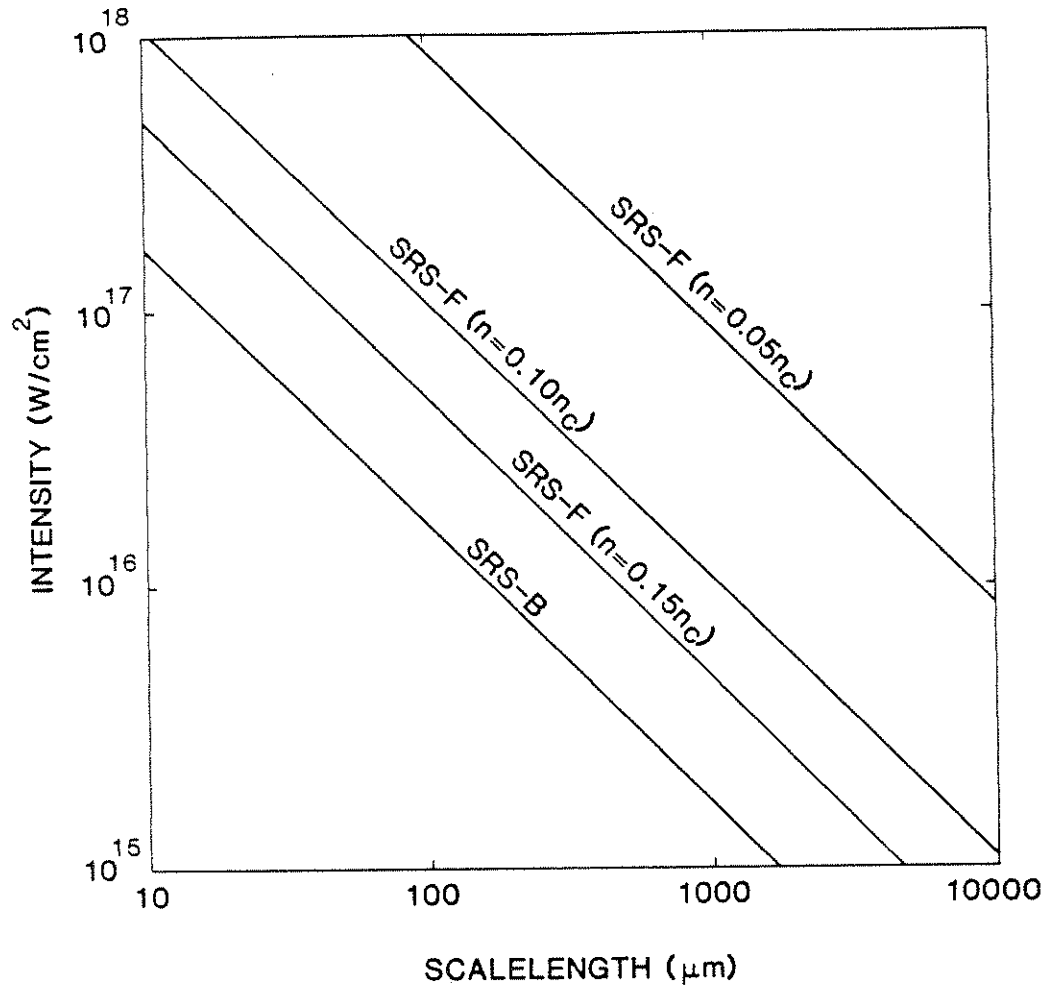


FIG. 2.4. Convective thresholds for SRS-B and SRS-F vs. plasma scalelength for a  $0.35 \mu\text{m}$  laser and  $k\lambda_D \ll 1$ .

for a parabolic profile is

$$I\left(\frac{W}{\text{cm}^2}\right) \approx \frac{5 \times 10^{15}}{\lambda_o^{2/3}(\mu\text{m})L^{4/3}(\mu\text{m})} \left[\frac{n_c}{n}\right]^{1/3} T_e^{1/3}(\text{eV}) \quad (2.34)$$

In the intermediate density regime,  $\omega_o \approx 3\omega_p$ , the threshold for SRS-B in a plasma with a parabolic profile can be much lower than that for a plasma with a linear profile with the same scalelength for modest temperatures. At low densities,  $\omega_o \approx 10\omega_p$ , other energy dissipation mechanisms such as Landau damping dominate the behavior of the threshold.

## 2.6 STIMULATED RAMAN FORWARD SCATTER

One of the characteristics of forward scattering is that the involved density perturbations possess a smaller wave vector than the ones responsible for back-scattering. This can be seen from the k-matching construction shown in fig. 2.1. For SRS-F,  $k_p$  is given by:

$$k_p = k_o - k_-$$

or,

$$k_p = \frac{\omega_o}{c} \left[1 - \frac{n}{n_c}\right]^{1/2} - \left[1 - 2 \left[\frac{n}{n_c}\right]^{1/2}\right]^{1/2} \quad (2.35)$$

We can see that the largest value that  $k_p$  can take is  $k_o$  at  $n_c/4$ , whereas at low densities  $k_p$  tends to  $\omega_p/c$ . Thus, near  $n_c/4$ , the  $D_+$  term is non-resonant and can be neglected in eqn. (2.18). This means that the expressions (2.23), (2.26), and

(2.31) for the growth rate and threshold for SRS-B will also hold for SRS-F in this region. The only difference is that now  $k_p$  is given by eqn. (2.35) rather than by eqn. (2.24). Since  $k_p$  for SRS-F is smaller than for SRS-B, the SRS-F threshold will be higher and the growth rate will be smaller than for SRS-B.

The collisional threshold and the convective threshold for SRS-F are shown in Figs. 2.2 and 2.4.

At very low densities,  $k_p \rightarrow \omega_p/c$ , and the first term on the right hand side of eqn. (2.20) becomes very small. In this case, both side bands are nearly resonant and the  $D_+$  term cannot be neglected in eqn. (2.18). Keeping both terms in the dispersion relation, the growth rate and convective threshold in this limit take the form:

$$\delta = \frac{\omega_p^2 v_o}{\sqrt{8} \omega_o c} \quad (2.36)$$

and

$$\left( \frac{v_o}{c} \right)^2 \approx \frac{4}{k_o L} \left[ \frac{\omega_o}{\omega_p} \right]^3 \quad (2.37)$$



## CHAPTER III

### PROPAGATION OF WAVES IN A RIPPLED PLASMA

The usual SRS theory that predicts the behavior of the scattered spectrum assumes that the plasma density variations are negligible on the scale of the plasma wavelengths involved in the scattering process. However, due to the high SRS threshold, whenever one excites the SRS instability, stimulated Brillouin scattering (SBS) will also invariably be excited. SBS excites an ion wave which ripples the plasma density with wavelengths smaller than that of the plasma waves from SRS. Thus, it is important to understand the behavior of the plasma waves and e.m. waves in the presence of a rippled plasma.

Recently, there has been a renewed interest in the study of the propagation of high frequency plasma waves in the presence of ion acoustic fluctuations. In the corona of a laser fusion pellet ion fluctuations can arise from several sources. First, The stimulated Brillouin scattering (SBS) instability can generate fairly large amplitude,  $n_1/n_0 \approx 10\%$ , ion waves with wave numbers twice that of the incident e.m. wave<sup>72</sup>. SBS can occur from very low densities, all the way up to the critical density  $n_c$ . Second, large amplitude ion waves with a wide spectrum in  $k$  space have been seen near the quarter critical density layer and are thought to be associated with the  $2\omega_p$  decay instability<sup>73-76</sup>. Finally, ion acoustic turbulence driven by the return current can occur near the critical density<sup>77</sup>. Ion fluctuations can influence the laser light absorption<sup>78-84</sup> and may affect the high frequency instabilities which are capable of producing high energy electrons in

laser fusion pellets. Early theoretical work in this field was carried out by Kaw et al.<sup>85</sup>. They studied the energy transfer between the primary plasma wave and its spatial harmonics which were coupled to the primary wave via the ion fluctuations. Later, Nicholson<sup>86</sup> showed that the density modulations tended to reduce the spatial and temporal parametric instability growth rates. Rozmus et al.<sup>87</sup> analyzed the threshold conditions for SRS-B from an underdense plasma in the presence of the ion acoustic fluctuations. They concluded that under certain conditions, the threshold for SRS-B could be reduced by the presence of the ion fluctuations. Barr and Chen<sup>89</sup> studied the harmonic excitation of the plasma wave from SRS in the presence of a rippled density induced by SBS at very low densities. The ripple was found to reduce the usual growth rate of SRS and also permitted the presence of other decay modes. In a subsequent paper, Rozmus and co-workers<sup>59</sup> presented a model for SRS in the presence of SBS and non-linear effects described by the Zakharov equations. One of the main results of this model is that it predicts enhanced damping and collapse phenomena in the region where the Raman gap exists. Recently, Aldrich et al.<sup>88</sup> studied the Langmuir collapse of the plasma waves when SRS is excited in the presence of SBS. On the experimental side, Darrow et al.<sup>90</sup> have shown very recently the coupling between the primary wave and its spatial harmonics when such a plasma wave is excited through the beating of two laser lines acting resonantly with the plasma frequency.

In this chapter we address the effects of a density ripple on the propagation of both e.m. waves and electron plasma waves. The ripple is assumed to be stationary in time. We find that the presence of a ripple in the plasma density introduces "forbidden" bands of frequencies (evanescent modes) for both types of

waves; the plasma waves being the most affected for typical values of the ripple amplitude.

As we will see in chapter VI, the presence of these forbidden bands can split the SRS radiation at  $\omega_0/2$  into a red and a blue shifted satellite. The blue satellite is found to be more sensitive to the ripple height and plasma temperature than the red peak. Experimental measurements of such splitting show a good qualitative agreement with the theoretical predictions presented here.

### 3.1. THEORY

Consider an infinite plasma whose density  $n'_0$  varies sinusoidally in space about an average density value  $n_0$  as given by

$$n'_0(x) = n_0(1 + \epsilon \cos k_i x) \quad (3.1)$$

Here,  $\epsilon$  is the relative amplitude of the ripple and  $k_i$  its wave vector in the  $x$  direction. An electromagnetic wave propagating in such plasma will satisfy the wave eqn.

$$\nabla^2 E_T = \frac{4\pi}{c^2} \frac{\partial J}{\partial t} + \frac{1}{c^2} \frac{\partial^2 E_T}{\partial t^2} \quad (3.2)$$

where the current density  $J$  is given by

$$J = -nev \quad (3.3)$$

The transverse electric field  $E_T$  and the electron velocity  $v$  are related by the eqn.

of motion

$$\dot{v} = -\frac{e}{m}E_T \quad (3.4)$$

Let us perturb the plasma such that

$$n = n_0' + n_1 \quad (3.5)$$

and

$$v = 0 + v_1 \quad (3.6)$$

Combining eqns. (3.2)-(3.6) and linearizing in the perturbations we get

$$c^2 \frac{\partial^2 E_T}{\partial x^2} = \omega_p^2 [1 + \epsilon \cos k_i x] E_T + \frac{\partial^2 E_T}{\partial t^2} \quad (3.7)$$

where  $\omega_p^2 = 4\pi n_0 e^2/m$ .

Letting  $E_T(x,t) = E_T(x)e^{i\omega t} + c.c$  and substituting into eqn. (3.7) one gets

$$\frac{d^2 E_T(x)}{dx^2} + \left[ \frac{\omega^2 - \omega_p^2}{c^2} - \epsilon \frac{\omega_p^2}{c^2} \cos k_i x \right] E_T(x) = 0 \quad (3.8)$$

Transforming to the dimensionless variable  $\xi = k_i x/2$  and using the relation  $\cos(2\xi) = 2\cos^2\xi - 1$  one obtains

$$\frac{d^2 E_T(\xi)}{d\xi^2} + \left[ \frac{4(\omega^2 - \omega_p^2 + \epsilon\omega_p^2)}{c^2 k_1^2} - \frac{8\epsilon\omega_p^2}{c^2 k_1^2} \cos^2 \xi \right] E_T(\xi) = 0 \quad (3.9)$$

This relation can be written as

$$\frac{d^2 E_T(\xi)}{d\xi^2} + [B - H^2 \cos^2 \xi] E_T(\xi) = 0 \quad (3.10)$$

which is the Mathieu eqn. Here, we have made use of the definitions

$$B = \frac{4(\omega^2 - \omega_p^2 + \epsilon\omega_p^2)}{c^2 k_1^2} \quad (3.11)$$

and

$$H^2 = \frac{8\epsilon\omega_p^2}{c^2 k_1^2} \quad (3.12)$$

Relation (3.10) represents the behavior of an e.m. wave of frequency  $\omega$  propagating in a plasma with a stationary rippled density.

The case of the propagation of an electron plasma wave in a rippled plasma was considered by Kaw et al.<sup>85</sup> and the relation that they obtained for the longitudinal electric field under similar conditions was

$$\frac{d^2 E_L(\xi)}{d\xi^2} + [b - h^2 \cos^2 \xi] E_L(\xi) = 0, \quad (3.13)$$

where

$$b = \frac{4(\omega^2 - \omega_p^2 + \epsilon\omega_p^2)}{3v_e^2 k_i^2} \quad (3.14)$$

and

$$h^2 = \frac{8\epsilon\omega_p^2}{3v_e^2 k_i^2} \quad (3.15)$$

Here  $v_e$  is the thermal velocity. Notice that eqn.(3.13) is identical to eqn.(3.10) and therefore both the e.m. waves and the electron plasma waves will show a similar behavior. The only difference between both relations is that now  $c^2$  is replaced by  $3v_e^2$ . The parameters  $H$  and  $h$  are related by

$$H^2 = \frac{3v_e^2}{c^2} h^2 \quad (3.16)$$

Thus, we only need to solve eqns. (3.10) or (3.13) in order to get the dispersion relation of both modes.

The fact that  $H^2$  can be much smaller than  $h^2$  for a given ripple amplitude  $\epsilon$ , makes the e.m. waves far less sensitive to the density ripples than the plasma waves, as will be seen latter.

Following Kaw et al., it is possible to express the solution to the eqns.(3.10) or (3.13) as a Laurent series in  $e^{i2\xi}$  multiplied by the factor  $e^{iq\xi}$ . Here,  $q$  is in general a complex quantity. Thus, we can write

$$E(\xi) = \sum_{m=-\infty}^{m=\infty} E_m e^{i(2m+q)\xi} \quad (3.17)$$

where E represents  $E_T$  or  $E_L$ .

Substituting this solution into eqns. (3.10) or (3.13) we get the recursion relation

$$\beta^2 E_{m+1} - [4\alpha^2 - 16(m + \frac{q}{2})^2] E_m + \beta^2 E_{m-1} = 0. \quad (3.18)$$

Here

$$\alpha^2 = \begin{cases} B - \frac{H^2}{2} = \frac{4}{c^2 k_i^2} (\omega^2 - \omega_p^2) & \text{for e.m. waves} \\ b - \frac{h^2}{2} = \frac{4}{3v_e^2 k_i^2} (\omega^2 - \omega_p^2) & \text{for plasma waves} \end{cases} \quad (3.19)$$

and

$$\beta^2 = \begin{cases} H^2 & \text{for e.m. waves} \\ h^2 & \text{for plasma waves} \end{cases} \quad (3.20)$$

Notice that  $\alpha^2$  is independent of the ripple amplitude, and for a given average density  $n_0$  and ripple wave vector  $k_i$ ,  $\alpha^2$  can be regarded as the frequency of the wave;  $\beta^2$  on the other hand, represents the ripple amplitude.

For the primary wave ( $m = 0$ ) we have from the relation (3.18):

$$(\alpha^2 - q^2) - \frac{\beta^2}{4} \left( \frac{E_1}{E_0} + \frac{E_{-1}}{E_0} \right) = 0 \quad (3.21)$$

which represents the dispersion relation of either the e.m. wave or the plasma wave propagating in a rippled plasma. Notice that as the ripple amplitude  $\varepsilon$  goes to zero, we obtain from the dispersion relation (3.21):

$$\alpha^2 - q^2 = 0. \quad (3.22)$$

By letting

$$q = \frac{2k}{k_1} \quad (3.23)$$

we get

$\omega^2 = \omega_p^2 + c^2k^2$  for the e.m. waves and  $\omega^2 = \omega_p^2 + 3v_e^2k^2$  for the plasma waves which are the usual dispersion relations for the e.m. waves and for the plasma waves.

In order to evaluate the dispersion relation (3.21) we still need to know the parameters  $E_{\pm 1}/E_0$ . These parameters can be obtained from the three term recursion relation, eqn. (3.18). This relation can be solved by doing a continued fraction expansion<sup>90</sup> for the unknowns  $E_m$  in terms of  $E_0$ . Thus, we have:

$$\frac{E_m}{E_{m-1}} = \frac{\beta^2}{4\alpha^2 - 16(m + \frac{q}{2})^2 - \beta^2 \frac{E_{m+1}}{E_m}} \quad (3.24a)$$

$$\frac{E_m}{E_{m+1}} = \frac{\beta^2}{4\alpha^2 - 16(m + \frac{q}{2})^2 - \beta^2 \frac{E_{m-1}}{E_m}} \quad (3.24b)$$



from which  $E_{\pm 1}/E_0$  can be obtained in terms of  $E_{\pm 2}/E_{\pm 1}$  and so on. Thus, the expression for  $E_{\pm 1}/E_0$  will be:

$$\frac{E_1}{E_0} = \frac{\beta^2}{4\alpha^2 - 16(1+\frac{q}{2})^2 - \beta^2} \frac{\beta^2}{4\alpha^2 - 16(2+\frac{q}{2})^2 - \beta^2} \frac{\beta^2}{4\alpha^2 - 16(3+\frac{q}{2})^2 - \beta^2} \dots \quad (3.25a)$$

and

$$\frac{E_{-1}}{E_0} = \frac{\beta^2}{4\alpha^2 - 16(-1+\frac{q}{2})^2 - \beta^2} \frac{\beta^2}{4\alpha^2 - 16(-2+\frac{q}{2})^2 - \beta^2} \frac{\beta^2}{4\alpha^2 - 16(-3+\frac{q}{2})^2 - \beta^2} \dots \quad (3.25b)$$

Since one cannot start from  $\frac{E_{\pm 1}}{E_0}$  and move up to higher terms, the opposite is what is normally done. One starts with a large enough value for  $m$  such that

$$\frac{E_m}{E_{m\pm 1}} \approx - \frac{\beta^2}{16(m + \frac{q}{2})^2} \quad (3.26)$$

Then, one substitutes these values for  $\frac{E_{\pm 1}}{E_0}$  into eqns. (3.24a) and (3.24b) and work your way up to reaching  $\frac{E_{\pm 1}}{E_0}$ . The values of  $E_{\pm 1}/E_0$  for given  $\alpha^2$  and  $q$ ,

are substituted into the dispersion relation (3.21) which will be identically satisfied only for certain values of  $\alpha^2$  and  $q$ , or in other words, for certain values of  $\omega$  and  $k$ .

For the plots of the dispersion relation shown below, we used  $m = 10$  in the continued fraction expansion, which gave an error  $< 10^{-5}$  for  $E_{\pm 1}/E_0$ . The values of  $\beta^2$  used were less than 100.

The solid line of Fig. 3.1 represents the ripple-free dispersion relation of either an e.m. wave or an electron plasma wave in terms of  $\alpha^2$  vs.  $q$ . We have represented the dispersion relation in this manner to facilitate the comparison with the corresponding dispersion relations in the presence of a ripple. The symbol  $v$  represents either  $\sqrt{3}v_e$  or  $c$ .

When a ripple is present, the waves can couple with their spatial harmonics which possess the same frequency but their wave vectors are shifted by multiple integers of  $k_i$ . These spatial harmonics are represented by the dotted lines. One should expect a strong interaction between the wave and its harmonics at the points where both dispersion relations intercept each other. This strong interaction can be observed in Fig. 3.2, where the numerical solution for the dispersion relation (3.21) has been plotted for  $\beta^2 = 1$  and  $q$  varying between -4 to 4. Only the real solutions for  $\alpha^2 < 5$  are shown. Now, the dispersion relation does not extend continuously from  $\alpha^2 = 0$  to  $\alpha^2 = 5$ , but instead, it breaks at  $\alpha^2 = n^2$  ( $n=1,2,3,\dots$ ), giving rise to forbidden frequency bands around these values. This figure only shows two bands, a broad band around  $\alpha^2 = 1$  and a much narrower band around  $\alpha^2 = 4$ . These bands come from the Bragg reflection of the waves at intervals  $k = k_i/2$  apart.

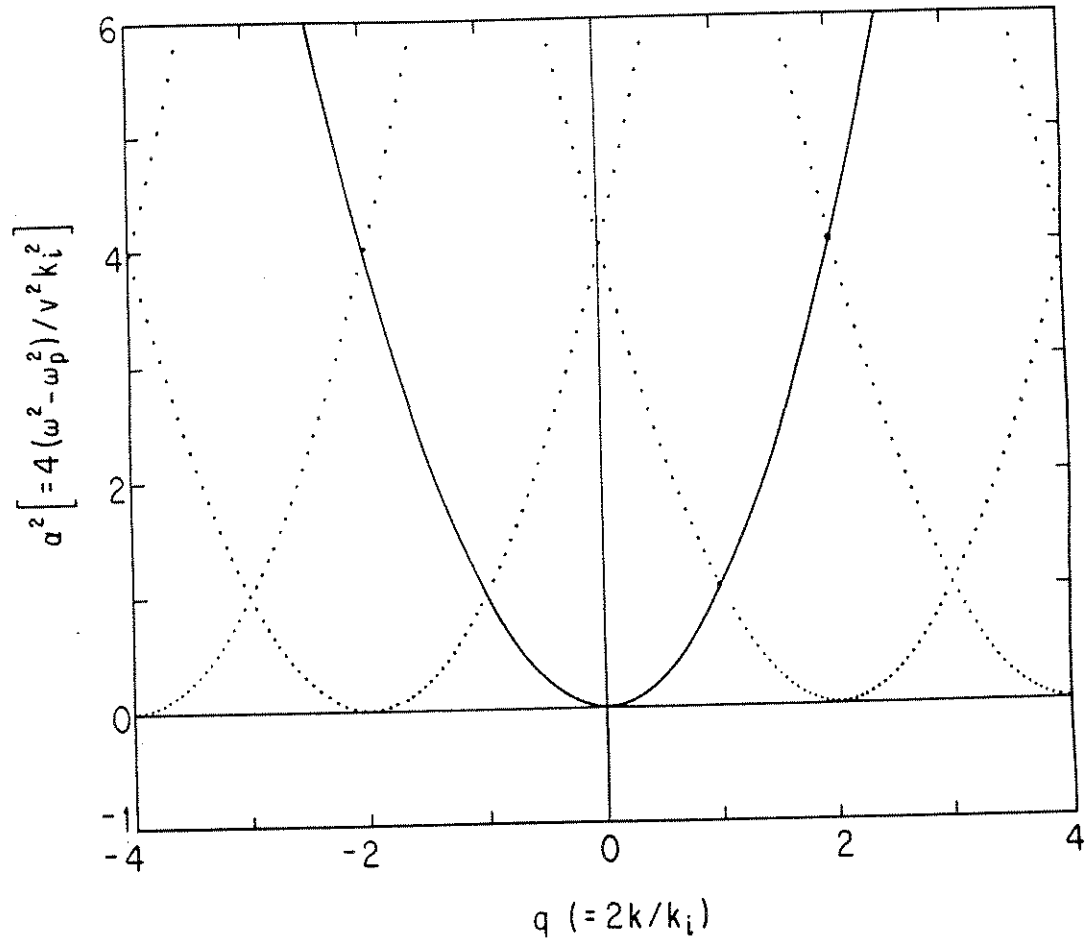


FIG. 3.1. Continuous line :Dispersion relation of an e.m. wave or plasma wave in the absence of a ripple. Dotted curves: dispersion relation of the spatial harmonics of the original wave.

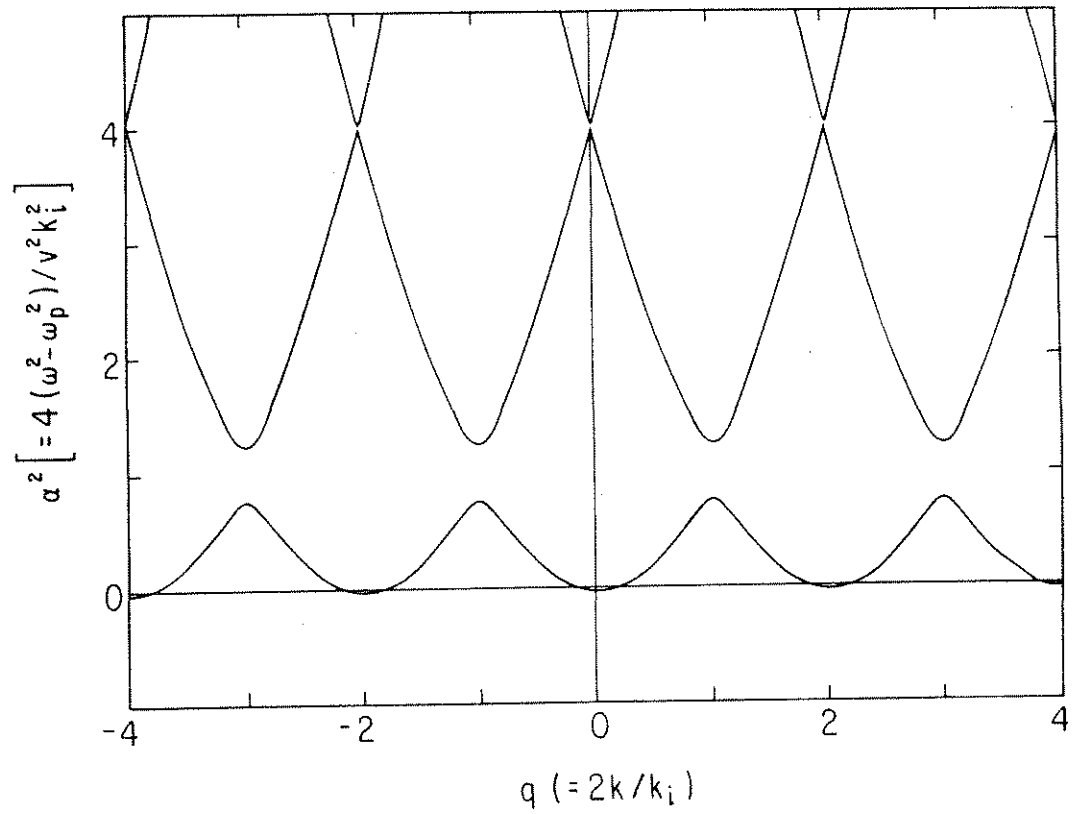


FIG. 3.2. Dispersion relation of a wave propagating in a ripple plasma with  $\beta^2 = 1$ .

The width of the forbidden bands depends on the ripple amplitude, and for  $\beta^2 = 2$  the stop band around  $\alpha^2 = 4$  starts to become clearly resolved as shown in Fig. 3.3. As the ripple increases the stop bands become broader, and for  $\beta^2 = 10$  the dispersion relation already bears little resemblance to the one without any ripple as shown in Fig. 3.4. In Fig. 3.5 we have plotted the first two solutions  $\alpha_-^2$  and  $\alpha_+^2$  for  $q = 1$  as shown in Fig 3.3 for several values of  $\beta^2$ . Waves with frequencies between  $\alpha_+^2$  and  $\alpha_-^2$  possess complex wave vectors  $k$ , its real part being equal to  $\pm(2n+1)\frac{k_i}{2}$  (or  $\pm q = 1,3,5,\dots$ ). These waves are evanescent, and corresponds to the first forbidden band found in solids. For  $\beta^2 \ll 1$  one can estimate the values of  $\alpha_{\pm}^2$  by expanding the dispersion relation (3.21), obtaining

$$\alpha_{\pm}^2 = 1 \pm \frac{\beta^2}{4}. \quad (3.27)$$

The subsequent forbidden bands will be narrower occurring at  $\alpha^2 = n^2$ ,  $n = 1,2,\dots$ . At frequencies outside the the forbidden bands, the roots of the dispersion relation for  $k$  are real, corresponding to propagating waves. In Fig. 3.6 we have plotted the dispersion relation near the first forbidden band for  $\beta^2 = 2$ , showing the real and imaginary parts of  $q$ . In Fig. 3.7 are plotted the values of the imaginary part of  $q$  vs.  $\beta^2$  for  $\alpha^2 = 1$ . Notice that for high enough ripples the wave could be damped 1e-folding in about 0.4 ripple wavelengths ( $\text{Im}(q) = 0.8$ ).

Some of the interesting features of the dispersion relation that are worth mentioning are the following. a) From Fig. 3.3 we see that it is possible to find solutions to propagating waves for  $\alpha^2 < 0$  or, what is the same, for  $\omega < \omega_p$ . This happens for waves with small  $k$ 's and its spatial harmonics. However, for large

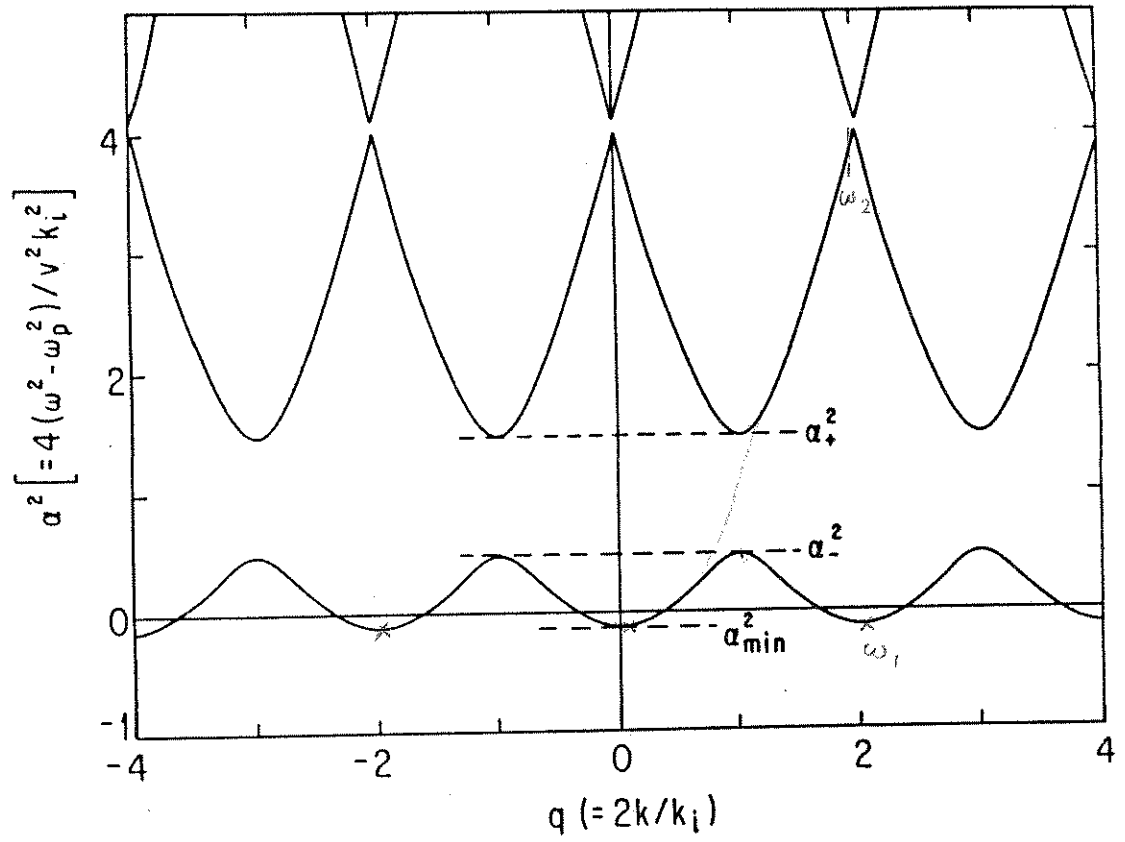


FIG. 3.3. Dispersion relation of a wave propagating in a rippled plasma with  $\beta^2 = 2$ .

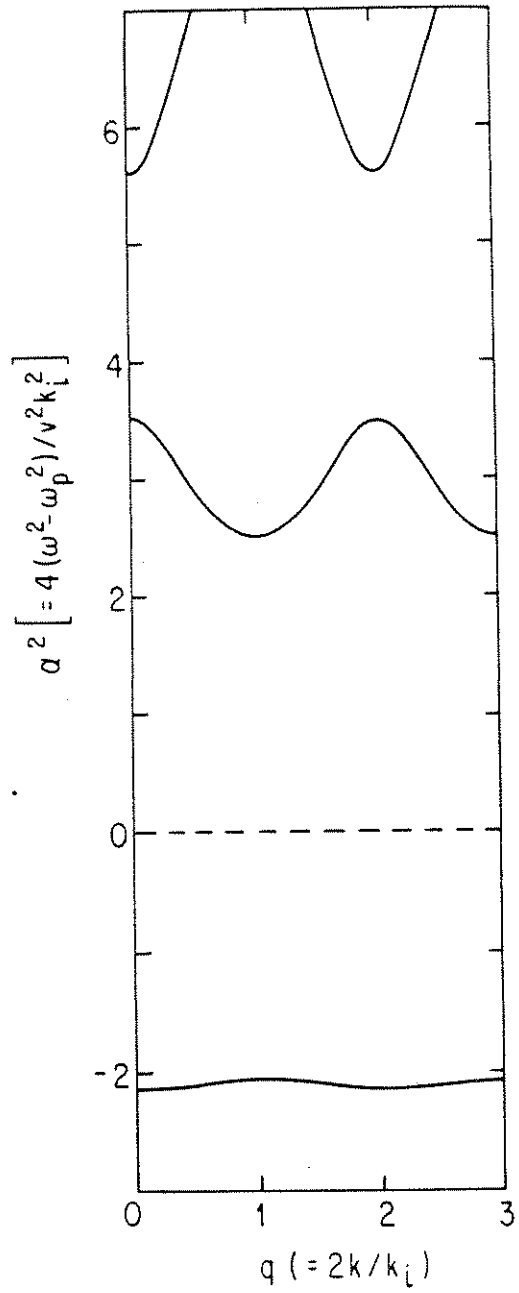


FIG. 3.4. Dispersion relation of a wave propagating in a rippled plasma with  $\beta^2 = 10$ .

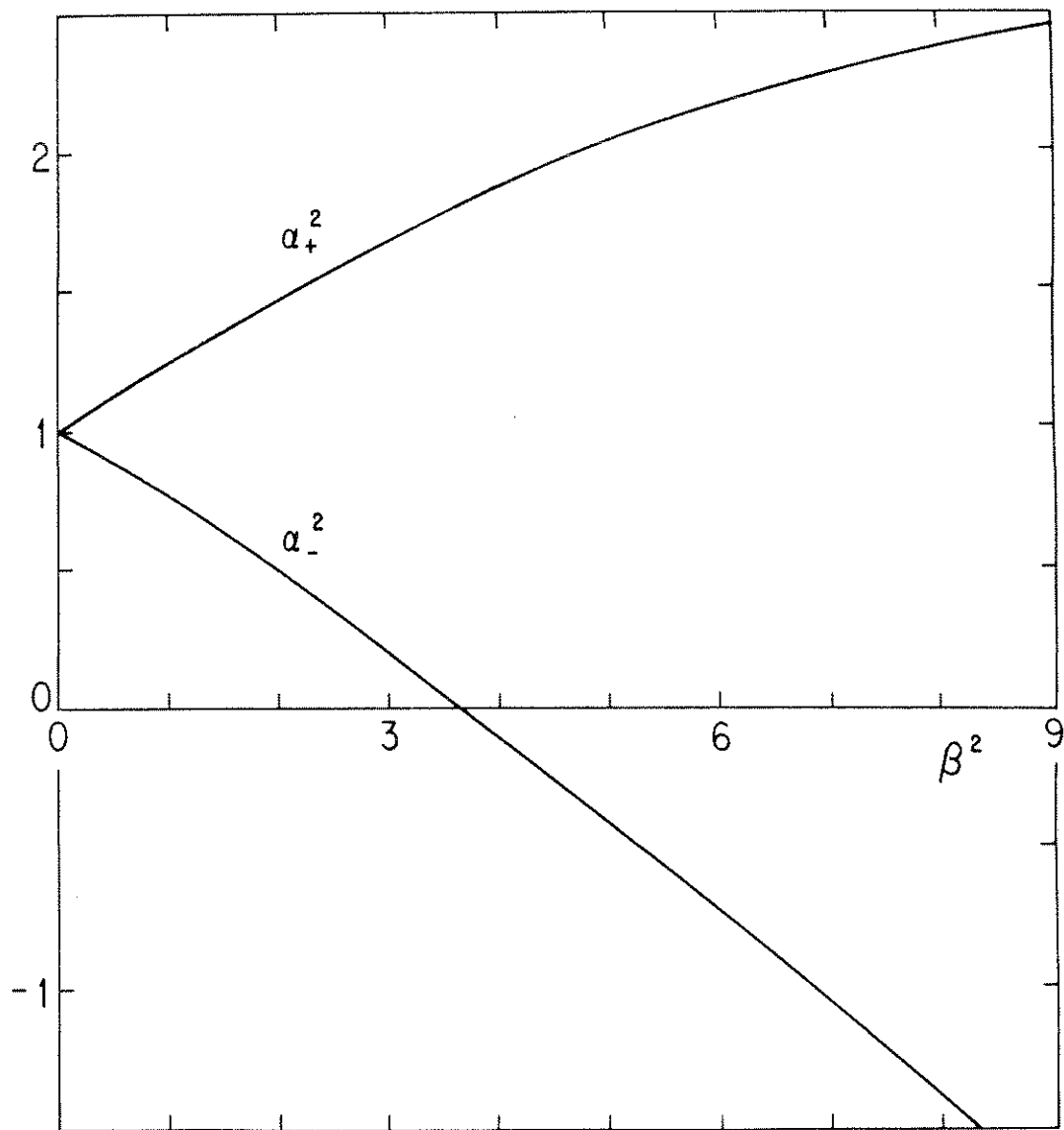


FIG. 3.5. Values of  $\alpha_{\pm}^2$  as a function of  $\beta^2$  for the first forbidden band.



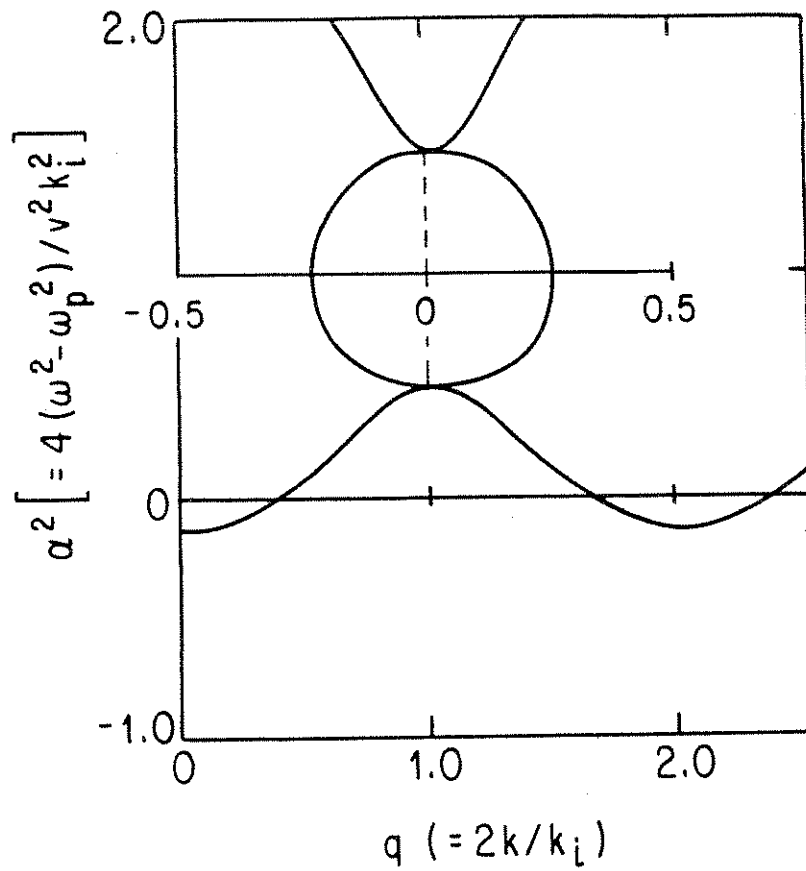


FIG. 3.6. Dispersion relation near the first forbidden band. The real and imaginary parts of  $q$  are shown for  $\beta^2 = 2$ .

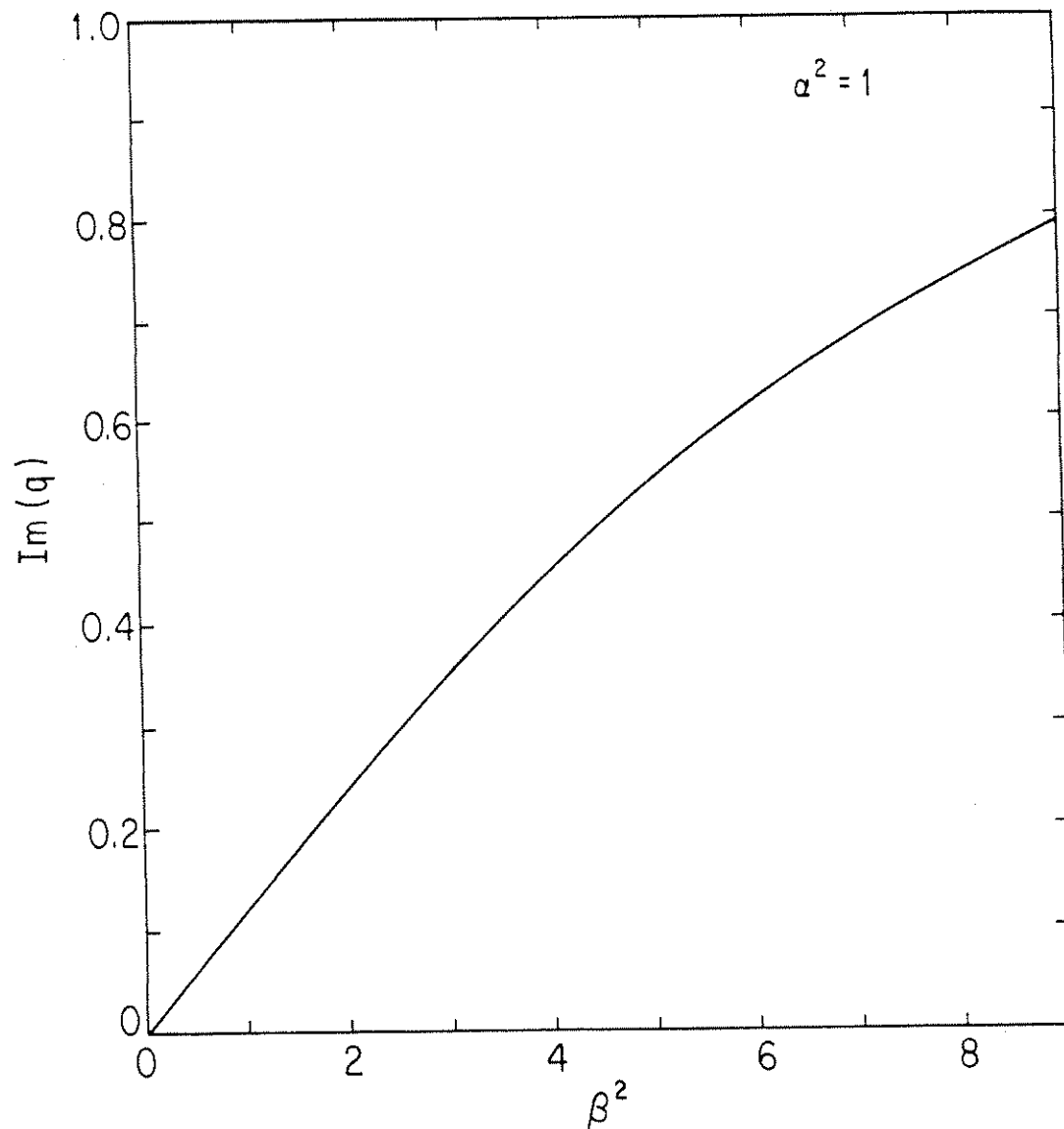


FIG. 3.7. Imaginary part of  $q$  vs.  $\beta^2$  for  $\alpha^2 = 1$ .

used: 800, 2000, and 4000 Å. Two 1/4 meter visible spectrographs were used to obtain the Raman spectra in the backscatter and 45° sidescatter directions. Here, the angles are measured from the backscatter direction which is taken to be at zero degrees as shown in Fig. 4.1(b). The backscatter spectrum was resolved using an S20 subnanosecond resolution streak camera to give the maximum density as a function of time. The sidescatter spectrum was spatially resolved to give an idea of the density profile of the plasma. An array of six absolutely calibrated photo-diodes with a 300 Å bandwidth filter was used to monitor the angular distribution of the half-harmonic light. A transmission calorimeter and an x-ray crystal spectrograph (RAP) were used to obtain the transmitted 0.35 μm beam energy and continuum x-ray emission between 1 and 3 keV, respectively. In addition, two electron spectrometers were used to obtain energy and angular distribution of hot electrons in the range 35 to 350 keV and + 45° to -135°, respectively.

## 4.2 PLASMA DIAGNOSTICS.

Raman-scattered light itself is a diagnostic of the plasma density. We have used this fact to obtain an estimate of the temporally averaged electron density profile of the plasma by space resolving the 45° Raman-sidescattered light and of the maximum electron density of the foil plasma (at the time Raman backscattering is occurring) by time resolving the Raman-backscattered light. The experimentally measured density profile and time evolution enables a comparison to be made with hydrodynamic code simulation of our experiment using the 2-D code LASNEX\*.

---

\* LASNEX simulations were carried out at Lawrence Livermore National Lab by Kent Estabrook

Figure 4.2 shows the schematic of the experimental arrangement for measuring the plasma density profile. Raman-sidescattered light at  $45^\circ$  with respect to the  $0.35 \mu\text{m}$  beam axis, and perpendicular to the density gradient, was imaged using a  $f/2.8$  achromatic lens onto the slit of a  $1/4$  meter space resolving spectrograph with a magnification of 5. The slit size was about  $150 \mu\text{m}$  wide which gave quite a reasonable spectral resolution. The spectra were recorded on Kodak 4143 infrared film. The density profile obtained from a  $2000 \text{ \AA}$  carbon target target is shown in Fig. 4.3. In this particular case information was obtained about the plasma density between  $0.075n_c$  and  $0.095n_c$ . The plasma region between these densities was determined to be roughly  $50 \mu\text{m}$  long in reasonable agreement with code calculation after taking into account the plasma motion.

In view of the rather large horizontal error bars, which are mainly caused by the motion of the plasma, it is not very meaningful to deduce a density scale length from such a measurement. The usefulness of this diagnostic is rather in determining how large the plasma region is which produces the Raman sidescattering. The refraction of the Raman sidescattered light at angles greater than  $45^\circ$  was estimated to have a negligible effect on these measurements because of the shadowing effect of the lead washer on which the target was mounted.

A more useful diagnostic of the density history of the plasma was found to be the time resolution of the Raman-backscattered spectrum. An example of a time-resolved Raman backscatter spectrum from a  $4000 \text{ \AA}$  thick carbon foil is shown in Fig. 4.4(a). In this particular picture both the half-harmonic emission at approximately  $700 \text{ nm}$  and the time fiducial at approximately  $525 \text{ nm}$  are not visible, as a result of attenuation used in front of the streak camera slit.

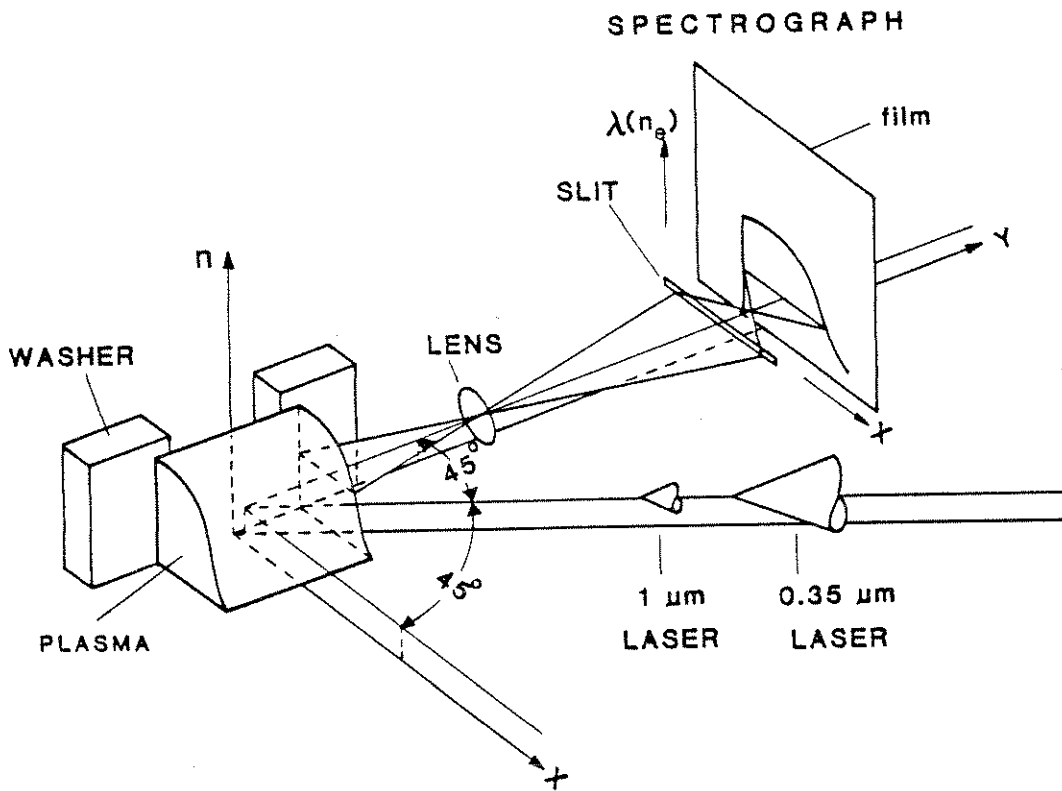


FIG. 4.2. Experimental arrangement for space resolving the Raman sidescattered radiation at  $45^\circ$  with respect to the backscatter direction which gives information about the density profile.

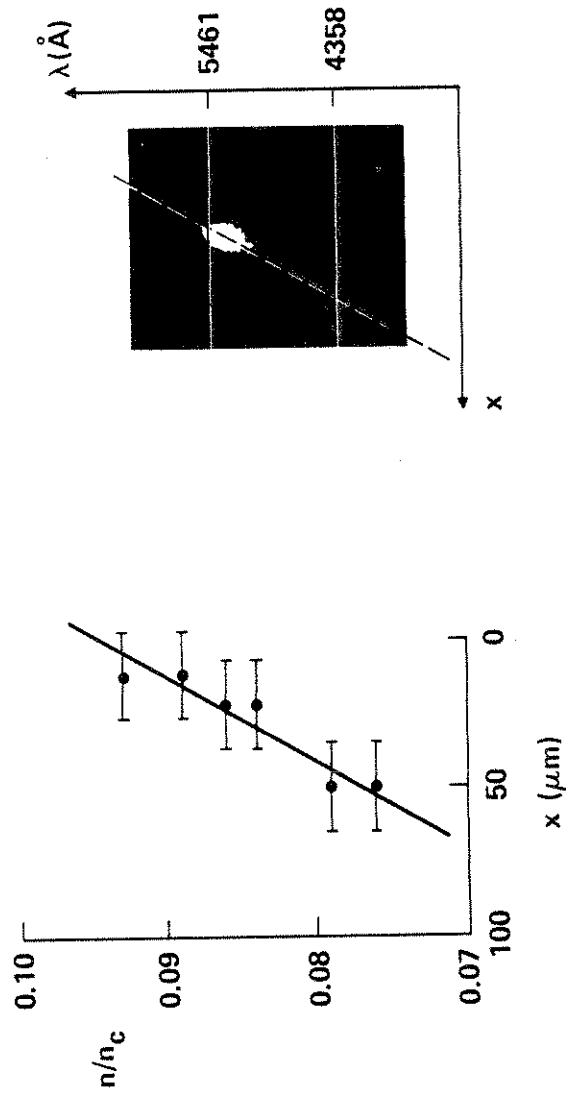
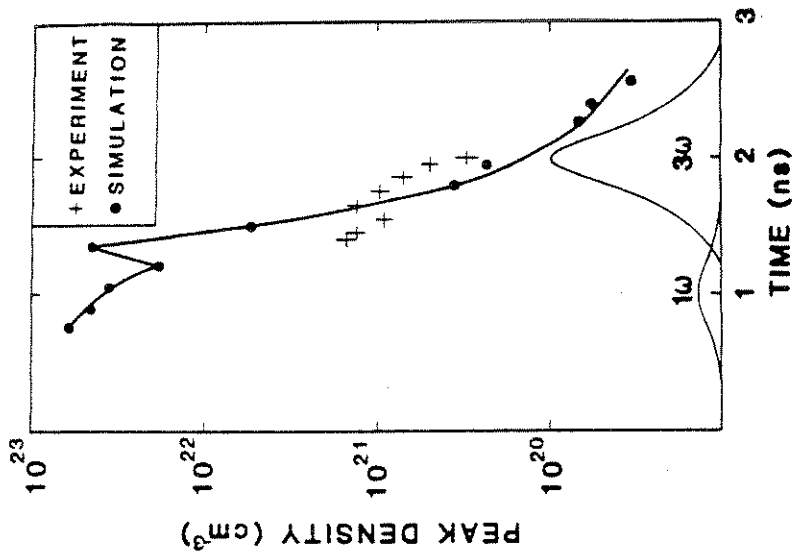
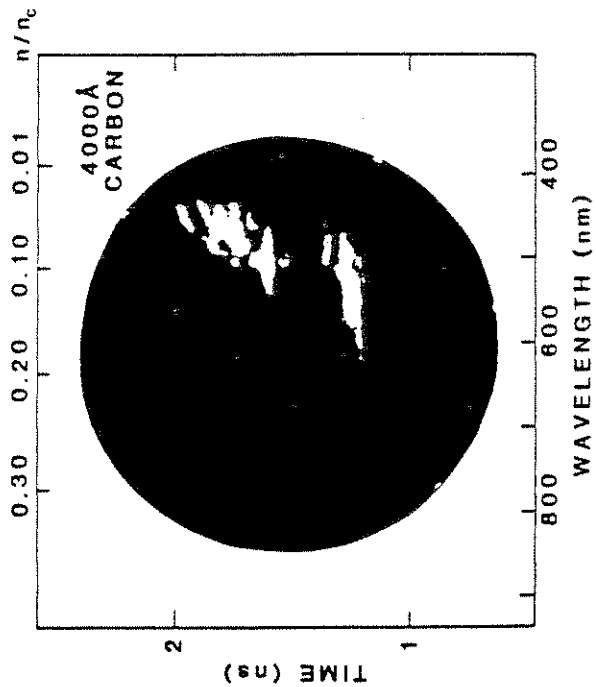


FIG. 4.3. Spatially resolved Raman sidescatter at  $+45^\circ$  for a  $2000 \text{ \AA}$  thick carbon foil target. (a) Typical density profile. (b) Actual photograph corresponding to (a) showing the spatial dependence of the Raman radiation with frequency (or plasma density).



(a)



(b)

FIG. 4.4 Temporal behavior of SRS-B for a 4000 Å thick carbon foil. (a) Typical streak record of SRS-B light. (b) Comparison between experimentally obtained maximum density and 2-D LASNEX predictions. Laser pulses are indicated for comparison.

However, from this and other streak records from 2000 Å and 800 Å thick carbon foils, which essentially show very similar behavior, we deduce that the shift of the long wavelength cutoff to the blue as a function of time is indicative of the peak density of the foil (plateau region), decreasing with time. The experimentally obtained values of the maximum plasma density as a function of time are compared in Fig. 4.4(b) with those from LASNEX simulations. Such comparison leads us to believe that the 800 Å thick foil is already below  $n_c/4$ , the 2000 Å thick foil is below  $n_c$ , and the 4000 Å thick foil is above  $n_c$  within 100 psec of the peak of the 1 μm (marked  $1\omega$ ) prepulse.

Experimentally, the slope of the continuum x-ray emission gives us a plasma temperature of 500 eV for the 800 Å thick and 700 eV for the 2000 Å thick carbon foil plasmas. This is in reasonable good agreement with the simulations which predict a peak temperature of 450 and 750 eV for the 800 Å and 2000 Å carbon foil plasmas, respectively. Backscattered radiation around 0.35 μm (presumably from SBS) was monitored by tilting the targets to avoid any specular back reflection and was found to contain  $\leq 1\%$  of the 0.35 μm ( $3\omega$ ) incident energy for all three foils and occurred in every shot.

### 4.3 RESULTS AND DISCUSSION

#### 4.3.a SCATTERED LIGHT MEASUREMENTS

We believe we are observing backscattered and sidescattered light from a stimulated process for the following reasons. First, the streak data show that the frequency of the scattered radiation varies with the plasma density as would be expected from SRS because of the frequency matching condition. Second, the



time integrated backscattered spectra (Fig. 4.5) show an enhancement by a factor up to  $10^4$  above the bremsstrahlung background in the frequency range expected from SRS. Third, although the experimental value does not agree with the theoretical threshold, there is a threshold for the onset of both back and sidescattering. As the laser intensity is increased there is also a nonlinear growth; however, comparison with theory is once again difficult because both the onset and growth of the instability is strongly influenced in our experiments by plasma heating and hydrodynamics. Finally, the backscattered light above the bremsstrahlung background in the frequency range between 4000 - 6000 Å<sup>o</sup> (presumably from below the quarter critical) is found to be strongly polarized, as shown in Fig. 4.6, in the same direction as the incident light, as would be expected from SRS. We have no evidence that suggests whether we are observing a convective or an absolute instability. Time resolution of the SRS-B light (Fig. 4.4(b)) shows that backscattering is over by the peak of the laser pulse. The threshold for the convective SRS-B for a plasma with a linear density profile is shown in Eqn. (2.33) to be  $I(\text{W}/\text{cm}^2) > 4 \times 10^{17} / \lambda L$ . In order to exceed this threshold during the rise time of the laser pulse, either the laser intensity locally must have been one to two orders of magnitude higher than the estimated average intensity (FWHM), or the plasma scalelength must have been greater than the estimated 50 microns, or a combination of the two. If instead of a linear profile, we assume that the plasma has a parabolic density profile, then for a  $T_e = 750$  eV,  $L = 50 \mu\text{m}$ , and  $n_e = 0.1n_c$  plasma, the threshold for SRS-B becomes  $1 \times 10^{15} \text{ W}/\text{cm}^2$  (see eqn. (2.34)), which is close to the average density used in the experiments. However, in this case one might expect the SRS-B radiation to be emitted from the maximum density region which occurs at the plateau of the

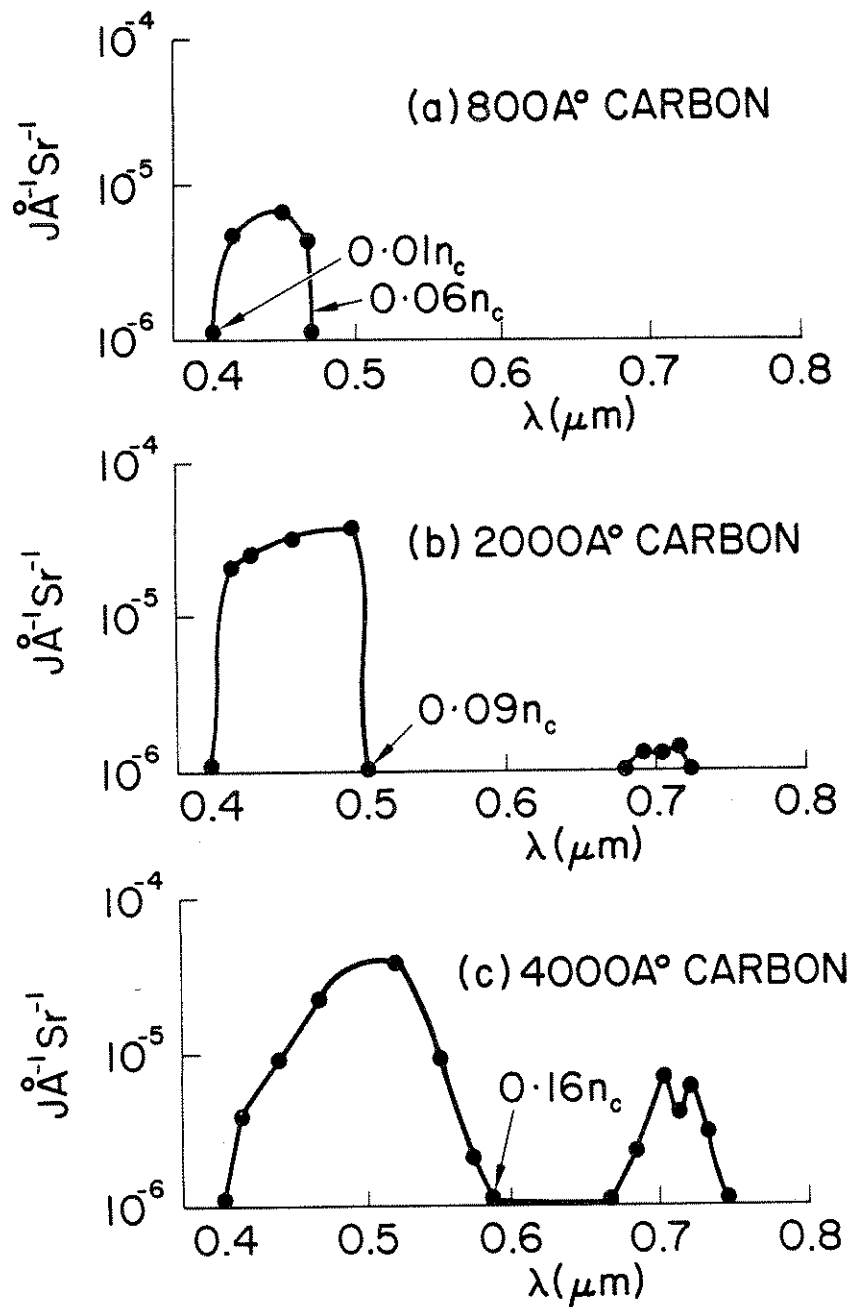


FIG. 4.5 Time integrated SRS-B spectra from carbon foils of various thicknesses.

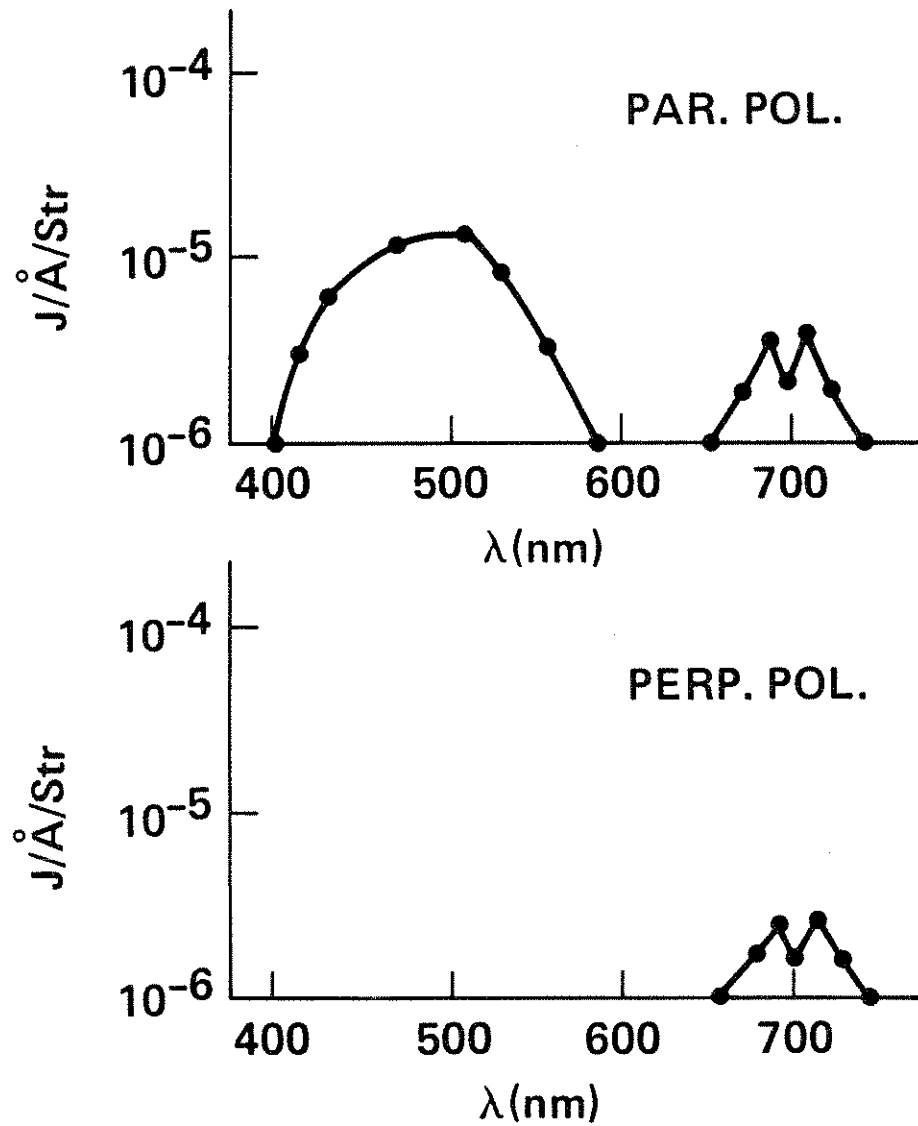


FIG. 4.6. Polarization dependence of SRS-B light. The direction of the plane of polarization is taken with respect to the polarization of the laser beam.

parabolic density profile. Time resolved backscattered measurements show that at a given time SRS-B occurs not only at the peak foil density, but over a wide range of densities. Two dimensional simulations also show strong self-focusing of the 0.35  $\mu\text{m}$  laser beam because of thermal effects. The 0.35  $\mu\text{m}$  laser beam locally heats a 70  $\mu\text{m}$  diameter region of a 2 mm diameter preformed plasma from an initial temperature of 100-150 eV to a final temperature of 500 - 750 eV, depending on the foil thickness. To maintain pressure balance, the density within the heated volume must decrease leading to self-focusing of the laser beam.

As mentioned earlier, the SRS-B light is emitted in a series of 50 -100 psec bursts simultaneously over a wide spectral range. This puzzling behavior has also been seen in 0.53  $\mu\text{m}$  experiments on solid targets<sup>25</sup>. There are two sources of noise from which the Raman instability can grow. The first of these is the bremsstrahlung radiation that is emitted with the appropriate polarization, and second is the Thomson scattering of the incident radiation from thermal density fluctuations in the plasma. Certainly, if bremsstrahlung radiation acts as a noise source for Raman, then it is stronger at shorter wavelengths in the time integrated spectra. If this is the case, then fewer number of e-foldings are required at lower densities (shorter wavelengths) compared to higher densities. In the time resolved spectra, we could not detect the background bremsstrahlung radiation because of the limited dynamic range of the streak camera. The bremsstrahlung radiation from an optically thin plasma is given by<sup>92</sup>

$$\xi(\lambda) = 6.63 \times 10^{21} \left( \frac{n_e}{n_c} \right)^2 \frac{z}{T_e^{1/2}} \frac{1}{\lambda^2} \ln(1.8 \times 10^{-4} T_e \lambda), \quad (4.1)$$

where  $\xi(\lambda)$  is the energy emitted by the plasma at temperature  $T_e$  per unit wavelength, per cubic centimeter, per unit solid angle per unit time in all transverse polarizations, the temperature  $T_e$  is in eV, and  $\lambda$  is in  $\text{\AA}$ . Assuming a linear density profile with a maximum density  $n_c/4$ , a plasma radius  $R = 50 \mu\text{m}$ , and a temperature of 700 eV, the energy radiated between 3500 and 6500  $\text{\AA}$  with polarization parallel to the laser light will range from  $6 \times 10^{-10} \text{ J/\AA}^\circ/\text{Sr}$  to  $2 \times 10^{-10} \text{ J/\AA}^\circ/\text{Sr}$ , being larger at shorter wavelengths. So, even though the radiated thermal energy increases with frequency, it does not vary considerably between 3500 and 6500  $\text{\AA}$  (since  $\hbar\omega \ll kT_e$ ), and SRS in this region grows from essentially the same noise levels. On the other hand, SRS can grow from collective Thomson scattering ( $1/k_p \lambda_D \gg 1$ ) from thermal fluctuations in the plasma. We can estimate the level of Thomson scattering from thermal density fluctuations in the plasma by following Sheffield<sup>93</sup> and assuming a temperature of 750 eV and the plasma length of 0.40  $\mu\text{m}$  (approximately the interaction length in the region of interest). For an average incident energy of 30 J, the estimated Thomson scatter levels between  $0.25n_c$  and  $0.08n_c$  in the backward direction was on the order of  $10^{-10} \text{ J/\AA}^\circ/\text{Sr}$ . Thus, the levels of collective Thomson scattering are apparently on the order of bremsstrahlung. Thus, both processes will give comparable contributions to the noise level.

The number of e-foldings growth from the noise level can be estimated if we assume that the Raman reflectivity is given by the expression<sup>15</sup>

$$\Lambda(1 - \Lambda) = B \frac{\omega_o}{\omega_s} \left[ e^{x(1 - \Lambda)} - \Lambda \right] \quad (4.2)$$

where  $B$  is the noise level at frequency  $\omega_s$ ,  $\Lambda = (\omega_o/\omega_s)r$  where  $r$  is the fraction of light reflected, and

$$x = \frac{k_p^2 L}{8k_s} \left[ \frac{v_{os}}{c} \right]^2 \frac{\omega_p}{\gamma} \frac{\omega_p}{\omega_{epw}} \left[ 1 - \frac{n_e}{n_c} \right]^{-1/2} \quad (4.3)$$

In the above expression  $L$  is the density scalelength and  $\gamma$  is the Landau damping rate. As can be seen from Fig 4.5, we observe  $3 \times 10^{-5} \text{ J/A}^\circ/\text{Sr}$  SRS-B light in the region 4000-5000  $\text{A}^\circ$  when a 2000  $\text{A}^\circ$  thick carbon foil is used. In this wavelength region Landau damping dominates, or is as important as collisional damping. If we take as the noise level  $B = 10^{-10}/30 \text{ J/J/A}^\circ/\text{Sr}$ , then the number of e-foldings will be about 13. The estimated plasma amplitude corresponding to this growth is  $n_1/n \approx 7 \times 10^{-4}$ , which is way below the estimated warm plasma wavebreaking limit which is  $n_1/n \approx 0.17$ . Experimentally, however, the reflectivity showed a weak increase with the intensity, implying that the instability was probably been driven quite close to saturation. The number of e-foldings in the above calculation would be much greater if the reflectivity was normalized to energy in the hot spots instead of to the the incident energy.

Now we discuss the time integrated results. Figure 4.5 shows the time integrated SRS-B spectra. These spectra often showed peaks that were superimposed on top of the bremsstrahlung continuum. Film density at representative frequencies was converted into absolute spectral energy density  $\text{J/A}^\circ/\text{Sr}$ . An absolute calibrated photodiode with appropriate filters to monitor the half-harmonic Raman light placed close to the beam axis was used to calibrate the half-harmonic energy density. The error in the absolute magnitude of the Raman

light at a particular frequency should be less than a factor of 2 because of uncertainties in the spectrally dependence transmission of the optics. A common feature to all the spectra is the short wavelength cutoff at  $0.4 \mu\text{m}$  which is caused by the cutoff filter used in front of the spectrograph. Nevertheless, the Raman spectrum is found to be rapidly decreasing around this wavelength, which can be attributed to strong Landau damping of the plasma waves at these low densities. On the long wavelength side, the Raman spectrum extends to  $0.06n_c$  when the target is a  $800 \text{ \AA}$  thick carbon foil. In this case no half-harmonic emission at  $0.7 \mu\text{m}$  is observed. This is consistent with simulation results which show that the  $800 \text{ \AA}$  foil plasma was already below  $n_c/4$  at the time of the peak of the  $1 \mu\text{m}$  prepulse. However, when we further increase the foil thickness to  $2000 \text{ \AA}$ , then we first observe the onset of the half-harmonic emission which is a unique signature that there is a  $n_c/4$  density layer to interact with the  $0.35 \mu\text{m}$  laser pulse. Also the broadband Raman emission from below  $n_c/4$  now extends up to  $0.09n_c$ . In previous experiments<sup>22</sup> a similar gap between the half-harmonic and the broadband Raman spectrum (which normally extends up to  $0.2n_c$  in solid target experiments) has been attributed to profile steepening at  $n_c/4$  because of  $2\omega_p$  decay instability. Profile steepening at  $n_c/4$  reduces the density scalelength for densities down to the lower shelf density of the steepened profile and consequently raises the Raman threshold in this region. In the present experiments it is unlikely that the gap in the  $2000 \text{ \AA}$  Raman spectrum between  $0.09n_c$  and  $n_c/4$  is caused by profile steepening. This is because this long wavelength cutoff of the broadband spectrum is a function of the foil thickness. For instance, as the foil thickness is increased to  $4000 \text{ \AA}$ , the broadband extends up to  $0.16n_c$ . It is therefore likely that the half-harmonic emission is generated early on in the  $0.35$

$\mu\text{m}$  laser pulse by a process which has a lower threshold than the process which generates the broadband radiation. Both the absolute Raman instability and the two-plasmon decay instability which occurs near  $n_c/4$  have a lower threshold compared to the convective Raman instability which occurs below  $n_c/4$ . The threshold for the process generating the half-harmonic radiation is apparently exceeded in both 2000 and 4000  $\text{\AA}$  cases, but the threshold for the Raman instability below  $n_c/4$  is exceeded in the case of the 2000  $\text{\AA}$  thick foil only when the foil density has dropped to  $0.09n_c$ ; whereas it is exceeded in the case of the 4000  $\text{\AA}$  thick foil by the time the density has dropped to  $0.16n_c$ .

A recent model attributes the presence of the sub-quarter critical frequency band at such low laser intensities to enhanced Thomson scattering<sup>40,51</sup>. According to this theory, the reflected levels of certain frequencies due to incoherent Thomson scattering from thermal fluctuations can be enhanced if the electron velocity distribution possesses a hot tail. Enhanced scattering will result at those frequencies that are scattered from plasma waves whose phase velocity falls on the increasing slope portion of the hot tail.

In an inhomogeneous plasma, the hot electron tail is created by the energetic electrons excited at the  $\frac{n_c}{4}$  layer that stream down the density gradient. Both the fraction and the temperature of the hot electrons affect the band of the enhanced frequencies as shown in Figs. 4.7(a) and 4.7(b) (these figures have been reproduced from ref. 51). The vertical lines represent the predicted enhanced bandwidth and the rectangle just above the abscissa represents the experimental measurements. No experimental data was taken around 200 nm.



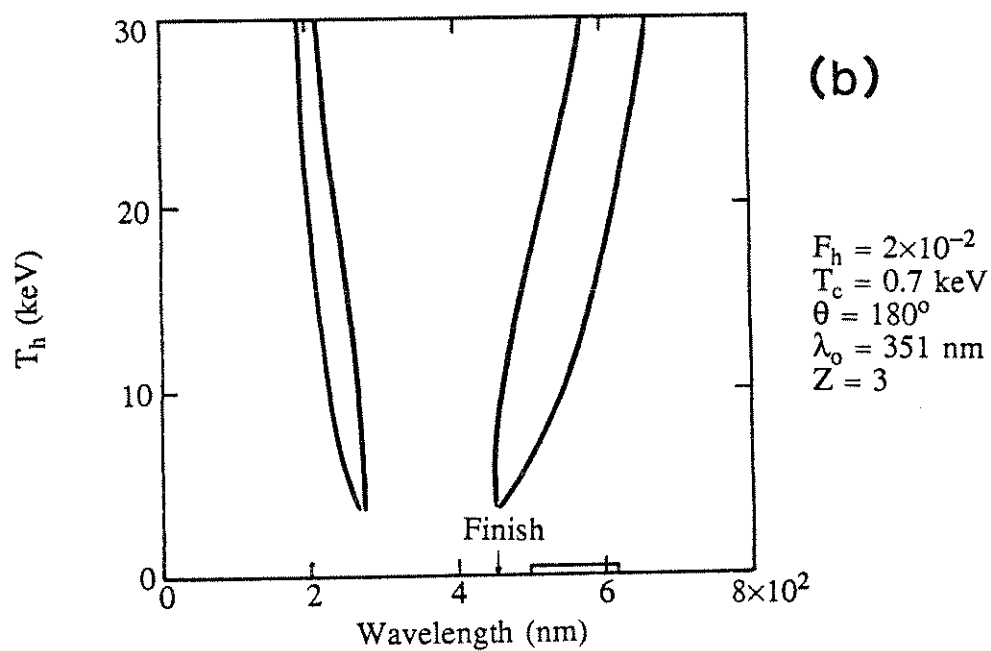
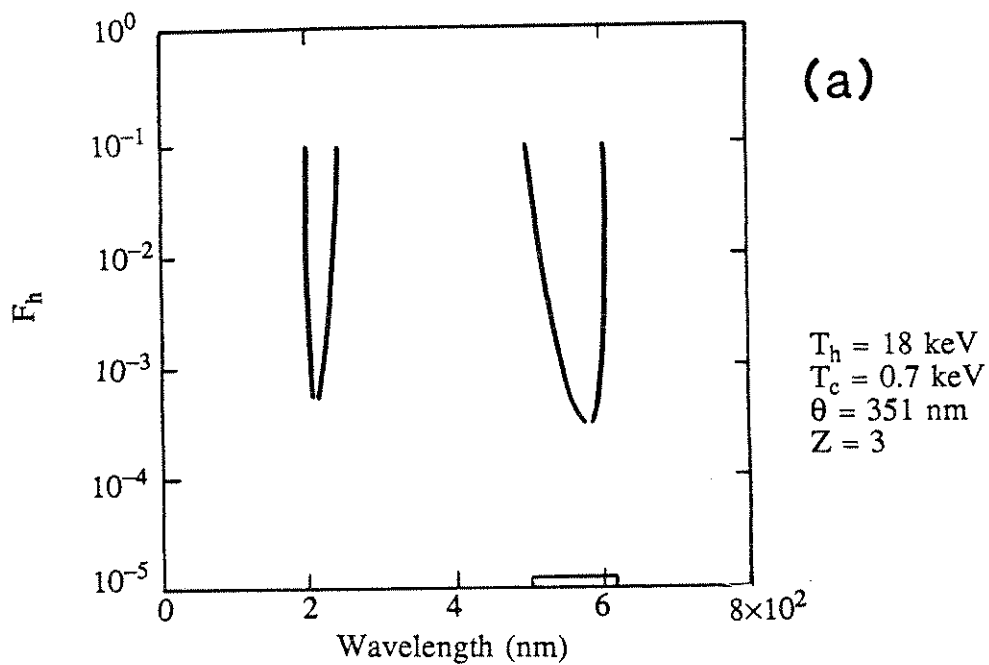


FIG. 4.7. Comparison between the enhanced Thomson scattering theory and the experimental measurements. (a) Variation of the wavelength bands with fraction of hot electrons. (b) Variation of wavelength bands with the hot electron temperature.

Comparisons between experiments and theory show a good agreement as long as one makes three assumptions: 1) A  $n_c/4$  density exists at all times; 2) The hot electron temperature is about 18 keV; and 3) The temperature of the hot electrons decreases during the scattered pulse.

Comparisons of the experimental data with simulations (see Fig. 4.4) indicate that the peak plasma density from all three foils fell well below  $\frac{n_c}{4}$  very early in the main pulse, and that the scattering process is over before the peak of the pulse. If this is the case, then the hot electrons will be generated only very early in the pulse and are not likely to affect the scattered spectrum at later times. It is possible that due to the transverse profile of the laser, hot electrons may be generated from  $n_c/4$  regions near the edge of the plasma while scattered light occurs from the central core. In that case, the fraction  $F_h$  of hot electrons will decrease considerably and the enhanced frequency band will get narrower and will shift towards the red contrary to what it is observed. Also, since the scattering is over before the peak of the pulse, there is no reason why  $T_h$  would decrease, shifting the enhanced band towards the blue.

Another difficulty of this model, as an explanation for the observed broadband spectrum, is that the measured scattered intensities are much higher than those predicted by this model. We conclude then that the enhanced Thomson scatter may be a noise source for the observed spectrum rather than being responsible for it.

#### 4.3.b HOT ELECTRON GENERATION FROM FOIL TARGETS

Concurrent to spectral measurements reported here, the characteristics of the high-energy electron emission from these preformed plasmas were investigated by H. Azechi and N. Ebrahim of Yale University. These measurements were carried out by employing two  $180^\circ$  focusing magnetic electron spectrometers with four surface barrier detectors, each, as detection elements. For these studies the targets were oriented at  $45^\circ$  with respect to the laser axis to reduce the refraction of  $2\omega_p$  decay plasma waves because of the density gradient.

Typical electron spectra in the energy range between 35 and 350 keV are shown in Fig. 4.8(a). These measurements were made in the plane of the electric field vector of the laser (p-polarization) and in the direction of the density gradient, i.e.,  $-45^\circ$  with respect to the laser. The error bars denote shot-to-shot variation. The shaded area in Fig. 4.8(a) represents the electron detection threshold set by detector noise level. As can be seen, when an  $800 \text{ \AA}$  carbon foil was used, only the lowest energy channel at 35 keV showed significant electron emission above the background noise. This was also found to be the case at other angles. It will be recalled that at this thickness no half-harmonic emission was observed, and the Raman emission was confined to densities below  $0.06n_c$ . The kinetic energy of an electron moving at the phase velocity of a plasma wave generated by SRS at  $0.06n_c$  is  $\approx 3.7 \text{ keV}$  for  $T_e \approx 500 \text{ eV}$ . If we assume that the maximum amplitude (therefore potential) of the plasma wave is given by the warm plasma wave-breaking limit<sup>94</sup>, then we obtain perturbed density  $n_1/n_0 \approx 0.24$  for our conditions. Since the plasma wave is an electrostatic wave, Poisson's equation gives the maximum potential in the wave frame as  $(n_1/n_0)mv_p^2$ . The maximum energy of an electron moving initially in phase with the wave is thus  $(\frac{1}{2})mv_p^2 \left[ 1 + 2(n_1/n_0)^{1/2} \right]^2$ , which turns out to be 17 keV. Thus

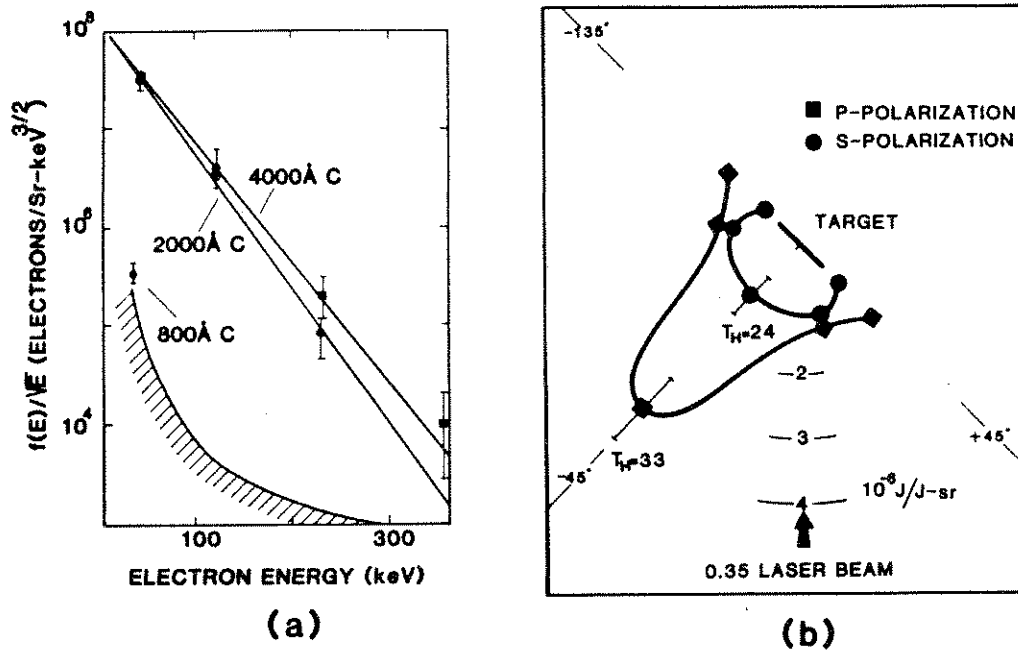


FIG. 4.8. Hot electron emission from thin foil targets. (a) Hot electron spectra from 800, 2000, and 4000 Å thick foil targets at  $45^\circ$  with respect to the laser axis and p-polarization. The shaded area represents the measurement threshold. (b) Angular distribution and polarization dependence of the electron emission for a 2000 Å thick carbon foil.

it is not surprising that no hot electrons were observed on any of the higher energy channels except the lowest channel when an 800 Å thick foil was used.

There was an abrupt increase in the high-energy electron emission at a foil thickness of 2000 Å when the half-harmonic radiation was first observed indicating the presence of the  $n_c/4$  density layer. On the other hand, at this thickness simulations show that there is no critical density layer 100 psec after the peak of the prepulse. This strongly suggests that the electrons are being generated at  $n_c/4$ . On increasing the thickness further to 4000 Å the electron emission did not increase appreciably (more than a factor of 2). Thus, most of the high energy electron emission occurs in the vicinity of  $n_c/4$ , and the contribution of the parametric decay instability and resonance absorption is small in our experiments.

The experimental spectra were fitted with a Maxwellian distribution of the form

$$f(E) = \left(\frac{2}{\sqrt{\pi}}\right)N_0E^{1/2}T_H^{-3/2}\exp(-E/T_H), \quad (4.4)$$

where  $N_0$  is the number of electrons per solid angle,  $E$  is the energy, and  $T_H$  is the hot electron temperature. The electron spectra from a 2000 Å thick carbon foil target had a  $T_H \approx 30\text{--}40$  keV when measured in the plane of the  $E$  vector of the laser (p-pol) and  $T_H \approx 15\text{--}20$  keV when measured out of the plane of the  $E$  vector of the laser (s-pol). These measurements are probably not influenced by the target potential which arises because high-energy electrons escape the plasma, leaving the target with a net positive charge. By connecting the target

directly to the grounded Tektronix 519 oscilloscope<sup>95</sup>, we measured the target potential to be less than 5 kV on a nanosecond time scale.

The observed angular distributions for p- and s- polarizations were spectrally integrated to give the total electron energy in joules per joule of laser energy per solid angle ( $J/J/\text{sr}$ ). This is shown in Fig. 4.8(b) for a 2000 Å thick carbon foil plasma. The p-polarization case shows electron emission more intense than that for s-polarization. The polarization dependence is most pronounced at  $-45^\circ$ . Although refraction of plasma waves by density gradients cannot be ruled out, this systematic polarization dependence points to  $2\omega_p$  decay as the probable generation mechanism for the high energy electrons near the  $n_c/4$  density layer. The electron emission with p-polarization at  $+45^\circ$  and  $-135^\circ$  is not as strong as that at  $-45^\circ$ , probably because of partial shadowing effect of the washer used to mount the target foil. No measurements of the electrons in the forward direction within the cone angle of the laser beam were carried out, since a significant amount of laser energy is transmitted by the foil targets.

The main findings of the experiments were the following:

- 1- We have observed Raman back and sidescatter apparently below the convective threshold for a linear profile.
- 2- The SRS-B spectrum shows a gap near the quarter critical density and a wavelength cutoff near 400 nm.
- 3- The spectrum shows a splitting of the half-harmonic light. This will be discussed further in Chapter VI.
- 4- The broadband spectrum between 400 and 600 nm was strongly polarized in the same direction as the incident laser, as would be expected in Raman scattering, whereas the half-harmonic radiation showed no preferred polarization. The

depolarization of the half-harmonic may be indicative of a strongly polarized rippled  $n_c/4$  or Faraday rotation due to localized magnetic fields in this region.

5- High energy electrons were observed from plasmas with densities below  $n_c$ . The generation mechanism seems to be more efficient at  $n_c/4$ . The angular distribution and polarization dependence suggest  $2\omega_p$  decay as such a mechanism.

6- The length of the plasma region where SRS sidescatter was occurring was estimated to be on the order of 50  $\mu\text{m}$ .

7- The levels of backscattered light were about  $10^{-4}$  %. Such low scattered levels and the small plasma lengths obtained from the foils indicate that SRS-B was probably being excited locally where the laser intensity was one or two orders of magnitude higher than the average intensity.

The fact that plasma lengths on the order of 50  $\mu\text{m}$  were obtained with the foil targets led us to look for another plasma source that would simulate better the dimensions of a plasma from reactor-size pellet (millimeter plasma scalelengths). Foam targets offered us that option. These targets are very low density polymers filled with voids such that the laser beam can penetrate and ionize the inner walls of the target. Another advantage of these targets is that the plasma hydrodynamics is minimized; this makes easier the interpretation of the time integrated scattered spectrum, since the plasmas remain confined for longer periods of time.

We have carried out experiments with foam targets of variable average density and it is the purpose of the next chapter to discuss our findings.

## CHAPTER V

### EXPERIMENTS WITH FOAM TARGETS

There is mounting evidence from Lawrence Livermore National Lab, Ecole Polytechnique (France), Rutherford Lab (U.K), and the Institute for Laser Engineering (Japan) that the laser-to-plasma coupling efficiency is increased as one goes from 1  $\mu\text{m}$  radiation to shorter wavelengths. Absorption, by predominantly inverse bremsstrahlung, up to 90% is observed at 0.25  $\mu\text{m}$  (4th. harmonic of 1  $\mu\text{m}$ ) at an intensity of  $2 \times 10^{15}$  W/cm<sup>2</sup>, using nanosecond or less long pulses, and a spot size of several hundred  $\mu\text{m}$ . Although this is good news for laser fusion, the crucial question is if this high absorption into a thermal electron population will scale to plasmas that are millimeter scalelength created by many nanosecond long laser pulses. Such long scalelengths may lower the threshold for high frequency instabilities and deposit the laser energy in hot electrons.

We tried to create such long plasmas with a modest laser energy of less than 50 J in  $\approx 1$  ns using a 0.53  $\mu\text{m}$  laser. Experiments on slab targets with such pulses give plasma scalelengths of around 50-100  $\mu\text{m}$ . Our experiments with foils did not produce substantially longer plasmas, even when the separation between the prepulse and the main pulse was varied. The plasma scalelength was limited basically by the focal spot size. To create substantially longer plasmas, therefore, we used a novel technique: foam targets whose average density was much less than the solid density. We discuss these experiments in this chapter.



Figure 2.4 shows, following Estabrook and Krueer<sup>24</sup>, the thresholds for SRS vs. the plasma scalelength in the case of a linear density profile for a 0.35 micron laser and several densities for which  $k_p \lambda_D \ll 1$ . The SRS-B threshold depends weakly on the plasma density. It can be seen that in order to overcome the threshold, very high laser intensities and/or very long plasma scalelengths are required. This condition is particularly severe for SRS-F and probably that is the reason why it has not yet been conclusively seen. Also, for density profiles decaying not faster than the exponential  $n = n_0 \exp(-x/L)$ , the inhomogeneous threshold for SRS-B decreases as the plasma density increases. Thus, we might expect SRS-B to be the strongest in regions close to the quarter critical density ( $n_c/4$ ). However, contrary to expected, several research groups working with 0.35, 0.53 and 1.06  $\mu\text{m}$  lasers have reported a "gap" in the backscattered spectrum at densities near the quarter critical layer<sup>96</sup>.

Figure 5.1 shows the time evolution of such a spectrum obtained by focusing a 0.35 micron, 1 ns FWHM laser pulse on a solid flat Al target. The focal spot size was of approximately 70 microns giving an average laser intensity of  $10^{15} \text{W/cm}^2$ . On the right hand side of Fig. 5.1, near  $\lambda = 700 \text{ nm}$ , the typical splitting of the half harmonic radiation (presumably originating at  $n_c/4$ ) can be seen<sup>28</sup>. To the left of this quarter critical region is the Raman emission from the sub-quarter critical plasma, which does not increase monotonically up to the quarter critical layer. Instead, there is a distinct gap between 600 nm and 700 nm. Moreover, this gap is present throughout the pulse together with the half harmonic radiation. It corresponds to a lack of Raman backscatter between  $0.17n_c$  and  $0.25n_c$ , where  $n_c$  represents the critical density for a 0.35 micron laser.

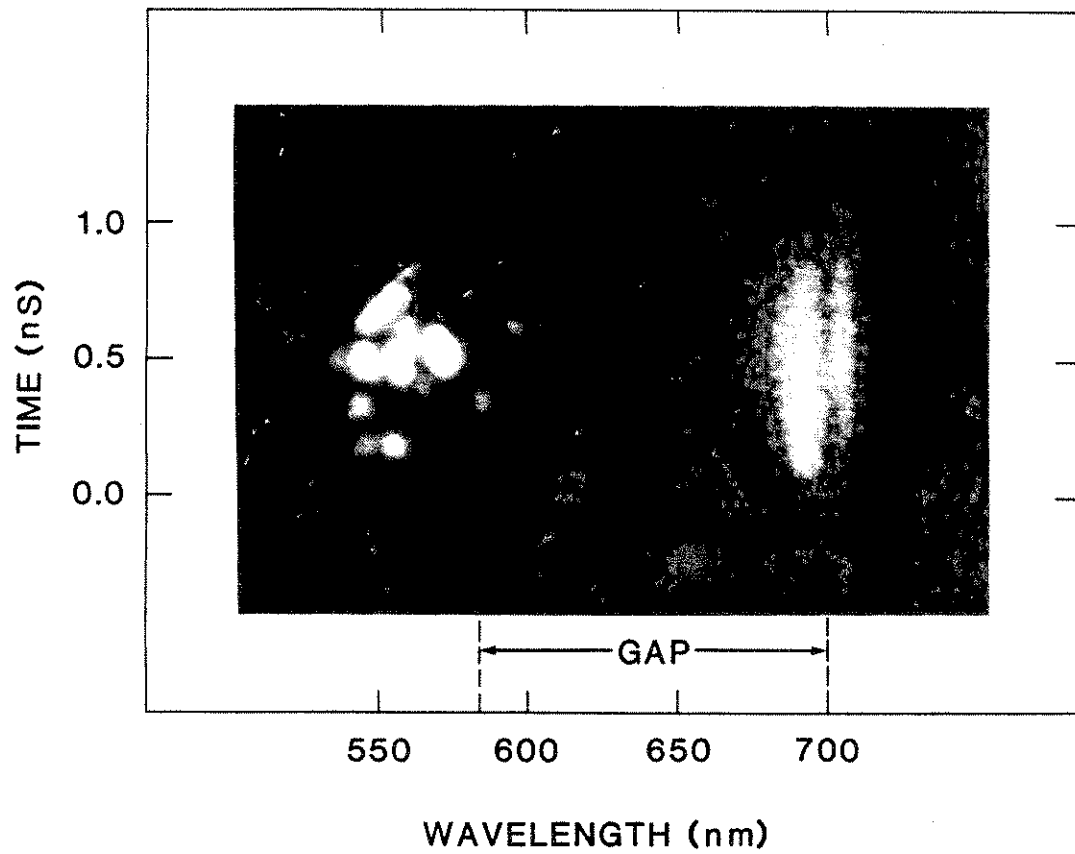


FIG. 5.1. Backscatter spectrum from a solid Al target showing the Raman gap between the half-harmonic radiation and the sub quarter critical spectrum.

This gap has been attributed to the steepening of the density profile due to the presence of the  $2\omega_p$  decay instability at the quarter critical density layer<sup>97</sup>. Unfortunately, direct interferometric probing for the evidence of the steepened profile at these high densities ( $2.5 \times 10^{21} \text{ cm}^{-3}$ ) is very difficult. Also, more recently, this behavior of the Raman spectrum has been explained in terms of the enhanced Thomson scattering from the energetic electrons generated at  $n_c/4$  that stream down the density gradient<sup>40,51</sup>.

Both of these explanations of the spectral gap (steepening of the density profile and enhanced Thomson scattering) require the presence of the quarter critical density layer. Thus, a good way of isolating these two phenomena from those independent of the presence of the  $n_c/4$  density layer would be to create long plasmas of variable densities where the SRS threshold could be exceeded.

The principal motivation behind this work was then to create sufficiently long plasmas of densities less than and greater than  $n_c/4$  and to examine the time dependent behavior of the scattered light in the back and forward directions.

## 5.1. EXPERIMENTAL CONDITIONS

The experiments described in this chapter were also carried out on the Glass Development Laser (GDL) system at the National Laser Users' Facility at the University of Rochester. The experimental set-up is shown in Fig. 5.2. The targets used were  $600 \pm 100 \mu\text{m}$  thick, 3 mm diameter foam discs of various average densities with a maximum value of usually  $\leq 0.25n_c$ . We expected complete ionization of these targets since simulations showed a laser burn-through on the order of  $800 \mu\text{m}$  at the peak of the  $0.35 \mu\text{m}$  pulse for an average target density of  $0.5n_c$ . The average cell size was on the order of  $10 \mu\text{m}$  in diameter for a

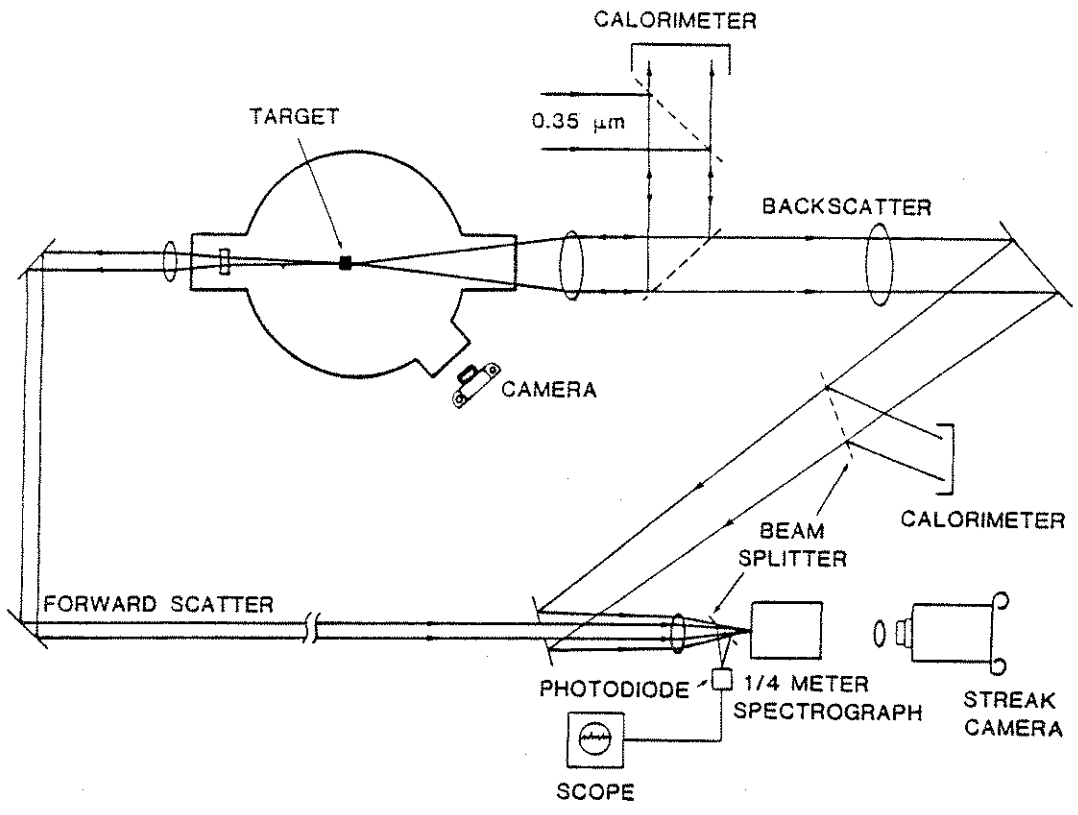


FIG. 5.2. Diagram of the experimental set-up. The forward optical path is 1.2 ns longer than the backward path.

target with a density of  $6.92 \times 10^{-3}$  gr/cm<sup>3</sup>, or an electron density of  $0.25n_c$ . Preliminary experiments on Raman scattering and more recent experiments on Brillouin scattering from such targets have been reported in the literature<sup>29,98</sup>. The average density of the foam targets used in these experiments was varied by altering the dextran (C<sub>6</sub>H<sub>10</sub>O<sub>5</sub>) concentration in the aqueous solution during the foam making process<sup>99</sup>. These targets were irradiated by a tightly focused 0.35 micron, 850 ps (FWHM) laser pulse with an average intensity of  $1.5 \times 10^{15}$  W/cm<sup>2</sup>. Both back and forward scattered light were spectrally and temporally resolved by using a 1/4 meter, 30 Å resolution optical spectrograph and a Hamamatsu C979 streak camera with a resolution of 30 ps. A calibrated Gen-Tec ED200 calorimeter with filters to absorb radiation near 0.35 μm was used to measure the total Raman backscattered energy. The laser burnthrough, as predicted by simulations<sup>29</sup>, was verified by time resolving the transmitted portion of the green line (0.53 μm) contained in the main 0.35 μm beam. This assured us that the entire thickness of the foam target had been ionized with a peak plasma density less than  $0.44n_c$  (which is the critical density for the 0.53 μm probe beam), thereby creating plasma lengths larger than 600 μm during the laser pulse.

That the foam target plasmas were hundreds of microns long was confirmed independently by imaging the Raman sidescattered light in the wavelength range 520 - 620 nm. For targets with an average density of less than  $n_c/4$ , these images showed emission from plasmas that were typically 300 μm long. A second calorimeter was used to measure the reflected energy of the 0.35 μm line.

## 5.2. RESULTS AND DISCUSSION

Both forward and backward spectra were obtained simultaneously from foam targets designed to produce plasmas with average densities between  $0.11n_c$  and  $0.25n_c$ . The optical path of the forward scattered spectrum was physically delayed by 1.2 ns with respect to the backscattered spectrum so that the two were clearly resolved by the streak camera. Interestingly, irrespective of the target density the backscattered spectrum from all these targets had the strongest emission in a narrow band of wavelengths between 470 nm and 500 nm, corresponding to densities of  $0.05n_c$  and  $0.07n_c$  (assuming a plasma temperature of 1 keV) as shown in Fig. 5.3. The spectrum shown in this figure was attenuated by  $10^6$  and only this band of wavelengths survived such strong attenuation. Up to 0.3% (150 mJ) of the incident energy was Raman backscattered in the solid angle subtended by the focusing lens (i.e.,  $5 \times 10^{-3}$  Sr). This rather large level of SRS-B rules out the possibility of the spectrum being due to collective Thomson scattering of the incident laser beam from the enhanced noise fluctuations in the plasma.

In order to observe the behavior of the less intense regions of the spectrum, an arrangement of neutral density and cut-off filters was necessary to be able to reduce the scattered intensity around 500 nm (where the emission was the most intense) to levels comparable with those at other wavelengths. An example of one such spectrum from a target with an average density of  $0.22n_c$  is shown in Fig. 5.4(a). Here, the short wavelength cut-off corresponds to the limiting case of scattering from zero density for a plasma temperature of 1 keV. The apparent gap in the spectrum between 520 nm and 585 nm is not real; it is due to the filters (Kodak wratten no. 25) used to suppress the very intense emission in this region. Unlike in Fig. 5.1, we can see now the emission extending right up to

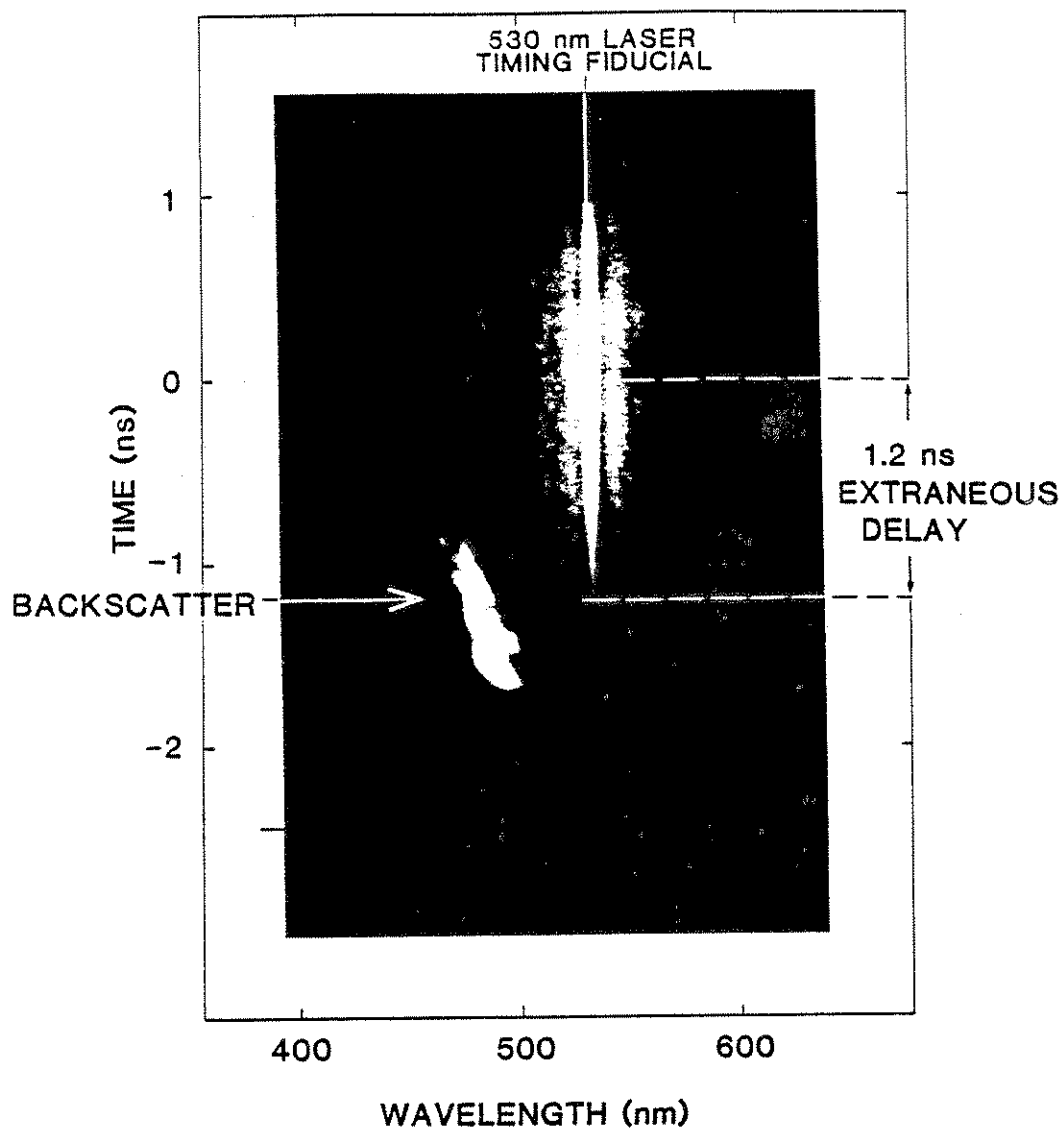


FIG. 5.3. Backward spectrum from a  $0.22n_c$  foam target. The spectrum was attenuated  $10^6$  times.

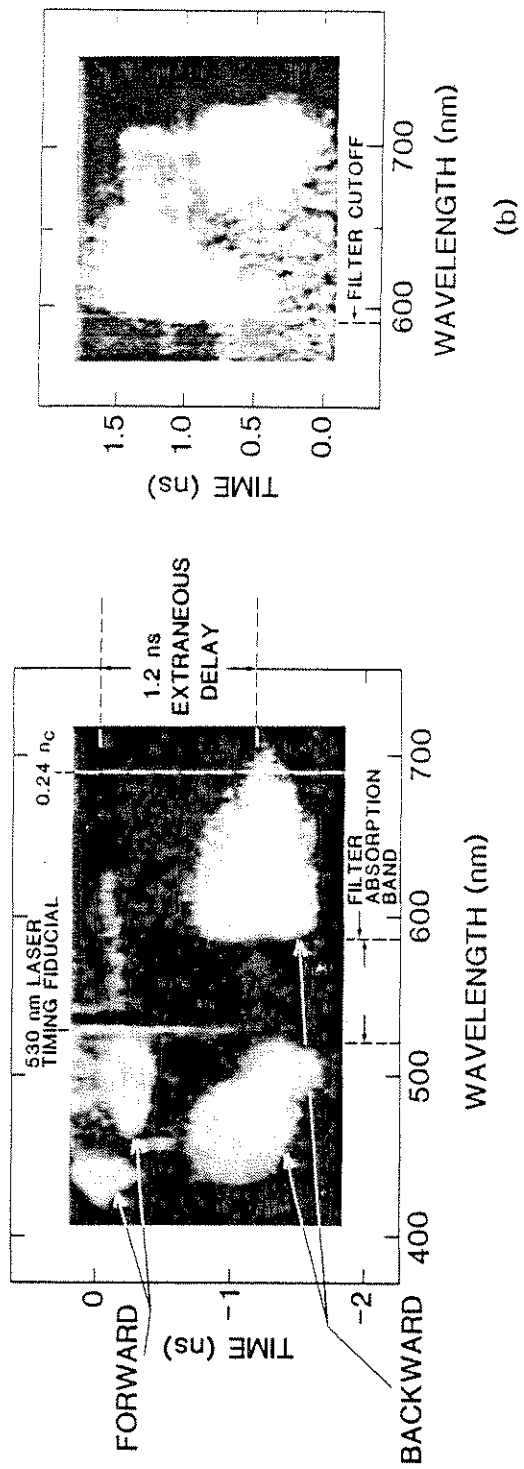


FIG. 5.4. Time resolved spectrum from two types of targets. (a) Forward (above) and backward (below) spectra from a 0.22 $n_c$  target. The lack of radiation between 520 and 585 nm in the backward spectrum is due to a Kodak Wratten filter # 25 used to attenuate the radiation below 600 nm. (b) Backscatter spectrum from a 0.25 $n_c$  target. The Raman gap can be observed between 630 and 700 nm.



700 nm or  $0.25n_c$ . In fact, these targets gave long wavelength cut-offs corresponding to densities between  $0.22n_c$  and  $0.24n_c$ . No detectable half-harmonic emission was observed with these targets. The detection threshold being  $> 10^{-6}\text{J/A/Sr}$ . When a target with an average density of  $0.25n_c$  was used, we readily observed the half harmonic emission for the first time.

A typical streak record of the details of the Raman emission for this kind of target in the vicinity of  $n_c/4$  is shown in Fig. 5.4(b). The half harmonic radiation at 700 nm on the right hand side is seen to appear first, indicating the presence of the quarter critical layer. The typical splitting of the half harmonic radiation is not readily resolved in this picture due to overexposure of the film. Sub quarter critical radiation follows about 250 ps later, but it does not extend continuously up to the half harmonic region in contrast to Fig. 5.4(a). Instead, a very distinct gap between 620 nm and 700 nm is seen, lasting only while the strong half harmonic emission is present. This gap, caused by reduction of the scattered signal by a factor of 10-20 compared to the signal obtained with a  $0.22n_c$  target, closes within 100 ps as soon as the strong half harmonic radiation is over. It is conjectured that the strong half harmonic emission is indicative of the bulk plasma being able to support the  $n_c/4$  layer, whereas the weak part which follows is probably due to localized residues of the quarter critical density.

Fig. 5.5 shows the time integrated backscattered intensity vs. the corresponding wavelength for the  $0.22n_c$  and the  $0.25n_c$  foam targets. The plot is a composition of several shots taken with different levels of attenuation which sampled the scattered spectrum in a topographic manner. For both types of targets the overall behavior of the backscattered spectrum is very similar. It peaks around 500 nm and then drops off on both the long and short wavelength sides

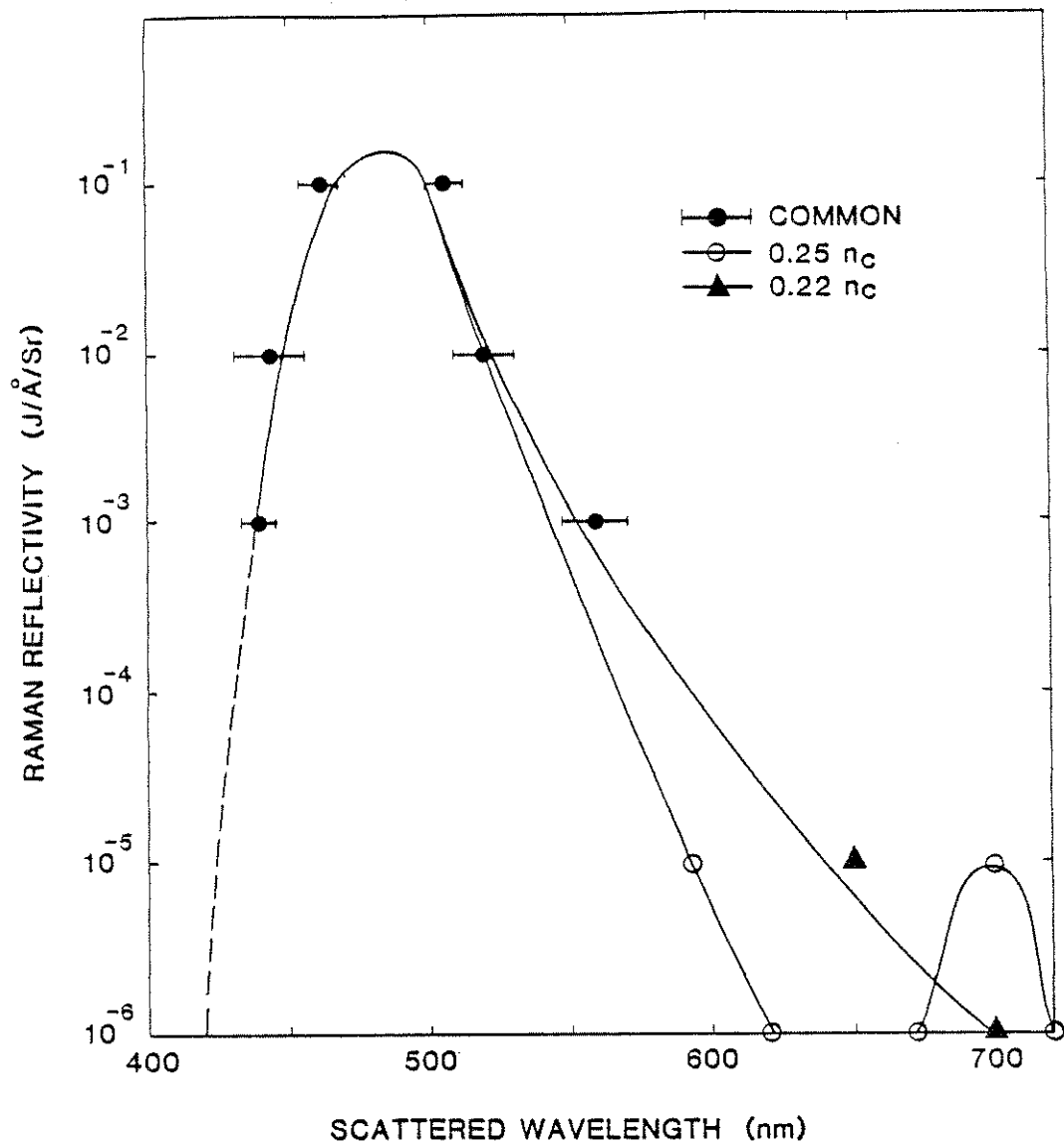


FIG. 5.5. Time integrated backscatter spectrum from a  $0.22n_c$  and a  $0.25n_c$  target.

very rapidly. The difference between the two spectra becomes noticeable in the region near 600 nm. In this region, the spectrum from the  $0.25n_c$  target drops faster than the one from the  $0.22n_c$  target, reaching the detection threshold near 625 nm and rising above threshold again about 700 nm. There is a difference of only a factor of 10 in intensity between the two spectra at 600 nm, for instance (the  $0.25n_c$  spectrum being less intense). Since this reduction is concurrent with the appearance of the half-harmonic radiation, one is led to speculate that the process causing the half harmonic is in some way responsible for further quenching the Raman instability below  $n_c/4$ , although even in the absence of the half harmonic radiation the Raman emission peaks at  $0.06n_c$  and falls off rapidly at higher densities. In our experiments, however, if the half harmonic is regarded as the signature for the  $2\omega_p$  instability, then it is clear that this instability cannot entirely account for the reduced Raman levels at densities close to  $n_c/4$ . Also, as Fig. 5.4(a) indicates, the Raman spectrum extends continuously up to 700 nm but the level of scattering between 600 nm to 700 nm is on the average  $10^4$  times weaker than that at the peak. The plasma is acting as a narrow band source. Such a strong suppression of Raman cannot be attributed to either the opacity or the influence of localized regions of  $n_c/4$  which may be present. These results indicate that the quenching of the SRS-B instability in density regions near  $n_c/4$  may be due to other processes that are quite independent of the presence of the  $n_c/4$  layer. Further studies are underway to resolve this issue.

When foam targets with average density of  $0.5n_c$  were used, the SRS-B reflectivity dramatically decreased to  $10^{-4}$  of the incident energy. As reported earlier<sup>27</sup>, this is still a factor 10-30 greater than that obtained with foil targets. Since the average density is greater than  $n_c/4$ , Raman presumably cannot occur

in the bulk of the plasma but occurs either locally or in the front blow off plasma.

Fig. 5.6 shows the reflectivity of the 0.35 micron line vs. the average foam density used. The width of the band indicates shot to shot variation. It has been shown recently that the backscattered light near the 0.35 micron line is due to Brillouin scattering (SBS)<sup>98</sup>. The backscattered levels tend to increase as the target density increases, reaching a maximum level of  $9\pm 2\%$  for target densities of  $0.20n_c$ . Such a high level of SBS can influence the Raman instability since now SRS has to occur in a rippled density profile.

Now we discuss the forward scattered spectrum. This spectrum was obtained from targets with average densities between  $0.11n_c$  to  $0.22n_c$ . A typical example of such a spectrum is shown in Fig. 5.7 for a target with an average density of  $0.22n_c$ . The vertical line at 530 nm is the trace green line contained in the 0.35 micron main laser pulse. It serves as a fiducial line for both spectral and temporal calibration. The forward spectrum typically extends over a wide range of wavelengths from about 420 nm to 620 nm, it is polarized in the same direction as the incident beam, and it is about  $10^4$  times weaker than the backscattered spectrum. Typically, forward scatter was observed at the peak of the laser pulse and lasted for about 100-150 ps, whereas the backscatter occurred throughout the laser pulse. Also, a 20% decrease in laser energy quenched the forward scatter, indicating that this spectrum is probably the result of a non-linear process excited near threshold.

One feature common to forward and backscatter was the wavelength range over which the two spectra occurred. The scattered spectrum from the SRS-F instability might be expected to be extended to lower densities or shorter

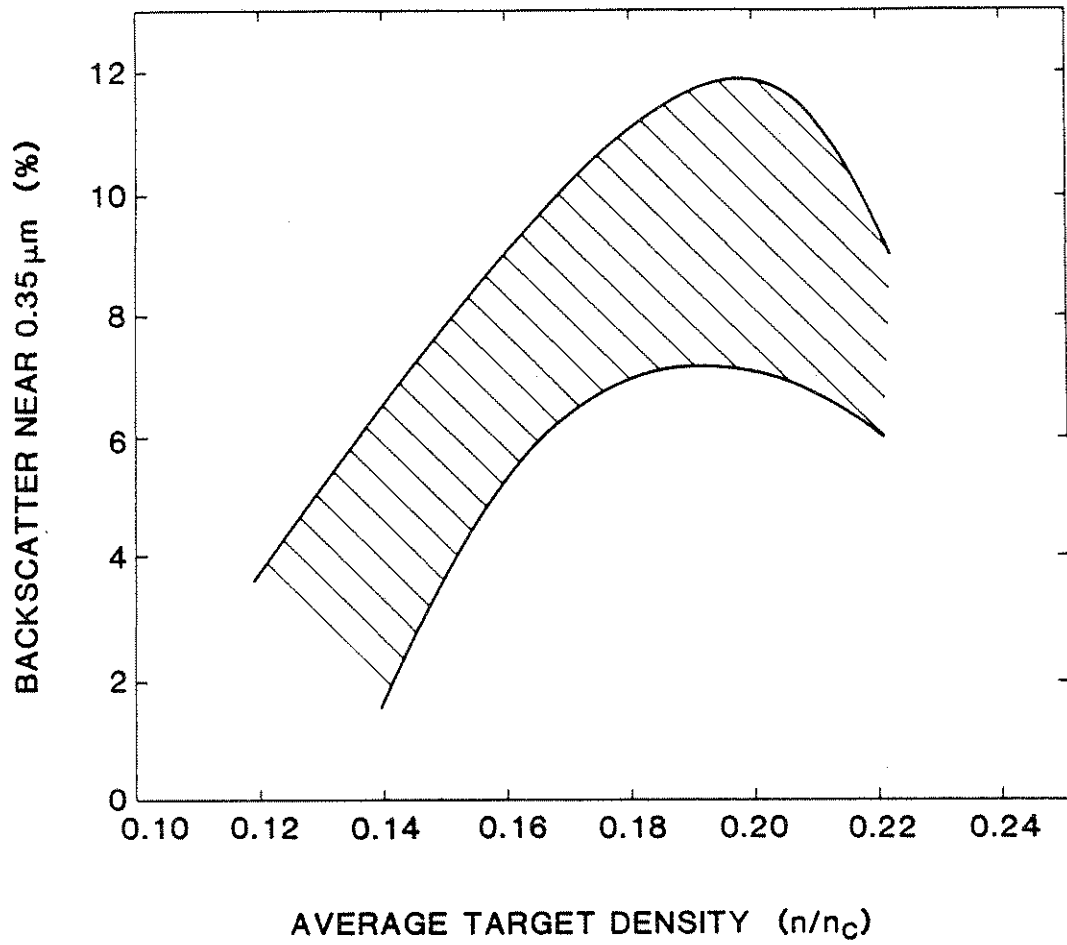


FIG. 5.6. SBS reflectivity vs. target density. The width of the band corresponding to shot-to-shot variation in the scattered intensity.

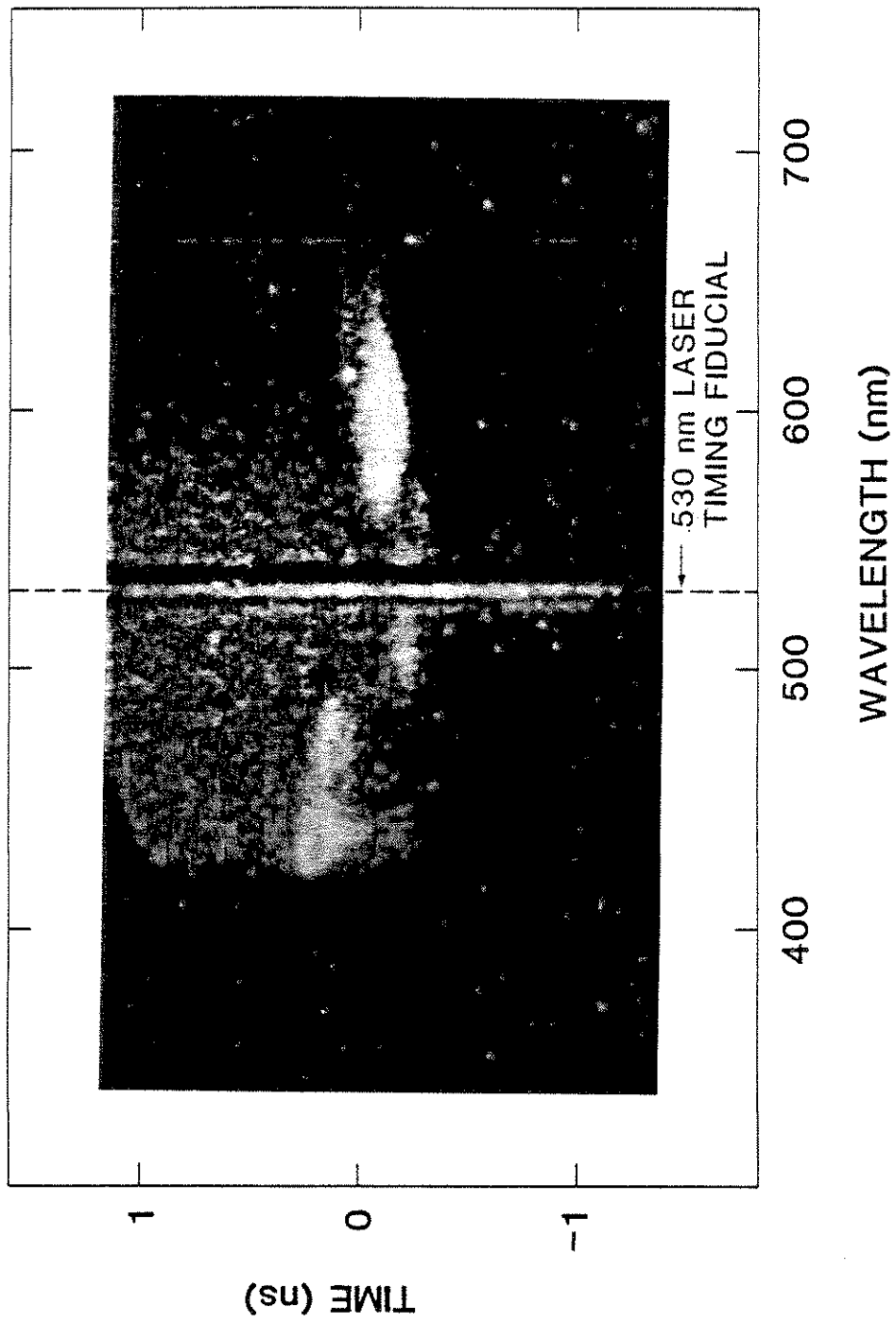


FIG. 5.7. Time resolved forward scattered spectrum from a  $0.22n_c$  target.

wavelengths compared to the SRS-B spectrum, since the high phase velocity plasma waves characteristic of SRS-F have little Landau damping . However, as can be seen from Fig. 2.4, the threshold intensity for SRS-F at  $0.1n_c$  is already  $3.5 \times 10^{16}$  W/cm<sup>2</sup> and increases to  $10^{17}$  W/cm<sup>2</sup> at  $0.05n_c$  for a plasma scalelength of 600  $\mu$ m. Of course, for plasma lengths of 600  $\mu$ m and a linear profile, the local density scalelengths are shorter than 600  $\mu$ m, and therefore, the threshold intensities at a given density will be even higher than the ones estimated above. Since the average laser intensity in these experiments was on the order of  $10^{15}$  W/cm<sup>2</sup>, the plasma had to have either a much longer scalelength to exceed the threshold for SRS-F, or the instability was being generated locally in regions where the laser intensity was much higher (possible hot spots or filaments) or the forward scatter was not growing from noise. The coincidence of the spectral range for the forward and backward spectra suggest this last possibility, that the forward scatter is not growing from noise, but that it is possibly being seeded by SRS-B. There are two ways in which this coupling can take place. First, the plasma waves created at low densities by SRS-B can move up the density gradient until the plasma wave vector becomes short enough to support scattering in the forward direction. This possibility was first considered by Koch and Williams<sup>100</sup>.

Assume that a plasma wave with frequency  $\omega_{epw}$  has been excited by SRS-B at a density  $n_b/n_c$  (the subscript b stands for backscatter) in the front side of the target. This wave will move to regions of higher densities until reaching a density where the  $\omega$  and  $k$  matching conditions for the excitation of SRS-F will be satisfied. At this point, the relations defining this instability will be:

$$\omega_{\text{epw}}^2 = \omega_p^2 + 3k_p^2 v_e^2 \quad (5.1)$$

where

$$k_p = k_o - k_s \quad (5.2)$$

is the k matching condition for 1-D SRS-F and

$$k_o = \frac{[\omega_o^2 - \omega_p^2]^{1/2}}{c} \quad (5.3a)$$

$$k_s = \frac{1}{c} [(\omega_o - \omega_{\text{epw}})^2 - \omega_p^2]^{1/2} \quad (5.3b)$$

Substituting relations (5.3) and (5.2) into relation (5.1) one gets the following expression for the density  $n_f/n_c$  at which SRS-F is being excited as a function of the frequency  $\omega_{\text{epw}}$  of the plasma wave excited by SRS-B:

$$\begin{aligned} & 6 \left[ \frac{v_e}{c} \right]^2 \left[ \left( 1 - \frac{n_f}{n_c} \right) \left[ \left( 1 - \frac{\omega_{\text{epw}}}{\omega_o} \right)^2 - \frac{n_f}{n_c} \right] \right]^{1/2} + \left[ \frac{\omega_{\text{epw}}}{\omega_o} \right]^2 - \\ & - 3 \left[ \frac{v_e}{c} \right]^2 \left[ 1 + \left( 1 - \frac{\omega_{\text{epw}}}{\omega_o} \right)^2 \right] - \left[ 1 - 6 \left( \frac{v_e}{c} \right)^2 \right] \frac{n_f}{n_c} = 0 \end{aligned} \quad (5.4)$$

Now,  $\omega_{\text{epw}}$  can be related to the density  $n_b/n_c$  where it was excited through the  $\omega$  and k conditions for SRS-B. Thus, equation (5.4) relates the original density  $n_b/n_c$  to the density  $n_f/n_c$  where this wave could seed forward scatter. This relationship is plotted in Fig. 5.8(a). Here we have assumed a temperature of 1 keV.



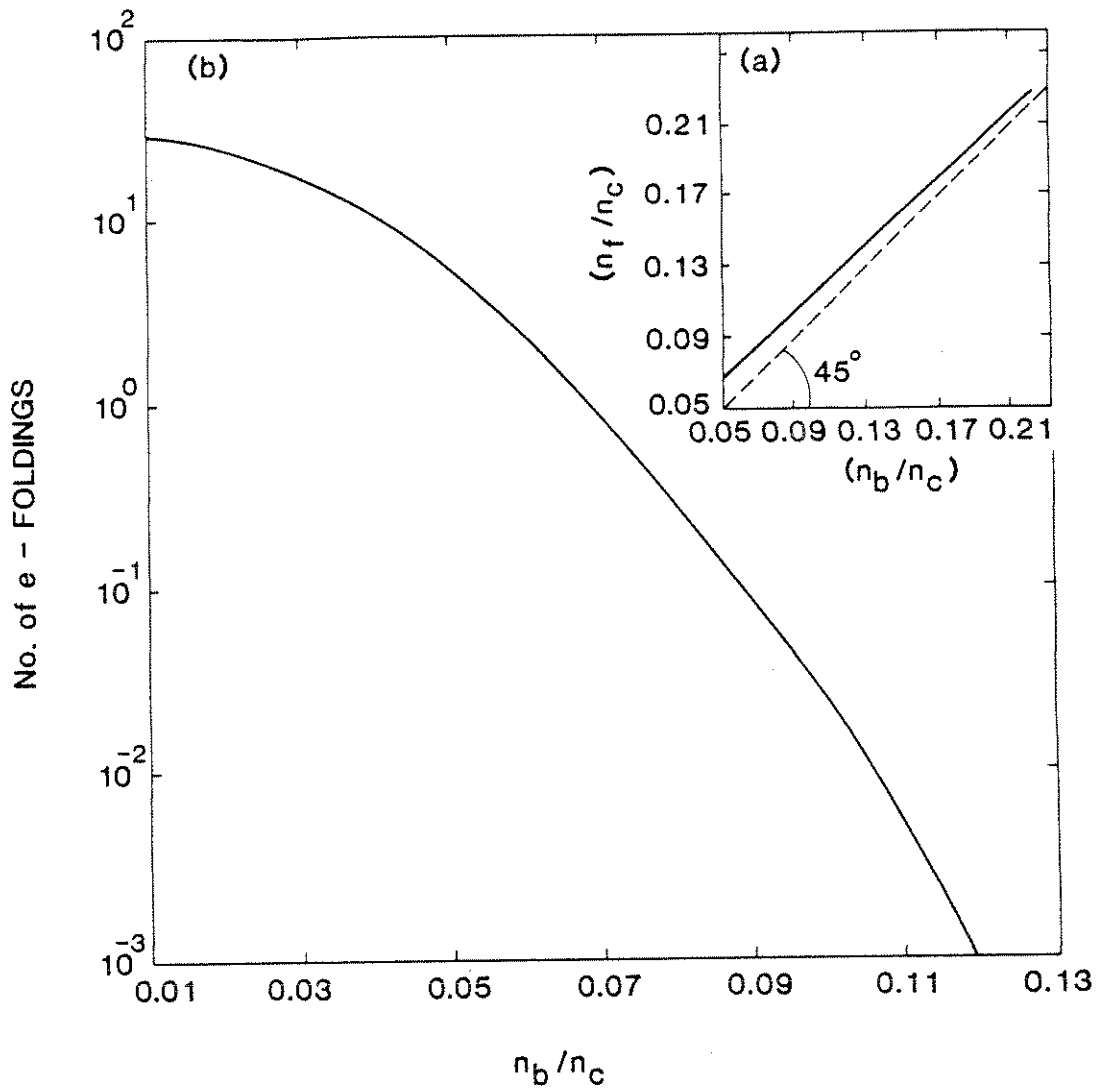


FIG. 5.8. SRS-F excitation from SRS-B in an inhomogeneous plasma. (a) Relationship between the density  $n_b/n_c$  where the plasma wave was originally excited by SRS-B and the density  $n_f/n_c$  where the wave has to travel to excite SRS-F. The dashed bisector is shown for reference. (b) Number of e-foldings that the plasma wave decays through Landau damping in going from  $n_b/n_c$  to  $n_f/n_c$ .

If the plasma were a non-dissipative medium the plasma wave would travel from  $n_b/n_c$  to  $n_f/n_c$  with a slight reduction in the amplitude of the density perturbation associated with it. This can easily be seen if one substitutes the dispersion relation of the plasma wave and Poisson's Eqn. into the relation for the conservation of the energy flux. However, because of the interaction of this wave with the plasma particles, the plasma waves generated at low densities will show a strong damping as they move to their corresponding  $n_f/n_c$ . If we assume a plasma with a length  $L$  and a linear density profile of the form  $n = n_p x/L$  ( $n_p$  is the peak plasma density) we can estimate the number of e-foldings  $\alpha$  that the wave will decay in going from  $n_b/n_c$  to  $n_f/n_c$ . In this case,  $\alpha$  will be given by  $\alpha = \int k_L dx$  where  $k_L$  is the spatial Landau damping given by  $k_L = (1/2\pi)\omega_L/v_g$ ,  $\omega_L$  is the temporal Landau damping and  $v_g$  is the group velocity of the plasma wave. Fig. 5.8(b) shows the number of e-foldings vs. the original density  $n_b/n_c$ . Only those plasma waves generated at densities higher than  $0.07n_c$  will have chance of reaching the necessary density layer to excite SRS-F. Waves generated below  $0.05n_c$  will be heavily Landau damped. This means that the forward scattered spectrum will have a short wavelength cutoff around 490 nm. We see, however, that the forward spectrum extends to regions of shorter wavelength. This indicates that it is unlikely that this process is solely responsible for the presence of the forward scattered spectrum.

The other possibility for the observed forward scatter is through the coupling of SRS-B with SBS. This coupling occurs between the large  $k$  plasma wave of SRS-B and the ion acoustic wave of SBS with wave vector  $k_i$ . As we saw in chapter III, the result of this coupling is the generation of plasma wave modes with wave vectors  $k_p \pm nk_i$  and frequency  $\omega_{epw} \pm n\omega_{ac} \approx \omega_{epw}$ . The

small  $k$  mode with wave vector  $k_p - k_{ac}$  will propagate in the opposite direction to the incident laser beam since  $k_i > k_p$ . For reasons of clarity, the effects of this coupling has been represented once more in Figs. 5.9(a) and 5.9(b). The solid curve in Fig. 5.9(a) represents the dispersion relation of a plasma wave in the absence of a ripple in terms of normalized dimensions. These normalized dimensions have been chosen in order to ease the comparison with the case when there is a ripple present. If one assumes that the density ripple is produced by the presence of SBS, then  $k_i = 2k_o$  and the plasma wave from SRS-B will be located in the region limited by the points (1) and (2). The exact location of the plasma wave in this region will depend on the plasma density. The point (1) corresponds to zero density ( $k_p = 2k_o$  or  $q = 2$ ), and the point (2) corresponds to the quarter critical density ( $k_p = k_o$  or  $q = 1$ ). In the presence of a ripple, the spatial harmonics interact among themselves, creating forbidden frequency bands as was explained in chapter III. The interaction between these modes is plotted in Fig 5.9(b).

A plasma wave with normalized wave vector  $q_o$  excited by SRS-B, will interact with the density ripple created by SBS to generate a large wave vector plasma wave  $q_1$  and a small wave vector plasma wave  $q_2$  which propagates in the opposite direction to the incident laser beam. If this small  $k$  vector is excited in the front half side of the plasma, as shown in Fig. 5.10, then it will propagate to lower densities until reaching a turning point. Notice from Fig. 5.9(b) that for the spatial modes with small wave vectors  $q_2$ , their wave vector decreases as the mode moves to lower densities. This is in contrast to the usual case where the wave vector of a plasma wave increases as the density decreases.

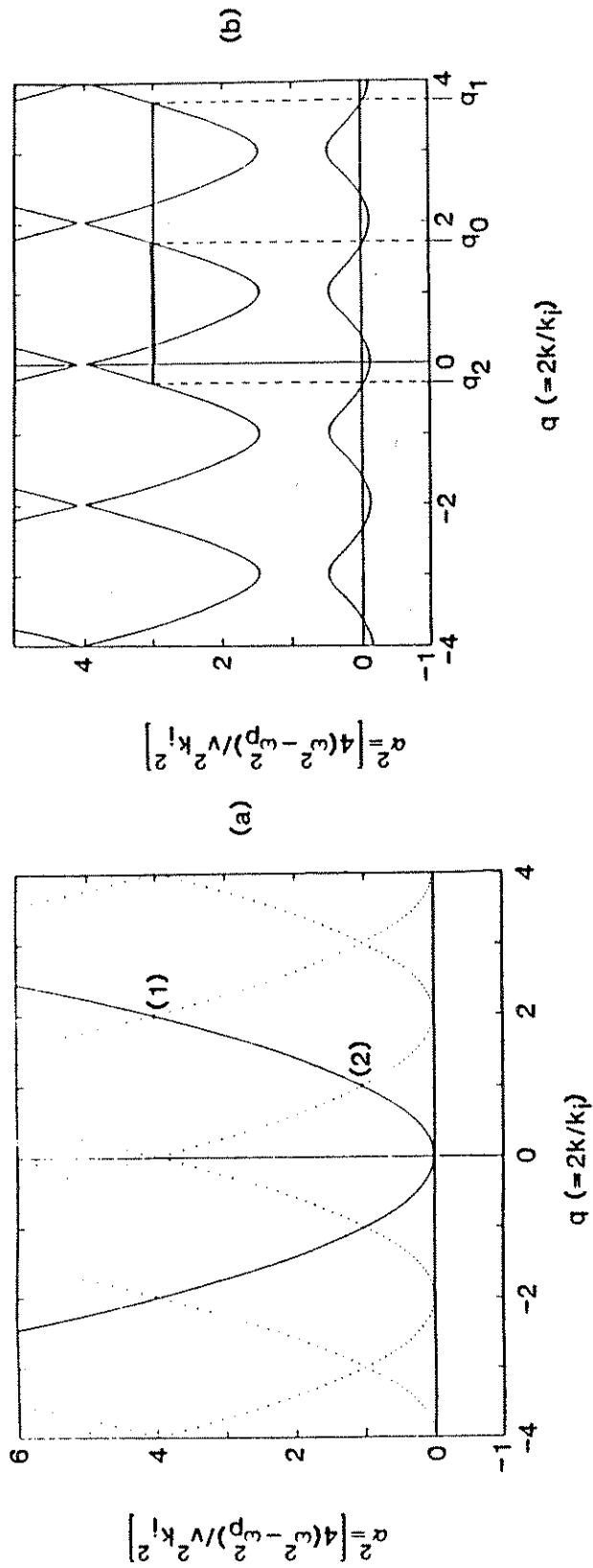


FIG. 5.9. Dispersion relation of a plasma wave. (a) The solid curve represents the dispersion relation of a plasma wave in the absence of a ripple. The dotted curves represent the dispersion relation of the spatial harmonics that the plasma wave would display in the presence of a ripple with wave number  $k_j$ . (b) Dispersion relation of the plasma wave in the presence of (b) Dispersion relation of the plasma wave in the presence of a ripple.  $q_0$  represents the wave number of a plasma wave excited by SRS-B;  $q_1$  and  $q_2$  represent the wave numbers of the first harmonics of the primary mode  $q_0$ .

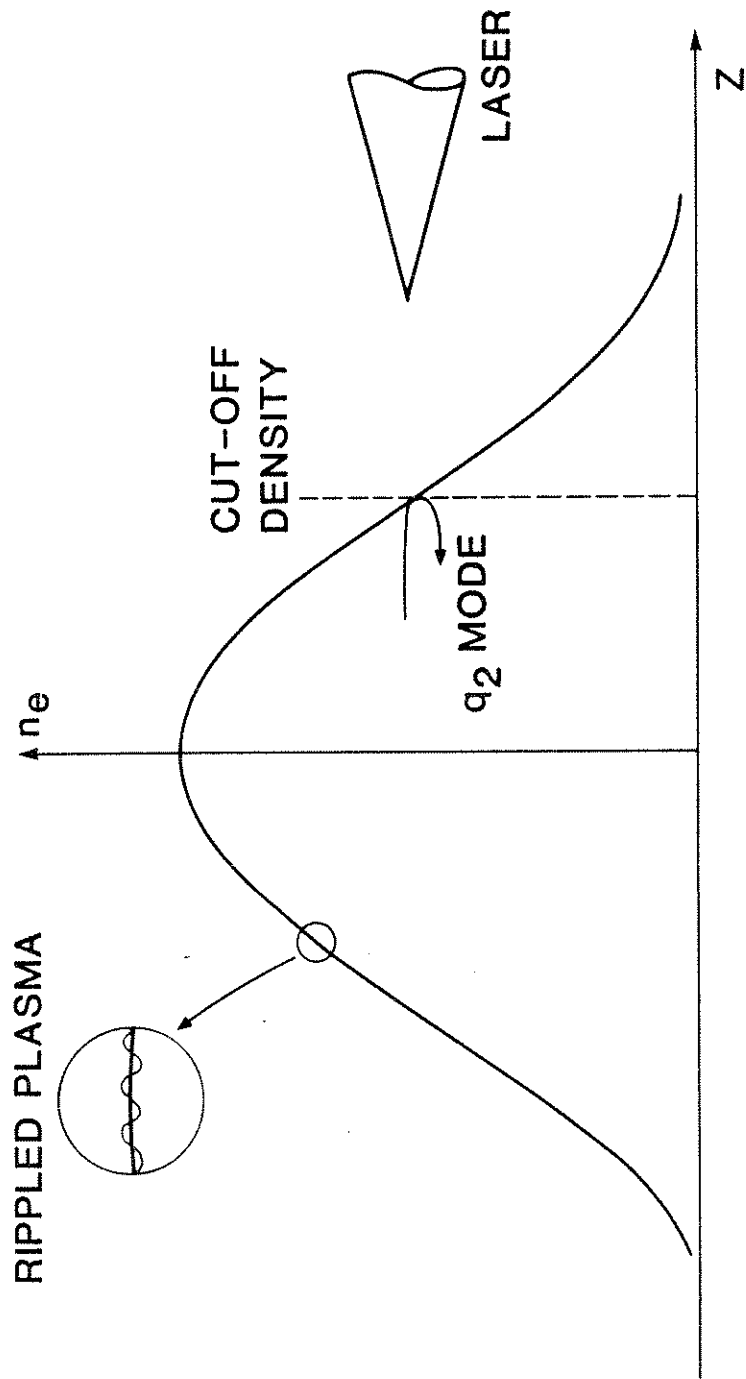


FIG. 5.10. Sketch of the behavior of the small wave vector mode  $q_2$  as it moves parallel to the density gradient. A cut-off layer for this mode is found as the wave moves to lower densities.

Once the small  $k$  wave has been reflected to the forward direction, it will pass through the original density layer where it was generated, becoming a source of scatter in the forward direction. The result is that a particular density layer could scatter light at the same frequency in both the forward and the backward directions. This situation is in contrast to the case where SRS-F and SRS-B are excited independently. In this case, the scattering in the backward direction is red shifted with respect to the scattering in the forward direction due to the fact that the plasma wave from SRS-B has a larger wave vector than the plasma wave from SRS-F. Thus, in an inhomogeneous plasma, the presence of a rippled density will make possible the scattering in both the forward and backward direction in the same range of frequencies. This type of behavior was observed in these experiments as shown in Fig. 5.4(a). Thus, it is possible that the observed forward scattered spectrum is not being excited from noise but from the beating of the large  $k$  plasma wave from SRS-B with the ion acoustic wave from SBS.

The main findings of these experiments with foam targets are following:

- 1- For targets with average density less than  $0.25n_c$  up to 0.3% of the incident energy is backscattered within a solid angle of  $5 \times 10^{-3}$  sr. These high reflectivities suggest that Raman scattering is operative in these long foam target plasmas rather than just enhanced Thomson scattering of the laser light.

- 2- When the foam density is increased to  $0.5n_c$  the reflected Raman light drops to about  $10^{-4}$  of the incident since the instability can no longer occur in the bulk of the plasma.

- 3- When targets with an average density less than  $0.22n_c$  are used, no detectable half-harmonic emission is observed. In such targets, most of the Raman

emission occurs in a range of frequencies between 470 nm and 500 nm.

4- When targets with average density slightly higher than  $n_c/4$  are used, the half-harmonic radiation is detected for the first time. Concurrent with this, the Raman emission between 600 nm and 700 nm is further reduced by a factor of 10-20. When the half-harmonic ceases there is an abrupt increase of the scattered signal by the same factor in this range of frequencies near 700 nm. The peak emission still comes from around 500 nm.

5- Weak, broad-band forward scatter is observed only when targets with average density less than  $n_c/4$  are used. This emission occurs around the peak of the laser pulse and lasts for  $< 150$  ps.

6- The forward scattered spectrum covers the same range of frequencies as the backscattered spectrum and disappears with a 20% reduction of the laser intensity. It is suggested the possibility that the forward emission is being seeded by SRS-B. The most likely way in which this excitation can occur is through the coupling of the plasma wave from SRS-B with the ion acoustic wave from SBS.

## CHAPTER VI

### HALF HARMONIC SPLITTING

Although the splitting of the half harmonic radiation emanating from the  $n_c/4$  layer into a red- and a blue-shifted satellite has been consistently reported by several groups<sup>101-104</sup>, it is not clear yet what mechanism is the source of such splitting<sup>105</sup>. We have carried out theoretical and experimental studies in this respect, and it is the purpose of this chapter to report our findings. Here, we study several mechanisms capable of splitting the half-harmonic light and analyze the extent to which they can be responsible for the splitting observed in our experiments.

#### 6.1 SPLITTING DUE TO SELF-GENERATED MAGNETIC FIELD

The first of these mechanisms is the presence of a d.c magnetic field perpendicular to the laser path. This magnetic field can be generated by the flux of energetic electrons ejected from the plasma<sup>106</sup> (fountain effect) or by the  $\nabla n \times \nabla T$ <sup>107</sup> mechanism.

Let the pump wave be  $\mathbf{E} = e_o \cos(k_o x - \omega t)$ . The self-generated magnetic field  $\mathbf{B}_o$  perpendicular to  $\mathbf{k}_o$  will in general have both y and z components. The dominant polarization of the backscattered e.m. wave will be the same as the incident beam. Therefore, its electric field  $\mathbf{E}_s$  will make an angle with respect to  $\mathbf{B}_o$  and both ordinary and extraordinary modes will be able to propagate simultaneously. Thus, two SRS-B processes are possible:



$$(\omega_o, \mathbf{k}_o) \rightarrow (\omega_{epw}, \mathbf{k}_p) + (\omega_{se}, \mathbf{k}_{se}), \quad (6.1a)$$

$$(\omega_o, \mathbf{k}_o) \rightarrow (\omega_{epw}, \mathbf{k}_p) + (\omega_{so}, \mathbf{k}_{so}). \quad (6.1b)$$

Here  $(\omega_{se}, \mathbf{k}_{se})$  and  $(\omega_{so}, \mathbf{k}_{so})$  represent the scattered extraordinary and ordinary e.m. waves, respectively, satisfying the dispersion relation<sup>108</sup>

$$\frac{c^2 k_{se}^2}{\omega_{se}^2} = 1 - \frac{\omega_p^2}{\omega_{se}^2} \frac{\omega_{se}^2 - \omega_p^2}{\omega_{se}^2 - \omega_h^2} \quad (6.2a)$$

$$\omega_{so}^2 = \omega_p^2 + c^2 k_{so}^2 \quad (6.2b)$$

The electron plasma wave  $(\omega_{epw}, \mathbf{k}_p)$  is at the upper-hybrid frequency

$$\omega_{epw} \approx \omega_h = (\omega_p^2 + \omega_c^2)^{1/2},$$

where  $\omega_c = eB/mc$  is the cyclotron frequency. The Raman process involving the ordinary wave does not give anything new. The minimum scattered frequency is  $\approx \omega_o/2$ , if  $\omega_c \ll \omega_p$ , as is usually the case. On the other hand, frequency matching with the extraordinary wave gives

$$\omega_o = \omega_{se} + (\omega_p^2 + \omega_c^2)^{1/2}. \quad (6.3)$$

The minimum frequency at which the instability occurs will be that at which

$k_{se} = 0$ , or

$$\omega_{se} = \omega_R = \frac{1}{2}[\omega_c + (\omega_c^2 + 4\omega_p^2)^{1/2}] \quad (6.4)$$

and for  $\omega_c \ll \omega_p$  this occurs at a plasma density of

$$\omega_p^2 = \frac{\omega_o^2}{4} \left(1 - \frac{\omega_c}{\omega_o}\right) \quad (6.5)$$

or

$$\frac{n_{\max}}{n_c} = \frac{1}{4} (1 - 9.34 \times 10^{-9} B_o \lambda_o) \quad (6.6)$$

where  $B_o$  is expressed in gauss and  $\lambda_o$  in  $\mu\text{m}$ . The minimum scattered frequency is thus

$$\omega_{se} \approx \omega_o/2 + \omega_c/4, \quad (6.7)$$

and the Raman backscattered light involving the extraordinary wave is blue-shifted by an amount which is

$$\Delta\lambda_s(\text{A}^\circ) = 1.15 \times 10^{-5} B_o \text{ (G)}. \quad (6.8)$$

In a warm plasma, the scattered frequencies  $\omega_{se}$  and  $\omega_{so}$  are both red-shifted by an amount which is<sup>14,35</sup>

$$\frac{9}{8} \left[ \frac{v_e}{c} \right]^2 \omega_o = \frac{9}{8} \frac{T_e(\text{keV})}{511} \omega_o, \quad (6.9)$$

thus not introducing any relative shift. This result (eqn 6.8) is the same as that obtained by Barr et al.<sup>36</sup> who verified this model using 1D particle simulations.

## 6.2 SPLITTING FROM $2\omega_p$ DECAY

A second process which might lead to splitting of the half-harmonic signal is the mode conversion of the two-plasmon decay waves into e.m. waves<sup>110</sup>. In the cold plasma approximation an e.m. wave with frequency  $\omega_o$  can decay into two plasma waves, each with frequency  $\omega_o/2$  at  $n_c/4$ . However, when thermal corrections are included the plasmon frequencies can show a significant red and blue shift. Furthermore, if both plasmons are mode converted into e.m. waves, then a symmetric splitting around  $\omega_o/2$  will be observed. This splitting can be as strong as the Raman red shift caused by finite temperature effects.

Let  $(\omega_{epw1}, \mathbf{k}_1)$  and  $(\omega_{epw}, \mathbf{k}_2)$  be the two plasma waves. Taking  $\omega_p = \omega_o/2 - \delta$ , the frequency matching condition gives

$$\omega_o = [(\omega_o/2 - \delta)^2 + 3k_1^2 v_e^2]^{1/2} + [(\omega_o/2 - \delta)^2 + 3k_2^2 v_e^2]^{1/2}. \quad (6.10)$$

Assuming  $\delta \ll \omega_o/2$ , we obtain after expanding,

$$\delta = \frac{3}{2} \frac{v_e^2}{c} \frac{(k_1^2 + k_2^2)}{k_o} \quad (6.11)$$

where  $k_o$  is the laser wave number in vacuum. Substituting  $\delta$  into the dispersion relation of the plasma waves, we get

$$\omega_{\text{epw}1,2} = \frac{\omega_0}{2} \left[ 1 \pm \frac{3v_e^2}{c^2} \frac{(k_1^2 - k_2^2)}{k_0^2} \right] \quad (6.12)$$

The x and y components of the plasma wave vector, originated from the two-plasmon decay instability, are related for maximum growth rate in a homogeneous plasma by<sup>110</sup>

$$\frac{k_{1x,2x}}{k_0} = \frac{\sqrt{3}}{4} \pm \left[ \frac{k_y^2}{k_0^2} + \frac{3}{16} \right]^{1/2}. \quad (6.13)$$

Here,  $\mathbf{k}_0 = k_0 \hat{x}$ ,  $k_{1x,2x}$  and  $k_y$  are the x and y components of the plasma wave vectors as shown in Fig. 6.1. Notice that  $k_{1y} = -k_{2y} \equiv k_y$ . Using Eq. (6.13) we can write Eq. (6.12) as

$$\omega_{\text{epw}1,2} = \frac{\omega_0}{2} \left[ 1 \pm \frac{9}{8} \frac{v_e^2}{c^2} \left[ \left( 1 + \frac{32}{3} \frac{k_1^2}{k_0^2} \right)^{1/2} - 1 \right] \right] \quad (6.14)$$

which is no longer dependent on  $k_2$ .

On mode conversion, the scattered light spectrum will show broad red- and blue-shifted peaks with respect to  $\omega_0/2$ , with frequency shifts given by

$$\frac{\Delta\omega}{\omega_0} = \pm \frac{9}{16} \frac{v_e^2}{c^2} \left[ \left( 1 + \frac{32}{3} \frac{k_1^2}{k_0^2} \right)^{1/2} - 1 \right] \quad (6.15)$$

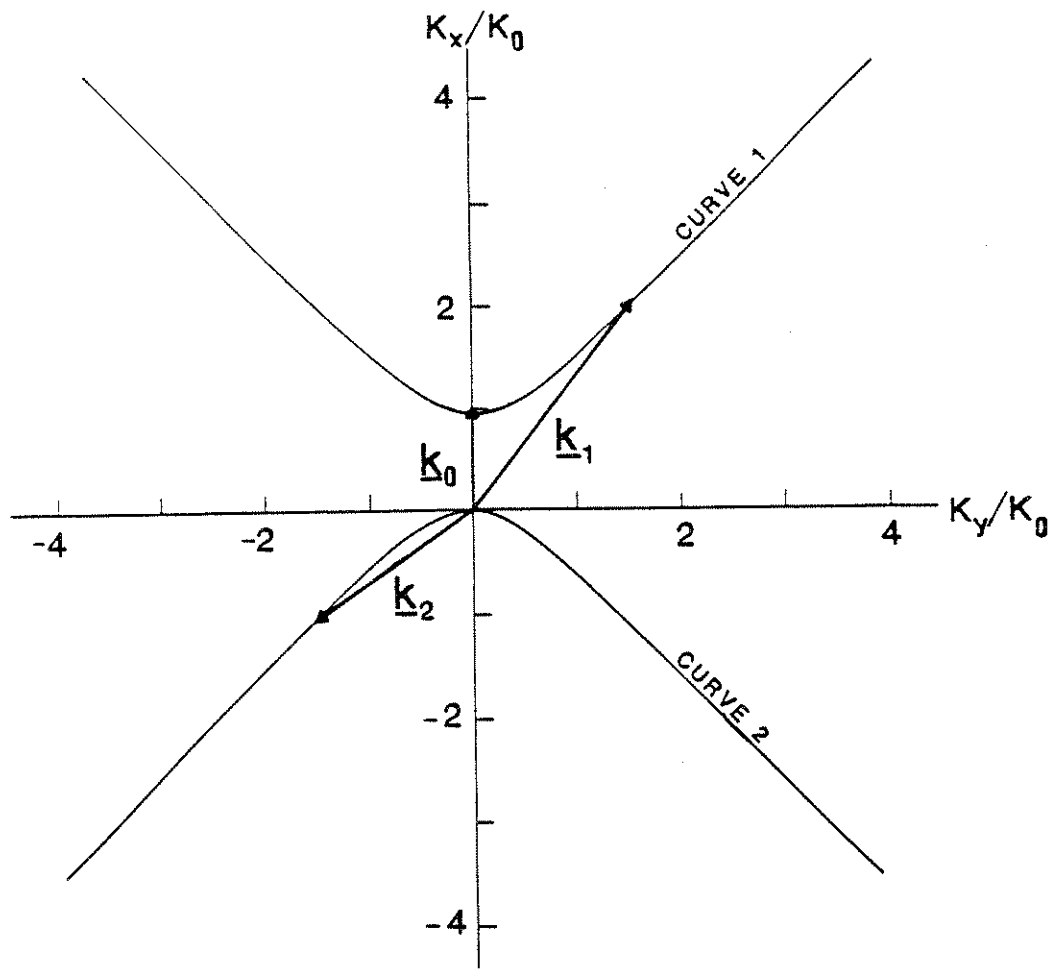


FIG. 6.1. Relationship between the x and y components of the plasmon wavevectors ( $k_1$  and  $k_2$ ) that give the maximum growth rate for the  $2\omega_p$  decay instability. Curve 1 relates  $k_{1x}$  to  $k_{1y}$ , and curve 2 relates  $k_{2x}$  to  $k_{2y}$ .

This frequency shift will be limited by Landau damping to approximately  $k_1\lambda_D < 0.6$ . Thus the allowed range of wavenumbers will be

$$\frac{\sqrt{3}}{2} < \frac{k_1}{k_0} < \frac{6.6}{T^{1/2}(\text{keV})}, \quad (6.16)$$

leading to a symmetric splitting in the range

$$\frac{T_e(\text{keV})}{227} < \frac{\Delta\lambda}{2\lambda_0} < \frac{T_e(\text{keV})}{511} \left[ \frac{21}{T^{1/2}(\text{keV})} - 1 \right] \quad (6.17)$$

Here,  $\lambda_0$  is the laser wavelength in vacuum.

This broadening of the blue- and red- shifted satellites around  $\frac{\omega_0}{2}$  is in contrast with the spectral shift due to thermal effects on Raman backscatter in which a red shifted sharp line should be observed. In these calculations the angular dependence of the conversion efficiency of the plasma waves into e.m. waves has not been considered.

### 6.3. SPLITTING DUE TO A DENSITY RIPPLE FROM SBS

A third mechanism we analyzed which is capable of splitting the half-harmonic light is the coupling of the plasma wave excited by SRS with the ion wave from Brillouin scattering.

Stimulated Brillouin scattering (SBS) is the decay of an intense e.m. wave into an ion acoustic wave and a scattered e.m. wave. This instability occurs in

the density region  $n \leq n_c$ . and has a threshold lower than SRS. Therefore, provided that the laser pulse is long enough, whenever SRS is excited it will occur in the presence of a rippled plasma due to SBS. SBS was present in all our experiments on both foil and foam targets when SRS was observed. Figure 6.2 represents the regions of occurrence of SRS-B in the presence of SBS. The  $\alpha^2$  axis is given by either of the relations (3.19) depending on whether we are referring to e.m. waves or plasma waves. A density ripple created by SBS will have a wave number  $k_1 \approx 2k_0$ , where  $k_0$  is the wave number of the incident e.m. wave (or pump). Therefore, the pump wave will always be represented by the point (0), since the value of  $q$  for the pump will be  $q = 2k_0/k_1 = 2k_0/2k_0 = 1$ . Near the quarter critical density the wave number of the scattered wave will tend to 0, whereas the wave number of the plasma wave will tend to  $k_0$ . These two waves are represented by the points (4) and (2), respectively. As the plasma density goes to zero, the wave number of the scattered wave will tend to  $-k_0$ , whereas the wave vector of the plasma wave will tend to  $2k_0$ . These waves are represented by points (3) and (1) respectively. As the plasma wave varies between these two values, the scattered wave will move between the points (3) and (4). As SBS is excited, the plasma waves will suffer a disruption of their dispersion relation near the  $n_c/4$  (point (2)) density layer, and also near zero density (point (1)). The dispersion relation of the scattered e.m. wave will only suffer a disruption near zero density (point (3)). Close to the quarter critical density ( $k_s \approx 0$ ) the frequency of the scattered wave becomes smaller than  $\omega_p$ .

In order to quantitatively evaluate the effects of a ripple driven by SBS on SRS-B, let us consider the specific example of a  $0.35 \mu\text{m}$  laser produced plasma at a temperature of 1 keV. Fig. 6.3 shows the values of  $h^2$  ( see Eqn. (3.15)) as a

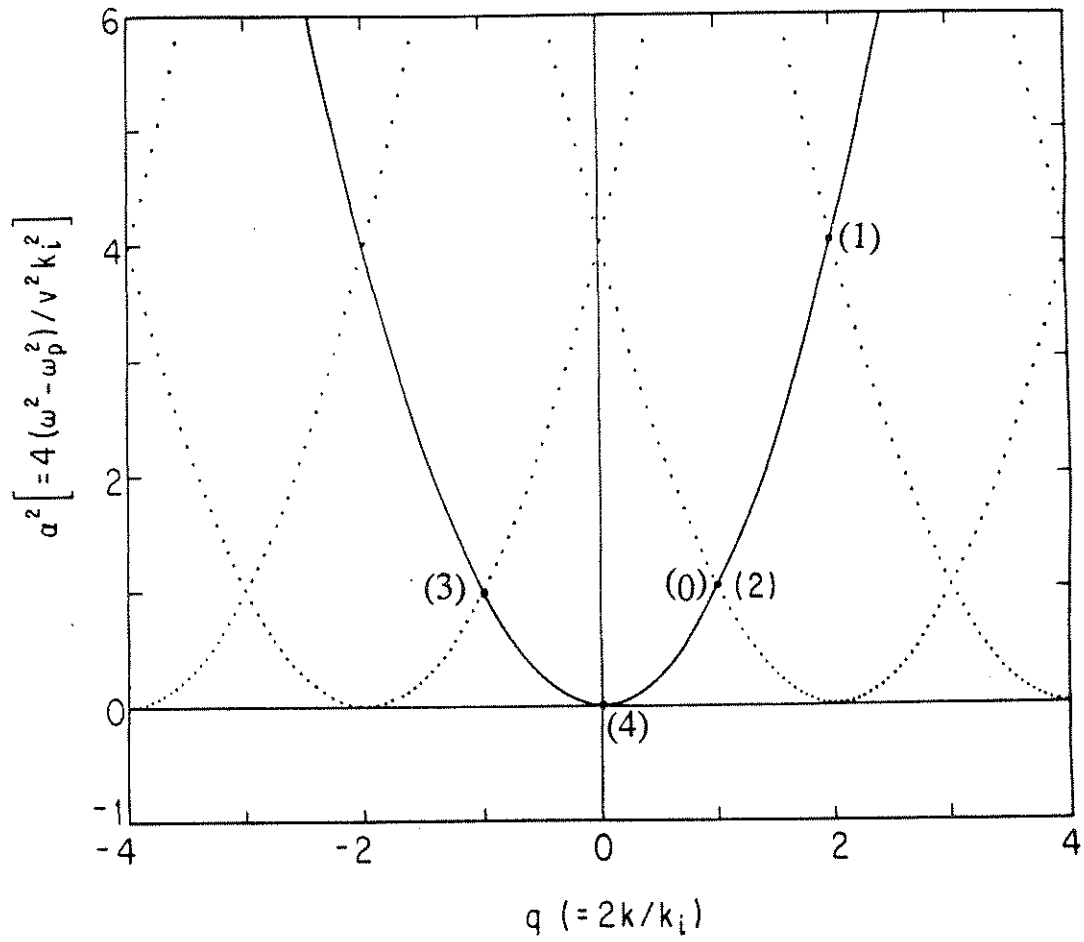


FIG. 6.2. Dispersion relation of either a plasma wave or an e.m. wave as in Fig. 5.9.



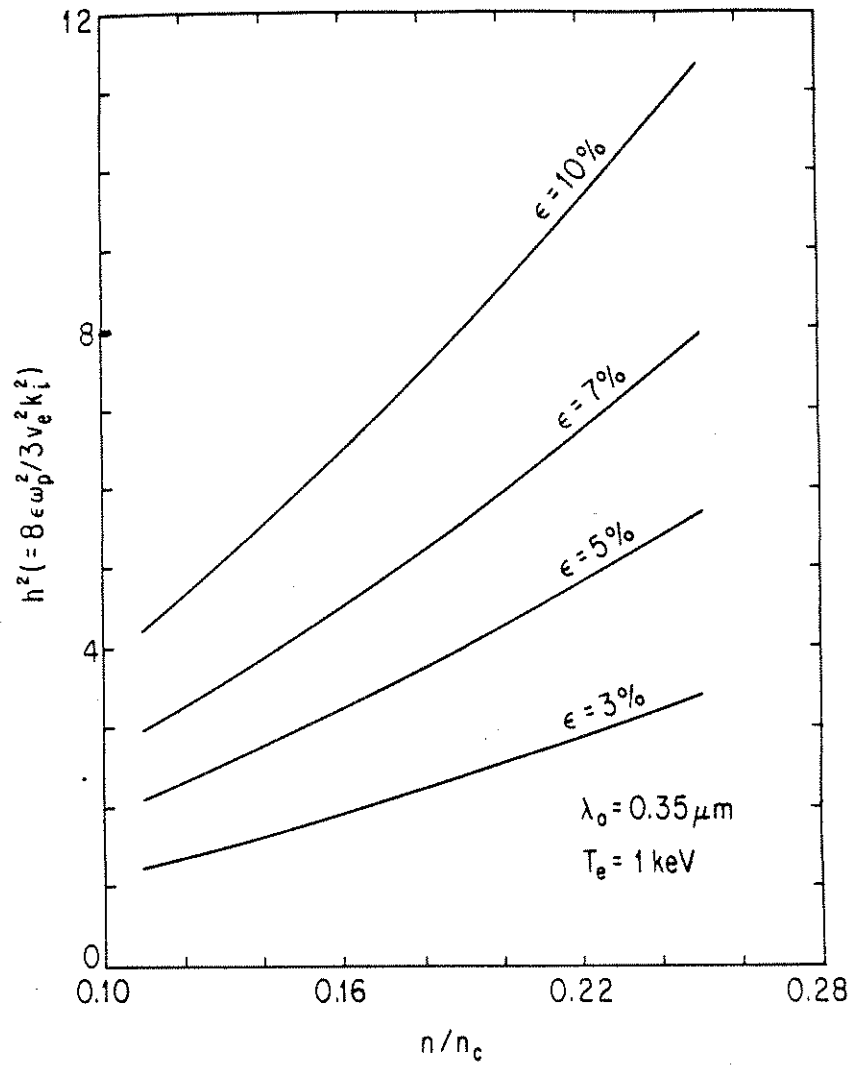


FIG. 6.3. Values of  $h^2$  vs. average density for several typical ripple amplitudes due to SBS. The plasma temperature was 1keV, and a 0.35  $\mu\text{m}$  incident laser was assumed.

function of the plasma density for typical values of the SBS driven ion wave amplitudes. We see that  $h^2$  goes from 0 to 11, whereas  $H^2$  for the e.m. wave will go from 0 to  $6 \times 10^{-2}$  according to relation (3.16). If we look at Fig. 3.7 we see that the plasma wave could be heavily damped, whereas the damping felt by the e.m. wave would be very weak. We can also estimate the relative width of the first forbidden band for the plasma wave near  $n_c/4$  and for the scattered wave at very low densities. For the plasma waves we see from Fig. 3.5 that  $\alpha_+^2 - \alpha_-^2 \approx 3$  for  $h^2 \approx 7$ . This means from Eqn. (3.19) that

$$\frac{\omega_+^2 - \omega_-^2}{(\omega_0/2)^2} \approx 27 \frac{v_e^2}{c^2} \approx 5 \times 10^{-2}, \quad (6.18)$$

here, we have divided by  $\omega_0/2$  since the frequency of the electron plasma waves excited by SRS at  $n_c/4$  is near  $\omega_0/2$ . For the scattered e.m. wave at very low densities we have from Eqn. (3.27) that

$$\alpha_+^2 - \alpha_-^2 = \frac{H^2}{2} \quad (6.19)$$

this means that from relation (3.19):

$$\frac{\omega_+^2 - \omega_-^2}{\omega_0^2} \approx \frac{H^2}{2} = \frac{\epsilon \omega_p^2}{c^2 k_0^2} \quad (6.20)$$

Thus for a very low plasma density, the width of the first forbidden band for the scattered wave given by relation (6.20) could be much smaller than the corresponding bandwidth for the electron plasma waves as given by relation

(6.18). In Eqn. (6.20) we have made use of the fact that at very low densities the values of both  $\omega$  and  $k$  of the pump are very close to the ones corresponding to vacuum.

To end the quantitative evaluation of the effects of a density ripple on both the plasma wave and the scattered e.m. wave excited by SRS-B let us look at the frequency shift of the scattered wave near  $n_c/4$ . In this region its wave vector is zero and its frequency is approximately  $\omega_0/2$ . Therefore, using Eqn. (3.28) one gets

$$\frac{\omega^2 - \omega_p^2}{(\omega_0/2)^2} \approx -\frac{3}{32}H^4$$

which is very small and could be neglected. Thus, we conclude that when considering the excitation of SRS in the presence of SBS, we can neglect, under the present conditions, the effects of the ripple on e.m waves and consider only the effects on the plasma waves.

In order to have a better understanding of the effects of a rippled density due to SBS on SRS-B, we show in Fig. 6.4 the parallelogram construction of the  $\omega$ - and  $k$ - matching conditions for SRS-B. Here,  $\omega_0$ ,  $\omega_s$ , and  $\omega_{epw}$  represent the incident e.m. wave, the scattered wave, and the plasma wave, respectively. The curve on the right represents the locus of points for which  $\omega = \omega_0 - \omega_s$  and  $k = k_0 - k_s$ . This curve is obtained by keeping  $\omega_0$  and  $k_0$  fixed and varying  $\omega_s$  and  $k_s$  on the parabola that represents the dispersion relation of the e.m. waves. The  $\omega$ - and  $k$ - matching conditions will be satisfied at the points where this locus intercepts the electron plasma wave dispersion relation. In the absence of a

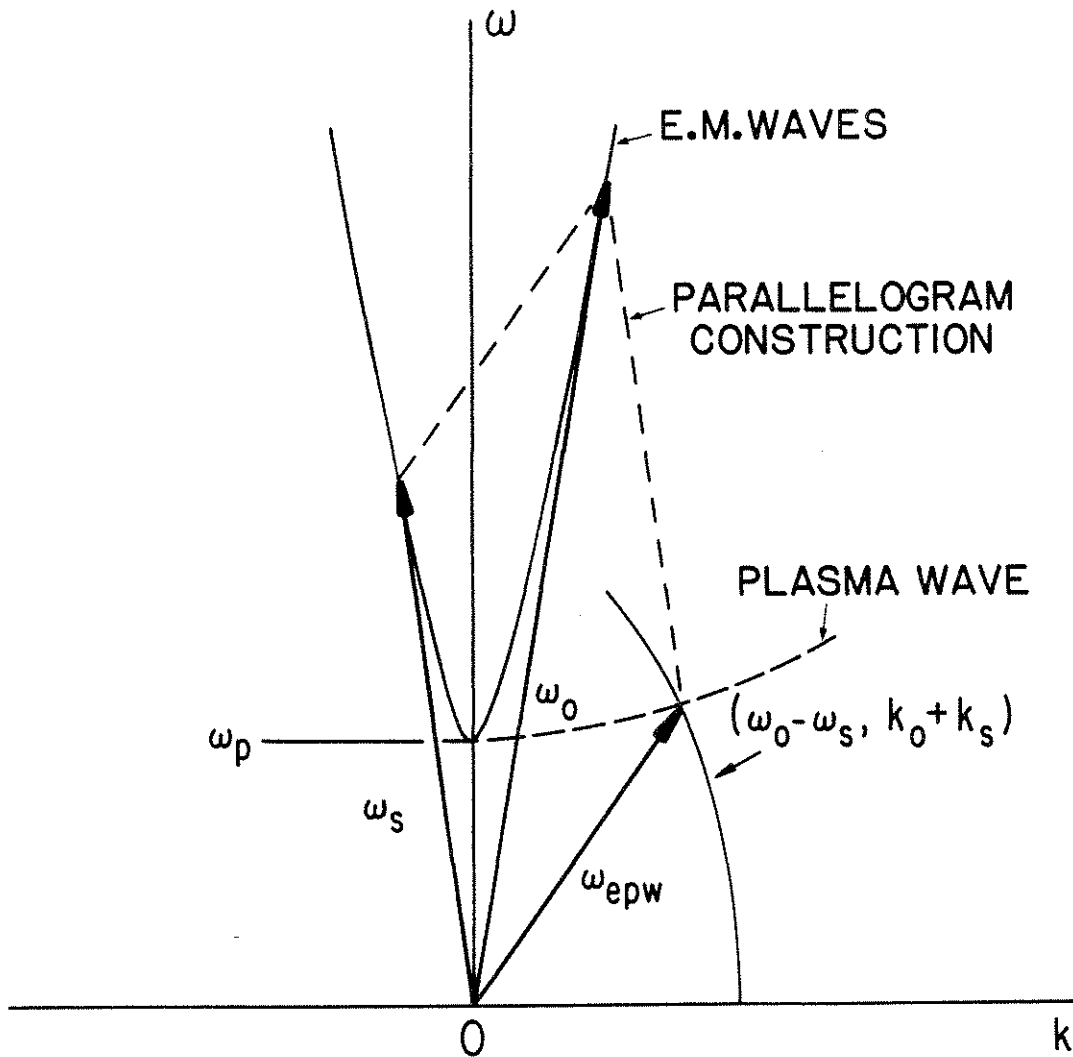


FIG. 6.4. Parallelogram construction of the  $\omega$ - and  $k$ - matching conditions for backward Raman.

ripple there is usually only one solution; however, when a ripple is present, the primary electron plasma mode (which is the strongest mode) will give rise to two solutions when  $k_s = 0$ . Figure 6.5 is a schematic of the dispersion relation of the primary electron plasma mode showing the frequency step at  $k_p = k_o$  ( or  $k_s = 0$ ). The dashed curve represents the plasma wave dispersion relation in a warm plasma in the absence of a ripple. The plasma density increases in the vertical direction. We have also represented the loci of points of frequency and wavevector  $\omega_o - \omega_s$  and  $k_o + k_s$ , respectively at each density. The  $\omega$ - and  $k$ -matching conditions  $\omega_o = \omega_s + \omega_{epw}$  and  $k_p = k_o + k_s$  will be satisfied at the points where the curves cross each other. The solutions are represented by the points (a) and (b). The presence of a ripple will introduce a negative shift  $\Delta k$  in the wave vector and a positive shift  $\Delta\omega$  in the frequency of the excited plasma wave. As a consequence, the scattered spectrum will come out red shifted. In regions near  $n_c/4$  where  $k_s = 0$ , there will be a continuous range of solutions for the frequency matching, but only the solution at each end of the frequency step will be undamped (see Figs. 6.5b and 6.5d). These two solutions will introduce two different frequency shifts away from  $\omega_o/2$  in the scattered spectrum. These two shifts can be estimated as follows. For a given ripple amplitude  $\epsilon$  and a given plasma temperature, the parameter  $h^2$  can be found from Eq. (3.15) and then the values of  $\alpha_{\pm}^2$  for  $k = k_o$  can be calculated numerically as in Figs. (3.2), (3.3), and (3.4). Once  $\alpha^2$  is known, we proceed in the following manner. From the definition of  $\alpha^2$  (see relation (3.19)) we have:

$$\omega_{epw}^2 = \omega_p^2 + 3\alpha^2 v_e^2 k_o^2 ,$$

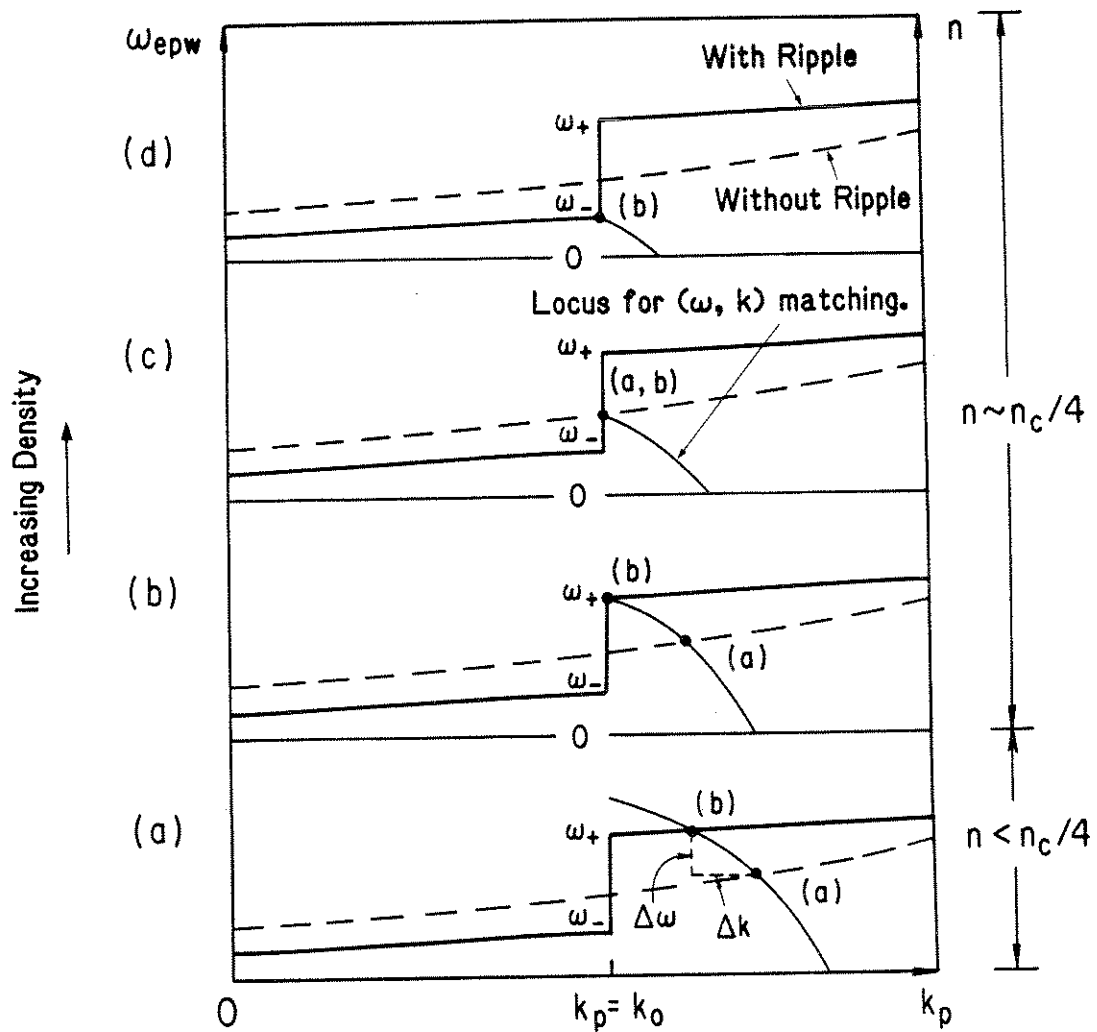


FIG. 6.5.  $\omega$  vs.  $k$  diagram of the electron plasma wave in the presence of a ripple for four different plasma densities.

where we have set  $k_i = 2k_o$ . Substituting into the frequency matching condition we get

$$\begin{aligned}\omega_o &= \omega_s + (\omega_p^2 + 3\alpha^2 v_e^2 k_o^2)^{1/2} \\ &= \omega_p + (\omega_p^2 + 3\alpha^2 v_e^2 k_o^2)^{1/2}\end{aligned}\quad (6.21)$$

since  $k_s = 0$ . If we set  $\omega_p = \omega_o/2 - \Delta\omega$  and assume  $\Delta\omega \ll \omega_o/2$ , we get after expanding relation (6.21),

$$\Delta\omega = \frac{9}{8} \alpha^2 \frac{v_e^2}{c^2} \omega_o, \quad (6.22)$$

which is just the shift due to thermal corrections multiplied by  $\alpha^2$ . Relation (6.22) can also be written as

$$\Delta\omega = \frac{9}{8} \frac{T(\text{keV})}{511} \alpha^2 \omega_o \quad (6.23)$$

Now, since  $\alpha_+^2$  is larger than 1, the shift produced by this solution will be positive, meaning that the scattered spectrum will be shifted towards the red by an amount given by Eq. (6.23). The shift produced by  $\alpha_-^2$  is more elaborate since  $\alpha_-^2$  can be positive or negative (see Fig. 3.5). The maximum value that  $\alpha_-^2$  can take is 1, corresponding to the absence of a ripple, and simply representing the red shift due to thermal corrections. As the ripple increases, the value for  $\alpha_-^2$  will move away from 1, reaching the value zero at  $h^2 \approx 3.5$ . At this point the red shift due to  $\alpha_-^2$  becomes zero. For larger ripple amplitudes,  $\alpha_-^2$  becomes

negative creating a blue shifted spectrum.

For the development of this model we have assumed an infinite, homogeneous, 1-D plasma and a stationary ripple whose amplitude remains constant in time. In real life, the plasma is neither infinite nor one-dimensional, and the ripple amplitude is most probably a function of time. We have chosen, however, such a simplified model in order to highlight the physics behind it, which otherwise would be obscured by the complicated mathematics. An improvement to this model would allow for density gradient effects, a spectrum of ion waves in 1D (rather than only SBS induced ion wave) and finally ion waves in 2D.

#### 6.4 EXPERIMENTAL DATA

Now we discuss the half harmonic results obtained in our experiments with foil targets. The threshold for the onset of the half-harmonic emission was found to be lower ( $\approx 2.5 \times 10^{14}$  W/cm<sup>2</sup>) than that for the Raman emission from below  $n_c/4$ . The most striking feature of the half harmonic spectrum was its nearly symmetric splitting about the half-harmonic position. The red and blue satellites were typically separated by 200 Å, each satellite had a bandwidth of about 280 Å. Furthermore, as shown in Fig. 6.6, the separation of the peaks was found to be strongly dependent on the laser intensity. For instance, at a laser intensity of  $2.5 \times 10^{14}$  W/cm<sup>2</sup> the peaks were first observed from a 7500 Å thick Al foil separated by 79 Å, whereas at an intensity of  $10^{15}$  W/cm<sup>2</sup> the splitting was  $200 \pm 30$  Å.

As discussed above, there are several mechanisms which may lead to the splitting of the half-harmonic spectrum. Raman in the presence of a perpendicular magnetic field seems unlikely since, according to Eqn. (6.8), it would



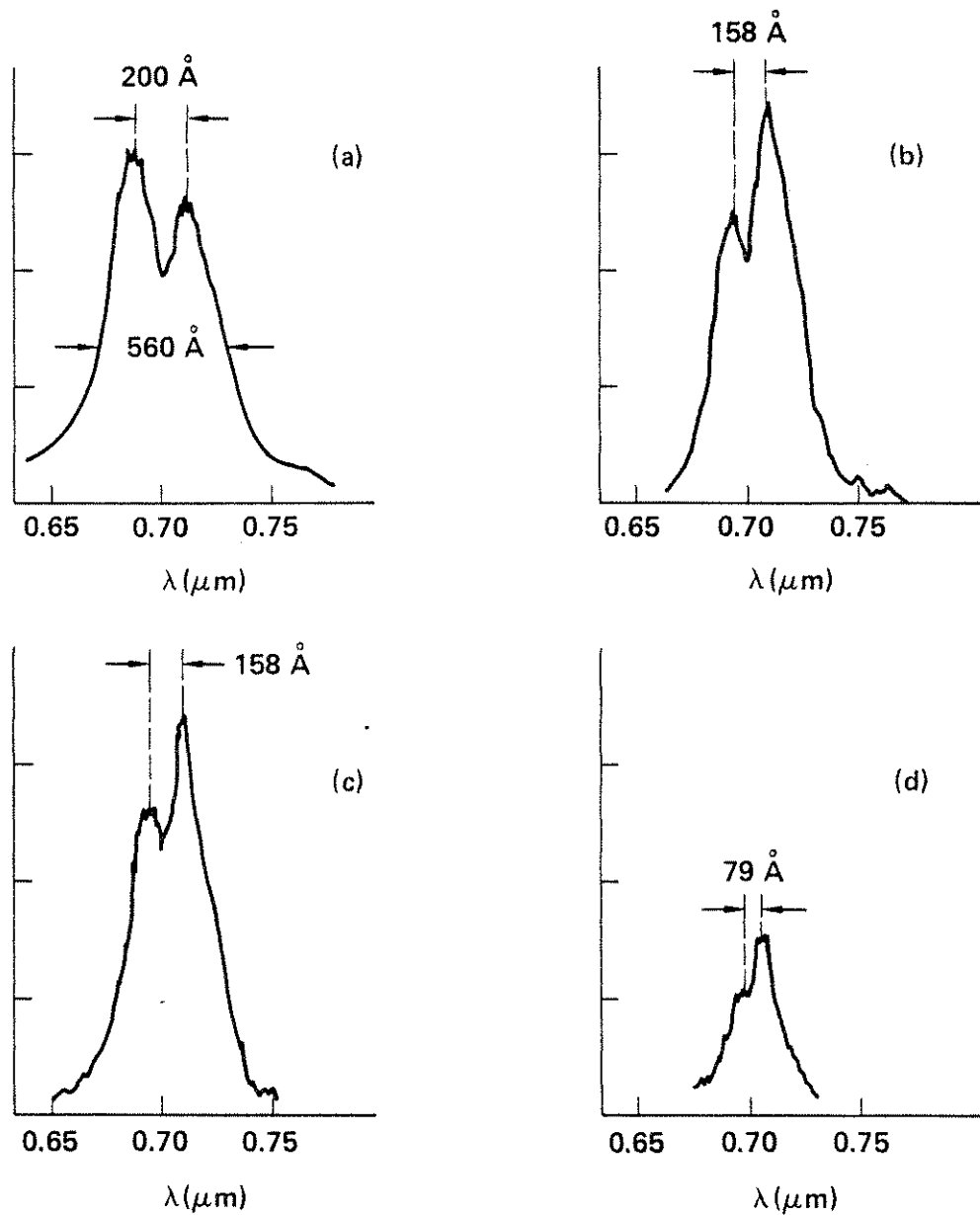


FIG. 6.6. Behavior of the backscattered spectrum around  $\omega_0/2$  with respect to the laser intensity for a 0.75  $\mu\text{m}$  thick Al foil plasma. (a)  $I = 1.2 \times 10^{15} \text{ W/cm}^2$ . (b)  $I = 9.5 \times 10^{14} \text{ W/cm}^2$ . (c)  $I = 6.1 \times 10^{14} \text{ W/cm}^2$ . (d)  $I = 2.5 \times 10^{14} \text{ W/cm}^2$ .

require a 10 MG magnetic field to produce a  $115 \text{ \AA}^\circ$  blue shift. In our experimental configuration such a large field can only be produced if the electron plasma waves associated with Raman or  $2\omega_p$  decay grow to very large amplitudes to trap a significant number of electrons. Such megagauss self-consistent B fields have been observed in two dimensional particle simulations of the SRS-F instability when the long wavelength, high phase velocity plasma waves approach wavebreaking amplitudes<sup>111</sup>. In simulations such large B fields tend to isotropize the hot electrons via the Weibel instability<sup>112,113</sup>. In the present experiments, no evidence of SRS-F from densities below  $n_c/4$  was seen when the transmitted light was spectrally analyzed. Furthermore, measurements of the high-energy electrons showed that their angular distribution was highly anisotropic. Thus, we do not think that the half-harmonic splitting is caused by the self generated magnetic fields.

Mode conversion of the plasma waves driven by the  $2\omega_p$  instability is another possibility, as was shown above. If we assume that the plasma expansion is isothermal during the time the half-harmonic is emitted, then for a plasma temperature of 750 eV, a peak separation of  $\pm 100 \text{ \AA}^\circ$  from the unshifted position would correspond to plasmons with wavenumber about  $2.8 k_0$ . Furthermore, Landau damping limit predicts a maximum broadening of about  $\pm 280 \text{ \AA}^\circ$ . The peak separation is seen to decrease with the laser intensity in qualitative agreement with the plasma temperature decreasing with lower laser intensity. However, the blue shifted peak appeared to be more sensitive to the laser intensity than the red shifted peak, disappearing for low enough intensities. This observation cannot be explained by this mechanism.

SRS-B generated from the interaction between the laser beam and the two plasmons from the  $2\omega_p$  instability can be discarded as a possible mechanism responsible for the splitting of the spectrum at  $\omega_0/2$  because of the following reasons. First, interaction of the laser beam with the plasmon going down the density gradient ( $\omega_2, \mathbf{k}_2$ ) will give rise to a scattered e.m. wave with frequency higher than  $\omega_0$ . Thus, it will have to undergo several processes in order to frequency downshift to the SRS-B interval  $\omega_0/2 \leq \omega < \omega_0$ . Second, although it is possible to generate SRS from the interaction of the laser beam and the plasmon going up the density gradient ( $\omega_1, \mathbf{k}_1$ ), this will only happen for plasma temperatures much higher than 10 keV. The resulting e.m. wave will have the same direction as  $\mathbf{k}_2$  ( $45^\circ < \theta < 90^\circ$ ). Only strong refraction effects would make turn to the backward direction. Both of these possibilities can be ruled out in our experiments.

Raman-like scattering between the SBS backscattered light and the  $\mathbf{k}_2$  plasmon was proposed by Turner et al.<sup>103</sup> as an explanation for the existence of the blue shifted satellite. However, because of the geometry of our experiment, the process would account for a maximum blue shift of about  $20 \text{ \AA}^\circ$ , which is much smaller than the observed shift. Thus, we do not think that forward scattered SBS from the  $\mathbf{k}_2$  plasmon can be the sole responsible for the presence of the blue shifted satellite.

The last mechanism proposed here is the splitting of the half-harmonic light due to the the excitation of SRS-B in the presence of ion fluctuations from SBS. As was explained above, the dispersion relation of the plasma wave in the presence of SBS is double-valued at  $n_c/4$ . Each of these branches can interact with the incident laser and scatter light with a frequency slightly red- and blue-

shifted from  $\omega_0/2$ . These shifts are given by relation (6.22). In Fig. 6.7 we have plotted the expected blue and red shifts for a 0.35  $\mu\text{m}$  laser and a plasma temperature of 1 keV. The shifts are represented in terms of  $\lambda_s$  vs. the ripple height  $\epsilon$ . We see that there is a good qualitative agreement between the experimental data (see Fig 6.6) and the expected shift from SBS. Namely, for low intensities only a red shifted peak is observed (presumably the ripple height is not significant), but as the laser intensity increases, a split structure is observed with the blue satellite being more sensitive to the laser intensity than the red satellite. To quantitatively compare the observed shifts with those predicted by this model, requires the knowledge of both the local temperature and the ripple height.

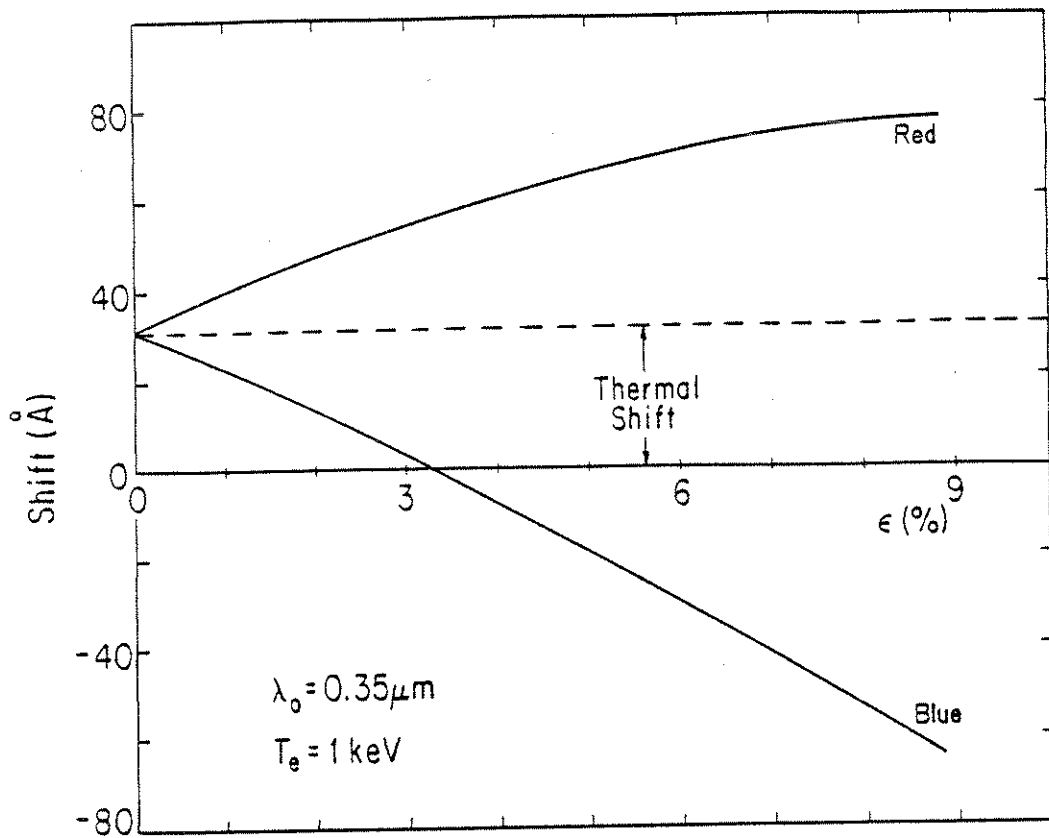


FIG. 6.7. Splitting of the scattered spectrum about  $\omega_0/2$  as a function of the ripple amplitude  $\epsilon$  driven by SBS.

## CHAPTER VII

### SUMMARY

In this thesis we have presented studies of SRS back and forward scatter from long scalelength plasmas excited when an intense  $0.35 \mu\text{m}$  laser is focused on a limited mass solid target. We attempted to create plasmas whose scalelengths would resemble those created by the future laser-fusion pellets, and tried to isolate the different processes occurring at different densities in the coronal region. we used two types of targets: a) Thin foil targets of various thicknesses, and b) Low density foam discs of fixed thickness and variable average density.

The plasmas from the foil targets were created by exploding the foils with a low energy prepulse. The instabilities were excited with an intense main  $0.35 \mu\text{m}$  pulse, nanoseconds later. By using different foil thicknesses, this technique allowed us to vary the peak plasma density. High energy electrons were observed from plasmas with peak densities below the critical density, indicating that resonance absorption was not the principal mechanism responsible for the hot electron tail. The angular distribution and polarization dependence suggested  $2\omega_p$  decay as the generation mechanism rather than SRS.

The backscattered light from the carbon foils showed a sub-half-harmonic broadband spectrum from sub-quarter critical densities. It was limited to wavelengths  $\geq 400 \text{ nm}$ . This short wavelength cut-off was attributed to strong Landau damping of the plasma waves below such low densities. The long

wavelength cut-off increased as the foil thickness increased. This cut-off was shown to be dominated by plasma hydrodynamics and the laser beam temporal profile.

The half-harmonic spectrum was observed for those targets for which simulations showed the presence of the quarter critical layer at the peak of the prepulse. This spectrum had a split structure comprising a blue and a red shifted peak, whose separation was a function of the laser intensity. The amount of light backscattered was on the order of  $10^{-4}$  %. Although the scattering process showed apparently a threshold lower than the theoretically predicted for a linear profile (presumably the dominant threshold), polarization measurements, frequency matching, and levels of scattered light, indicated that SRS was being observed.

The plasma lengths achieved by exploding foils with a prepulse, were not very much different from the ones obtained from solid slab targets because the laser focal spot dominated the plasma hydrodynamics. In order to obtain much longer length plasmas, foam targets with average densities less than the solid density were developed.

The scattered light from the foam targets showed the same general features as the light from the foil targets, except now the levels of the backscattered light increased to 0.3% of the incident energy. Up to 80% of the scattered light appeared in a narrow band of frequencies between 470-500 nm. This increase in the levels of the scattered light was directly due to the long plasma lengths achieved with the foam targets, estimated to be  $> 600 \mu\text{m}$ . The spectrum near the half-harmonic region (or near the quarter critical layer) was about  $10^4$  times weaker than the levels near 500 nm (or  $0.1n_c$ ) where SRS was the strongest.

When foam targets with average density less than  $0.25n_c$  were used, the scattered light levels near half-harmonic increased by only a factor of 10-20. This indicated that the main process responsible for quenching SRS-B near  $n_c/4$  appeared to be independent of the presence of the  $n_c/4$  layer. This result contradicts the popular notion that the low levels of scattered light near the quarter critical region (the so called Raman gap) is due to the steepening of the density profile near  $n_c/4$  due to the presence of the  $2\omega_p$  decay.

We examined several competing mechanisms occurring at  $n_c/4$  in a ripple-free plasma that could give rise to the splitting of the  $\omega_o/2$  light. Out the four mechanisms examined,  $2\omega_p$  decay appeared to be the most likely process responsible for the observed splitting. This explanation, however, was not completely satisfactory, since one had to assume ad hoc that the plasmons from  $2\omega_p$  decay were being mode converted into e.m. waves through the process inverse of resonance absorption. After invoking mode conversion,  $2\omega_p$  decay could account for the presence of two peaks, for the width of both peaks, and for the lower threshold presented by the  $\omega_o/2$  radiation compared with the sub  $n_c/4$  spectrum. This model, however, failed to predict the observed asymmetric splitting of the peaks; the blue shifted peak was found to be more sensitive to the laser intensity than the red shifted peak.

Since SBS was operative in all our experiments on both foil and foam targets when SRS was observed, we examined theoretically the propagation of both the e.m. waves and the plasma waves in the presence of an ion density ripple. We found that a ripple introduces forbidden frequency bands due to constructive interference at  $k = nk_i/2$ . The e.m. waves were found to be far less sensitive to the density ripples than the plasma waves. We also showed that a SBS-induced



ripple can directly influence the frequency matching condition for Raman at  $n_c/4$  and thereby lead to an asymmetric splitting of the half-harmonic radiation. The blue shifted peak was found to be more sensitive to the ripple amplitude in reasonable agreement with the experimental data. This theory is an attempt at understanding the normal high frequency modes of a plasma in a rippled density. A full treatment of the effect of the SBS instability on SRS, particularly on SRS threshold, reflectivity levels, and peak widths, still needs to be calculated.

We also observed scattering in the forward direction from the foam targets. This scattering was about  $10^4$  times weaker than the one in the backward direction and disappeared with a 20% reduction of the laser intensity. Since the SRS-F has such a high threshold, and since the scattered frequency range is similar to backscatter, it is suggested that the forward emission is being seeded by SRS-B. The most likely way in which this excitation could occur was through the coupling of the SRS-B plasma wave with the SBS ion acoustic wave.

## APPENDIX

### GLASS DEVELOPMENT LASER SYSTEM

In this appendix we describe the laser system used in our experiments.

The experimental work described in this dissertation was carried out at the National Laboratory for Users Facility at the University of Rochester using the Glass Development Laser (GDL) system.

GDL is a Nd: Phosphate glass laser with six amplification stages, the last one having a rod with a aperture of 90 mm. The system is capable of generating 150 J in 1 ns. The output beam at  $1.054 \mu\text{m}$  ( $1 \omega$ ) is triple converted to  $0.35 \mu\text{m}$  ( $3 \omega$ ) by means of two KDP type II crystals with an efficiency of 30%. The beam at the output of the second KDP crystal is a mixture of the fundamental, the second, and the third harmonic in a proportion of 10 - 1 - 40 respectively. These three different frequencies are separated by means of selective reflecting mirrors as shown in Fig. A.1. The mirrors M1, M2, and M3 drive 95% of the  $3\omega$  beam, together with 5% of the  $2\omega$  and  $1\omega$  beams to the target. The main part of the  $1\omega$  beam is directed by the mirrors M4 and M5. The remnants of the three frequencies that are transmitted through the M4 mirror are used as laser diagnostics. In the figure, only three calorimeters are shown.

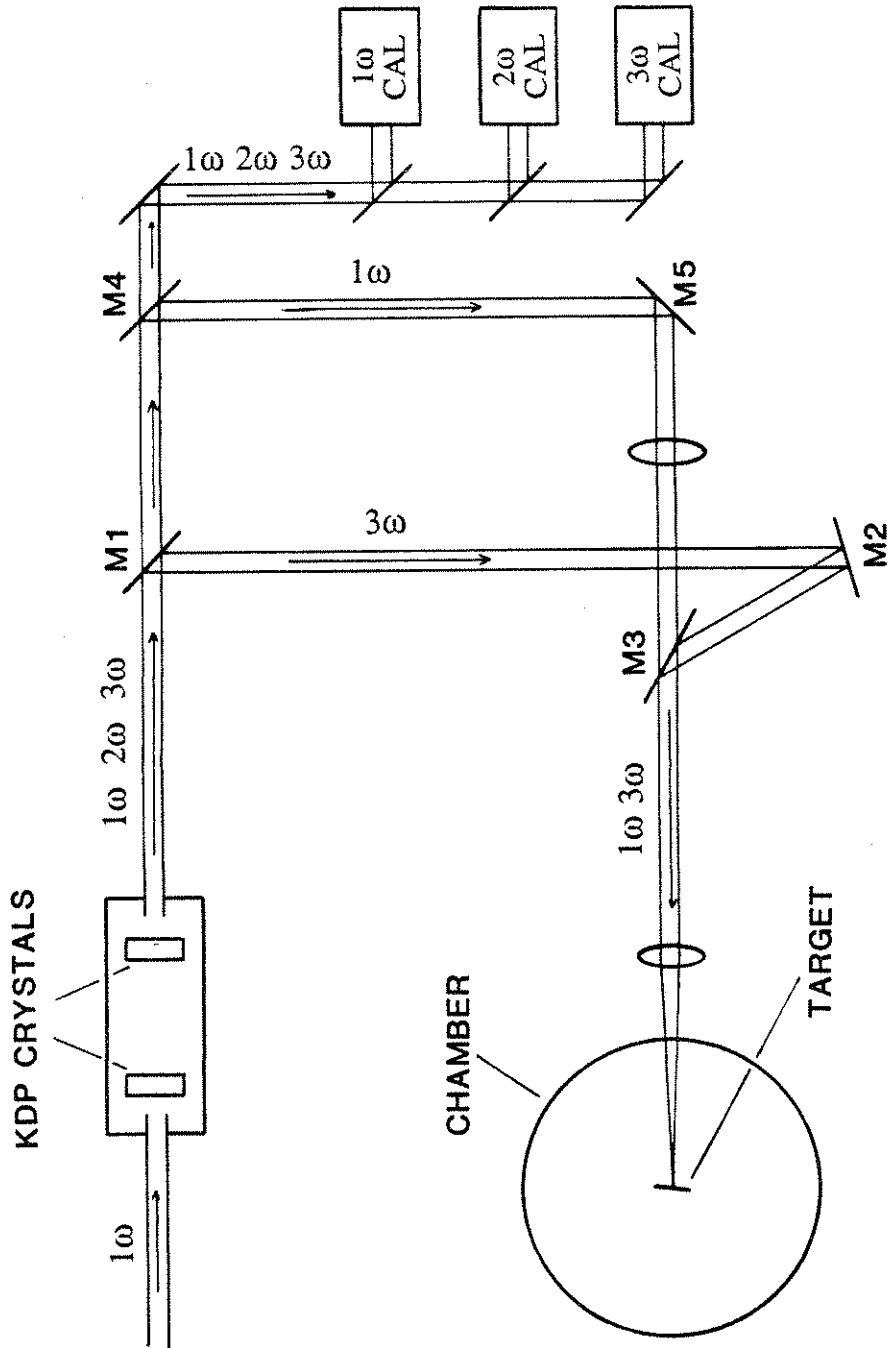


FIG. A.1. Layout of the Glass Development Laser (GDL) system.

## REFERENCES

1. E.A. Jackson, Phys. Rev. 153, 235 (1967).
2. J.L. Bobin, M Decroisette, B. Meyer, and Y. Vitel, Phys. Rev. Lett. 30, 594 (1973).
3. J.F. Drake and Y.C. Lee, Phys Rev. Lett. 31, 1197 (1973).
4. J.F. Drake, P.K. Kaw, Y.C. Lee, G. Schmidt, C.S. Liu, and M.N. Rosenbluth, Phys, Fluids 17, 778 (1974).
5. Paul Koch and James Albritton, Phys. Rev. Lett. 34, 1616 (1974).
6. C.S. Liu, M.N. Rosenbluth, and R.B. White, Phys. Fluids 17, 1211 (1974)
7. D.W. Forslund, J.M. Kindel, and E.L. Lindman, Phys. Fluids 18, 1002 (1975).
8. L.M. Gorbunov, V.I. Domrin, and R.R. Ramazashvili, Sov. Phys. JETP 43, 1128 (1976).
9. J.J Thomson, Phys. Fluids 21, 2082 (1978).
10. R.G. Watt, R.D. Brooks, and Z.A. Pietrzyk, Phys. Rev. Lett 41, 170 (1978).  
B. Amini and F.F. Chen, to appear in Phys. Fluids.
11. J.J. Schuss, T.K. Chu, and L.C. Johnson, Phys. Rev. Lett. 40, 27 (1978)
12. H.A. Bakdis, C.J. Samson, and P.B. Corkum, Phys. Rev. Lett. 41, 1719 (1978).
13. A.B. Langdon, B.F. Lasinski, and W.L. Kruer, Phys. Rev. Lett. 43, 133 (1979).

14. W.L. Kruer, K. Estabrook B.F. Lasinski, and A.B. Langdon, *Phys. Fluids* 23, 1326 (1980).
15. K. Estabrook, W. Kruer, and B.F. Lasinski, *Phys. Rev. Lett.* 45, 1399 (1980).
16. H.A. Baldis and C. Walsh, *Phys. Rev. Lett* 47, 1658 (1981).
17. H.A. Baldis and C. Walsh, *Phys. Fluids* 26, 1364 (1981).
18. H. Azechi, N.A. Ebrahim, K. Estabrook, C. Clayton, H. Figueroa, and C. Joshi, *Bull. Am. Phys. Soc.* 27 909 (1982).
19. D. W. Phillion, D.L. Banner, E.M. Campbell, R.E. Turner, and K.G. Estabrook, *Phys. Fluids* 25, 1434 (1982).
20. A.A. Offenberger, R. Fedosejevs, W. Tighe, and W. Rozmus, *Phys. Rev. Lett.* 49, 371 (1982).
21. V.K. Tripathi and K. Papadopoulos, *Comments Plasma Phys. Controlled Fusion* 7, 123 (1982).
22. K. Tanaka, L.M. Goldman, W. Seka, M.C. Richardson, J.M. Soures, and E.A. Williams, *Phys. Rev. Lett.* 48, 1179 (1982).
23. H. Azechi, N.A. Ebrahim, H. Figueroa, and C. Joshi, *Bull. Am. Phys. Soc.* 28, 1248 (1983).
24. K. Estabrook and W.L. Kruer, *Phys. Fluids* 26, 1892 (1983).
25. R.E. Turner, D.W. Phillion, E.M. Campbell, and K.G. Estabrook, *Phys. Fluids* 26, 579 (1983).
26. H. Figueroa, C. Joshi, and C.E. Clayton, *Bull. Am. Phys. Soc.* 29, 1260 (1984).

27. C. Joshi, H. Figueroa, and C.E. Clayton, *Bull. Am. Phys. Soc.* 29, 1260 (1984).
28. H. Figueroa, C. Joshi, H. Azechi, N.A. Ebrahim, and K. Estabrook, *Phys. Fluids* 27, 1887 (1984).
29. H. Figueroa, C. Joshi, C.E. Clayton, H. Azechi, N.A. Ebrahim and K. Estabrook, *Laser Interaction and Related Plasma Phenomena*, edited by H. Hora and G. Miley, p. 527, Plenum Press, N.Y. (1984)
30. C.J. McKinstrie, A. Simon, and E.A. Williams, *Phys. Fluids*, 27 2738 (1984).
31. Kent Estabrook and W.L. Kruer, *Phys. Rev. Lett.* 53, 465 (1984).
32. C.J. Walsh, D.M. Villeneuve, and H.A. Baldis, *Phys. Rev. Lett.* 53, 1445 (1984)
33. R.P. Drake, R.E. Turner, B.F. Lasinski, K.G. Estabrook, E.M. Campbell, C.L. Wang, D.W. Phillion, E.A. Williams, and W.L. Kruer, *Phys. Rev. Lett.* 53, 1739 (1984).
34. W. Seka, E.A. Williams, R.S. Craxton, L.M. Goldman, R.W. Short, and K.Tanaka, *Phys. Fluids* 27, 2181 (1984).
35. H.C. Barr, T.J. Boyd, L.R. Gardner, and R. Rankin, *Phys. Fluids* 27, 2730 (1984).
36. H. C. Barr, T.J. Boyd, G.A. Gardner, and R. Rankin, *Phys. Rev. Lett.* 53, 462 (1984).
37. Kent Estabrook and W.L. Kruer, *Phys. Fluids* 26, 1892 (1984).
38. Francis F. Chen, UCLA PPG-791 (1984).

39. Francis F. Chen, UCLA PPG-817 (1984).
40. Albert Simon and Robert W. Short, *Phys. Rev. Lett.* 53, 1912 (1984)
41. R.E. Turner, Kent Estabrook, R.L. Kauffman, D.R. Bach, R.P. Drake, D.W. Phillion, B.F. Lasinski, E.M. Campbell, W.L. Kruer, and E.A. Williams, *Phys. Rev. Lett.* 54, 189 (1985).
42. R.E. Turner, Kent Estabrook, R.L. Kauffman, D.R. Bach, R.P. Drake, D.W. Phillion, B.F. Lasinski, E.M. Campbell, W.L. Kruer, and E.A. Williams, *Phys. Rev. Lett.* 54, 189 (1985).
43. D.M. Villeneuve, C.J. Walsh, and H.A. Baldis, *Phys. Fluids* 28, 1591 (1985).
44. C.J. McKinstrie and A. Simon, *Phys. Fluids* 28, 2602 (1985).
45. B.B. Afeyan and E.A. Williams, *Phys. Fluids* 28, 3397 (1985).
46. R. Rankin and T.J.M. Boyd, *Phys. Fluids* 28, 3380 (1985)
47. C.R. Menyuk, N.M. El-Siragy, and W.M. Manheimer, *Phys. Fluids* 28, 3409 (1985).
48. D. Russel, M. Goldman, and D.L. Newman, *Phys. Fluids* 28, 2162 (1985).
49. T.J.M. Boyd, G.A. Gardner, and R. Rankin, *Phys. Fluids* 28, 1193 (1985).
50. Francis F. Chen, UCLA PPG-893 (1985)
51. A. Simon, W. Seka, L.M. Goldman, and R.W. Short, *Phys. Fluids* 29, 1704 (1986).
52. H.C. Barr, T.J.M. Boyd, and G.A. Coutts, *Phys. Rev. Lett.* 56, 2256 (1986).

53. A.P.G. Kutty, and B.K. Sinha, *Phys. Fluids* 29 1298 (1986).
54. C.L. Shepard, J.A. Tarvin, R.L. Berger, Gar. E. Bush, R.R. Johnson, and R.J. Schroeder, *Phys. Fluids* 29, 583 (1986).
55. J.A. Heikkinen and S.J. Kartunen, *Phys. Fluids* 29 1291 (1986).
56. H. Figueroa and C. Joshi, *Laser Interaction and Related Plasma Phenomena*, edited by H. Hora and G. Miley, Plenum Press, N.Y. (1986) to be published.
57. H. Figueroa, C. Joshi, and C.E. Clayton, to be published in *The Phys. Fluids*.
58. H. Figueroa and C. Joshi, submitted for publication to *The Phys. Fluids*.
59. W. Rozmus, J. Samson, R.P. Sharma, W. Tighe, and A.A. Offenberger, to be published.
60. N.A. Ebrahim, H.A. Baldis, C. Joshi, and R. Benesh, *Phys. Rev. Lett.* 45, 1179 (1980).
61. N.A. Ebrahim and C. Joshi, *Phys. Fluids* 24, 138 (1981).
62. N.A. Ebrahim, C. Joshi, and H.A. Baldis, *Phys. Lett. A* 84, 253 (1981).
63. C. Joshi, T. Tajima, J.M. Dawson, H.A. Baldis, and N.A. Ebrahim, *Phys. Rev. Lett.* 47, 1285 (1981).
64. H. Azechi, N.A. Ebrahim, K. Estabrook, C. Clayton, H. Figueroa, and C. Joshi, *Bull. Am. Phys. Soc.* 27, 950 (1982).
65. H. Azechi, N.A. Ebrahim, H. Figueroa, and C. Joshi, *Proceedings of the 9th International Conference on Plasma Physics and Controlled Nuclear Fusion Research*, Vol. 1, p. 115 (1982).



66. D.W. Phillion, E.M. Campbell, K.G. Estabrook, G.E. Phillips, and F. Ze, Phys. Rev. Lett. 49, 1405 (1982).
67. K.A. Nugent and B. Luther-Davis, Phys. Rev. Lett. 49, 1943 (1982).
68. R. G. Berger, R. D. Brooks, and Z.A. Pietrzyk, Phys. Fluids 26, 354 (1983).
69. D. M. Villeneuve, R.L. Keck, B.B. Afeyan, W. Seka, and E.A. Williams, Phys. Fluids 27, 721 (1984).
70. R.L. Keck, L.M. Goldman, M.C. Richardson, W. Seka, and K. Tanaka, Phys. Fluids 27, 2762 (1984).
71. J.M. Manley and H.E. Rowe, Proc. IRE 47, 2115 (1959).
72. See for example H.A. Baldis and C.J. Walsh, Phys. Fluids 26, 3426 (1983).
73. H.A. Baldis and D.M. Villeneuve, *Proceedings of the 7th International Workshop on Laser Interaction and Related Plasma Phenomena*, (1985), to be published.
74. J. Meyer and H. Houtman, Phys. Rev. Lett. 53, 1344 (1984).
75. See references 12 and 16.
76. H.A. Baldis and C.J. Walsh, Phys. Fluids 26, 1364 (1983).
77. F. Martin, H.A. Baldis, and C.J. Walsh, Phys. Rev. Lett. 52, 196 (1984) and references therein.
78. Y.S. Al-Shivaida, A.A. Offenberger, and A. Ng, Phys. Rev. A 25, 2857 (1982).
79. A.A. Offenberger and A. Ng, Phys. Rev. Lett. 45, 1189 (1980).
80. A.A. Offenberger, A. Ng, and L. Pitt, Phys. Rev. Lett. 40, 873 (1978).

81. W.M. Manheimer and D.G. Colombant, *Phys. Fluids* 21, 1818 (1978).
82. J.M. Dawson and C. Oberman, *Phys. Fluids* 5, 517 (1962).
83. J.M. Dawson and C. Oberman, *Phys. Fluids* 6, 394 (1963).
84. R.J. Faehl and W.L. Kruer, *Phys. Fluids* 20, 55 (1977).
85. P.K. Kaw, A.T. Lin, and J.M. Dawson, *Phys. Fluids* 16, 1967 (1973).
86. Dwight R. Nicholson, *Phys. Fluids* 19, 889 (1976).
87. W. Rozmus, A.A. Offenberger, and R. Fedosejevs, *Phys. Fluids* 26, 1071 (1983)
88. Charles Aldrich, B. Bezzerides, D.F. DuBois, and Harvey Rose, to be published in *Comments on Plasma Physics and Controlled Fusion*.
89. H.C. Barr and F.F. Chen, to be published.
90. C. Darrow, D. Umstadter, T. Katsouleas, W.B. Mori, C.E. Clayton, and C. Joshi, *Phys. Rev. Lett.* 24, 2629 (1986).
91. Jon Mathews and R.L. Walker, *Mathematical Methods of Physics*, ( Benjamin/Cummings publishing Co. Menlo Park, CA. 1970) p. 203.
92. J.M. Dawson, *Advances in Plasma Physics*, edited by A. Simon and W.A. Thomson (Interscience, New York, 1968), Vol. 1, p. 1.
93. J. Sheffield, *Plasma Scattering of Electromagnetic Radiation*, (Academic Press, New York, 1975), Chaps. 6 and 7.
94. T.P. Coffey, *Phys. Fluids* 14, 1402 (1971).
95. R.F. Benjamin, G.H. McCall, and A.W. Ehler, *Phys. Rev. Lett.* 42, 890 (1979).

96. See references 19, 22, 25, and 28.
97. See references 19, 22, and 25.
98. K.A. Tanaka, B. Boswell, R.S. Craxton, L.M. Goldman, F. Guglielmi, W. Seka, R.W. Short, and J.M. Soures, *Phys. Fluids* 28, 2911 (1985).
99. A. Coudeville, P. Eyharts, J.P. Perrine, L. Rey, and R. Rouillard, *J. Vac. Sci. Technol.* 18, 1227 (1981).
100. P. Koch and E.A. Williams, *Phys. Fluids* 27, 2346 (1984).
101. E. Elazar, W. Toner, and E.R. Wooding, *Plasma Physics* 23, 813 (1981).  
Also see reference 28.
102. W. Seka, B.B. Afeyan, R. Boni, L.M. Goldman, R.W. Short, and K. Tanaka, *Phys. Fluids* 28, 2570 (1985).
103. R.E. Turner, D.W. Phillion, B.F. Lasinski, and E.M. Campbell, *Phys. Fluids* 27, 511 (1984).
104. E. McGoldrich, S.M.L. Sim, R.E. Turner, and O. Willi, *Opt. Comm.* 50, 107 (1984).
105. S.S. Kartunen, *Laser and Particle Beams*, Vol. 3, part 2, 157 (1985).
106. R. Kolodner and E. Yablonovitch, *Phys. Rev. Lett.* 43, 1405 (1979).
107. J.A. Stamper, K. Papadopoulos, R.N. Sudan, S.O. Dean, E.A. McLean, and J.M. Dawson, *Phys. Rev. Lett.* 26, 1012 (1971).
108. Francis Chen, *Introduction to Plasma Physics*, (Plenum Press, New York 1977).
109. J. Meyer, J.E. Bernard, B. Hilko, H. Houtman, G. McIntosh, and R. Popil, *Phys. Fluids* 26, 3162 (1983).

110. R.L. Berger, L.V. Powers, Phys. Fluids 28, 2895 (1985).
111. T.P. Coffey, Phys. Fluids 14, 1402 (1971).
112. Warren Mori, private communication
113. A. Ramani and G. Laval, Phys. Fluids 21, 980 (1978).